Politecnico di Torino

ScuDo
Scuola di Dottorato ~ Doctoral School
WHAT YOU ARE, TAKES YOU FAR

Doctoral Dissertation
Doctoral Program in Electronic Engineering (35^{th}cycle)

Modeling and Design of 3-Terminal Perovskite/Silicon HBT Tandem Solar Cell

By

Gemma Giliberti

******

Supervisor:
Prof. Federica Cappelluti

Doctoral Examination Committee:
Dr. James Connolly, CentraleSupélec
Prof. Isodiana Crupi, Università degli Studi di Palermo
Prof. Karin Hinzer, University of Ottawa
Prof. Matthias Auf der Maur, Università degli Studi di Roma Tor Vergata

Politecnico di Torino
2023

Declaration

I hereby declare that, the contents and organization of this dissertation constitute my own original work and does not compromise in any way the rights of third parties, including those relating to the security of personal data.

Gemma Giliberti
2023

* This dissertation is presented in partial fulfillment of the requirements for **Ph.D. degree** in the Graduate School of Politecnico di Torino (ScuDo).

With love, to EM

Acknowledgements

Desidero ringraziare professionalmente e personalmente la mia Supervisor e Mentore, la professoressa Federica Cappelluti, che mi ha accompagnata e incoraggiata lungo tutto il mio percorso di dottorato, per l'impegno, la dedizione e la scrupolosità con cui ha revisionato questo lavoro di tesi; per l'approccio sempre sincero e diretto, per le conversazioni formative sempre volte al miglioramento, per avermi arricchito culturalmente. Questa tesi rappresenta il risultato di duro lavoro e di una collaborazione preziosa, costellata da momenti di gioia, ansia e difficoltà, che porterò sempre con me. Grazie.

Grazie a Matteo non solo per i suggerimenti professionali sempre puntuali, ma anche per la costante spinta a perseguire obiettivi sempre più ambiziosi. Grazie di cuore ad Eva e Alberto, amici e colleghi. Sono grata per il sostegno, la presenza, il confronto e il conforto in questi anni intensi.

Un sentito ringraziamento a tutto il CHOSE, soprattutto a Francesco, Erica e Francesca. Il tempo trascorso a Roma lascia un segno profondo in me di umanità ed entusiasmo che ho scoperto essere presupposti essenziali di vera professionalità.

Un grazie sincero va a Megragrosa, a Sara, Cristina, Eleonora e al VAIA F.C. che arricchiscono la mia vita e mi regalano momenti di condivisione e leggerezza.

Con immenso amore, stima e affetto ringrazio le persone che mi hanno sempre sostenuta e incoraggiata nella mia formazione accademica: mia madre e mio padre. Questa tesi è sopratutto frutto del vostro amore, della vostra perseveranza e dei valori che mi avete trasmesso. In egual modo, ringrazio mia zia Gina e mio zio Dino, punti imprescindibili di riferimento. Grazie per il vostro amore.

Grazie a tutta la mia famiglia, in particolare a mia sorella che mi riserva sempre parole di sostegno, infondendo in me sempre fiducia e tenerezza.

Un immenso ed inestimabile grazie alla persona che ha cambiato la mia vita, a Manu. Ogni pagina di questa tesi potrebbe raccontare il tuo sostegno costante, le notti insonni di lavoro, la tua infinita voglia e attenzione di comunicare. Grazie per incoraggiarmi a dare sempre il massimo.

Infine ringrazierei me stessa...

Abstract

The *energy transition* aims to move the global energy sector from fossil-based sources towards a zero-carbon system. Among sustainable energies, Silicon-based photovoltaic devices, providing clean energy at a low cost, are a viable alternative to traditional non-renewable sources of energy. Substantial investments in solar technology are ongoing to minimize their manufacturing costs while increasing their efficiency.

In this ever-changing scenario, Perovskite has drawn significant attention in the photovoltaics research community owing to their optimal opto-electronic properties and the fast progress achieved in the last decade. Perovskite is emerging as an ideal candidate for the development of low-cost thin-film silicon based tandems, able to overcome the efficiency bottleneck of single-gap Si cells.

To date, perovskite/silicon (PVS) tandem devices reported in the literature exploit mainly the 2-Terminal (2T) series connected structure, however 3-Terminal (3T) solutions, with interdigitated back contact (IBC) silicon bottom cell, have recently attracted great interest due to their potential for higher energy yield. Although the IBC cell is an ideal candidate for 3T tandems, according to the International Roadmap for Photovoltaics their commercialization will remain comparatively limited with respect to double-sided contact cells.

In this direction, this thesis investigates a novel 3T PVS tandem solar cell employing a well known structure used in microelectronic applications and proposed in 2015 by Martí and Luque as elementary building block for multi-junction solar cells: the hetero-junction bipolar transistor (HBT) structure. The 3T-HBT architecture properly engineered, allows the independent operation of the top and bottom sub cells, achieving maximum efficiency as high as classical 2T and 3T approaches, but with a simpler device architecture, because it also avoids the need of any tunnel junction or intermediate recombination layer.

After reviewing the theoretical limit efficiency of the 3T-HBT grounded on detailed

balance model, we introduce for the first time a compact closed-form analytical model of the 3T-HBT solar cell, by extending the well known analytical drift-diffusion Hovel model of single-junction solar cells. The generalized Hovel model provides an ideal means to analyze the basic operating principle of the 3T-HBT with a mindset already oriented to a realistic device (with realistic material properties and geometry), allowing to gain the preliminary knowledge needed to get insight from more advanced numerical models. It also naturally yields to the formulation of an equivalent circuit model of the HBT solar cell suitable for the assessment of parasitic loss.

In the second part of the dissertation, we present a thorough analysis of both planar and textured PVS 3T-HBT solar cells made on hetero-junction silicon bottom cell, based on coupled electromagnetic and transport numerical simulations. The numerical model is firstly validated against experimental data of a representative 2T series-connected tandem taken from the literature. Then, we use it to study the photovoltaic behavior of the 3T-HBT compared to the 2T one, devising possible bottlenecks and routes of optimization. The results show promising performance of the *intrinsic* device, i.e. when possible additional optical and electrical loss induced by the need of a third terminal are not considered.

However, to foster the development of this attractive concept, concrete design solutions shall deal not only with the optimization of the HBT-like multilayer stack, but also with the problem of conceiving appropriate layouts for the current collecting grid of the middle base terminal. In this direction, to address the additional optical and resistive losses associated to the current collecting grids of the HBT architecture, in the last part of the dissertation, we present a modeling framework that combines electro-optical simulations of the *intrinsic* 3T-HBT tandem stack with circuit-level simulations. The impact of the optical and electrical loss due to the current collecting grids on the scalability of the cell size is analyzed to ultimately develop a holistic optimization of the device design. In this regard, several possible approaches are considered for the development of HBT perovskite/silicon cells with heterojunction and homojunction c-Si technologies. The results show that the HBT architecture is a promising candidate for developing high efficiency 3T perovskite/silicon tandem solar cells compatible with standard silicon photovoltaics industry.

Contents

List of Figures

Acronyms

2T 2-Terminal

3T 3-Terminal

3T-HBT 3T-Heterojunction Bipolar Transistor

4T 4-Terminal

AL-BSF Aluminum Back-Surface-Field

AM Air Mass

E_{sun} Solar Irradiance

EQE External Quantum Efficiency

FE-SEM Field Effect Scanning Electron Microscope

GSMM General Scattering Matrix Method

HBT Heterojunction Bipolar Transistor

HIT Heterojunction with Intrinsic Thin layers

ITO Indium Thin Oxide

MAI CH_3NH_3I

MAPI $CH_3NH_3PbI_3$

MPP Maximum Power Point

PDD Poisson-drift-diffusion

PERC Passivated Emitter Rear Cell

PV Photovoltaic

PVK Perovskite

PVS PVK/Si

RT RayTracing

SHJ Silicon Hetero-Junction

Si Silicon

SPF Spectral Photon Flux

SQ Shockley-Queisser

TCAD Technology Computer-Aided Design

TCO Transparent Conductive Oxide

TIC Top Interdigitated Contacts

TMM Transfer Matrix Method

TOC Top Overlapped Contacts

Chapter 1

Energy transition powered by the photovoltaic technology

The 21st century is primarily focused on energy transition, power management, renewable sources, green city, cleaner cars, and fossil-free transport. The term "energy transition" or "energy sustainability" pertains to the shift of the energy sector from traditional fossil-based energy production, such as coal, oil, and natural gas, towards eco-friendly, renewable energy sources, such as wind and sunlight, coupled with efficient and durable batteries for energy storage [1]. However, many challenges need to be solved to achieve this energy transition, including economical and social sustainability, financial barriers, regulatory constraints, and technological limitations. This requires that nations adopt significant measures to foster this transformation process.

Energy outlooks, data and charts provide a clear picture of the current energy situation and several milestones have been established towards the goal of net-zero emissions, that according to the United Nations Sustanaible Development Goals should be achieved by 2050 [2]. In this regard, the energy transition goals are two: mitigate global warming through the exploitation of renewable energy sources, and ensure fair and equal socio-economic development [3]. Section 1.1 provides a brief overview of the author's personal motivations and interest in this research field, exploring gender inequalities in the energy sector.

Section 1.2 analyzes the Net Zero Emission by 2050 scenario, where solar energy source plays a leading role. In particular, photovoltaic devices offer innovative and low-cost technology solutions, becoming increasingly competitive with traditional

power sources.
This thesis focuses on the study of a novel photovoltaic device for terrestrial applications: the three terminal perovskite/silicon bipolar transistor solar cell. Aware that this work is just one piece in the large puzzle of the energy transition, we hope that it will contribute to a more sustainable future.

1.1 Personal motivation

The main challenges related to the energy renewable transition are to limit the global warming to 1.5 °C (*Net Zero by 2050* [2]) and to promote inclusive and equitable socio-economic development [3]. In the last decade, the growing awareness of environmental concerns and technological advancements have facilitated the commitment to the shift towards 100% renewable cities, presenting great potential for economic advancement, poverty reduction, and gender equality. Today, energy has a leading role in people lives, whose lifestyle can affect the climate change [4]. In this scenario, energy policy cannot be gender neutral recognizing that women and man have different energy needs depending on their demographic, social and economic status [5]. For example, there is a higher probability that older women experience energy poverty rather than men. In fact, when there is an increase in oil and gas prices there is a rise in energy costs, and hence heating/air conditioning costs are higher. This particularly can affect older people and above all women living alone in large houses, due to their lower pensions coupled with their higher life expectancy [6]. However, the lack of gender-disaggregated data and low representation of women in decision-making (only 4% of women have participated in the World Energy Council chairs (WEC) and 18% in secretaries [8]) and technical fields hamper the formulation of gender-inclusive energy policies [9].
Fig. 1.1 shows that the electricity workforce in the U.S is heavily male. In Europe, the situation is worse since women represent only 22.1% of the energy sector workforce [5]. These statistics confirm the significant gender imbalance present in the global energy sector [5]. The lack of female representation in the renewable energy field can be attributed to traditional gender roles and societal norms dictating suitable professions for men and women. Nevertheless, there is hope that the renewable energy sector, still in its early stages, can afford opportunities to promote gender equality. Recent years have seen increased attention paid to this issue, and

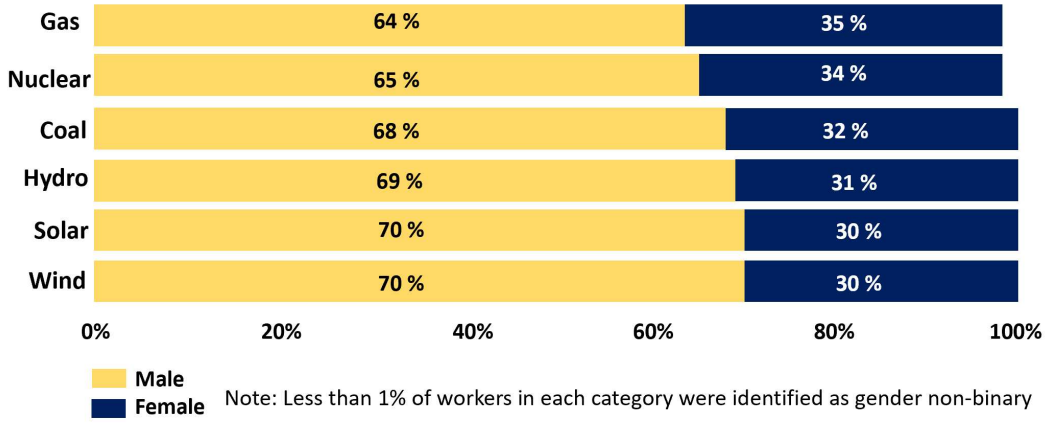

Fig. 1.1 Gender breakdown of workers in electric power generation sectors in the U.S. Source: U.S Department of Energy, United States Energy & Employment Report 2022 [7]

recommendations have been made to enhance women's involvement and decrease gender disparities in the renewable energy industry. This includes the need to improve gender data in order to reflect the diversity of citizens, better inform energy policies, promote women's leadership, and encourage female participation in science, technology, engineering and mathematics (STEM) education. Advancing gender and diversity inclusion in the energy sector can lead to numerous benefits, including enhanced innovation and competitiveness for companies, as well as promoting a more inclusive and equitable socio-economic development through the energy transition [10].

1.2 Research context

The primary objective of the energy transition is to achieve climate neutrality by 2050. The Net Zero Emission by 2050 scenario, also called NZE2050 [2], is a normative scenario made by the International Energy Agency (IEA) to provide guidelines for the global energy sector to achieve net zero CO_2 emissions by 2050 limiting the global temperature rise to 1.5 °C [2]. In this scenario, CO_2 emissions, will fall from 36.6 Gt of 2021 to less than 23 Gt in 2030 (Fig. 1.2b). Then, up to 2040, emissions reductions in the industry and transport sectors should accelerate to almost 10% per year (respectively yellow and red curves in Fig. 1.2a). Among several sectors, the electricity sector (blue curve in Fig. 1.2a) should reach zero net emissions by 2035

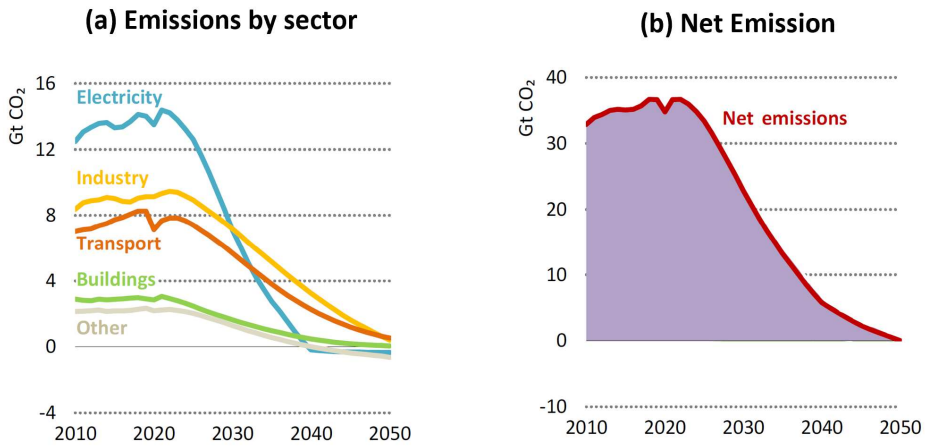

Fig. 1.2 CO_2 emission by sector (a) and total net emissions (b) in the NZE Scenario (2010-2050). Source: IEA 2022; World Energy Outlook [2], License: [CC BY 4.0].

and 2040 respectively for advanced and developing economies. Then, by 2050, all sectors should achieve emissions reductions of more than 90% compared to current levels (Fig. 1.2b) [2]. The NZE Scenario provides a profound transformation as low-emissions sources increase dramatically displacing the *unabated* sources, across the whole energy sector. *Unabated* fossil fuels are those used for energy purposes without Carbon Capture, Utilisation and Storage (CCUS) technology. CCUS technology is able to capture the high concentrations of CO_2 emitted by industrial activities [2]. For example, it is expected that unabated coal falling by nearly one-half and unabated natural gas by more than one-quarter by 2030, reflecting also the global energy crisis and energy security around natural gas sparked by Russia's invasion of Ukrain [2].

In general, decrease in emissions in the energy sector reflects clearly the drop of the fossil fuels energy supply and the improvement of the low-emissions sources (Fig. 1.3). The main goal is to achieve nearly 90% of electricity from renewable energy. In this context, energy storage plays an important role for an increased renewable energy production and for energy security. Indeed, with the growing share of renewables in electricity generation is essential to increase the storage potential (purple rectangle - batteries - in Fig. 1.3) for long periods of time and the flexibility of the energy systems, i.e. by balancing out supply and demand of the generated power [2, 11].

In the transition to a low carbon system, Photovoltaic (PV) and wind technologies are the leading means of reducing electricity sector emissions aiming at increase

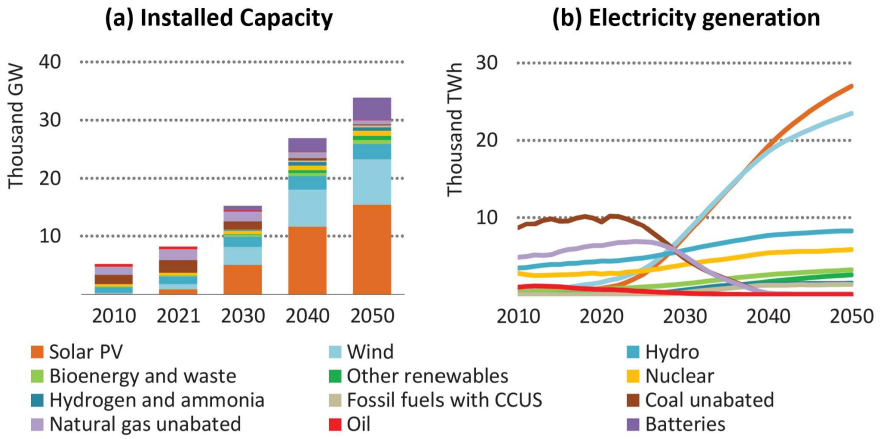

Fig. 1.3 Total installed capacity (a) and electricity generation (a) by source in the NZE Scenario. Source: IEA 2022; World Energy Outlook [2], License: [CC BY 4.0].

their electricity generation from 10% in 2021 to 40% by 2030, and 70% by 2050 (Fig. 1.3, [2]). The carbon footprint of energy production technologies can be estimated by life cycle assessment (LCA) analysis. LCA allows the evaluation of a product over its life cycle, taking into account the specific technology and others factors such as economical and climatic scenarios. An inventory of estimates of greenhouse gas (GHG) emissions predicted for 2022 in different geographical regions is shown in Fig. 1.4 [12]. Coal power shows the highest scores, with a minimum of 753 g CO2

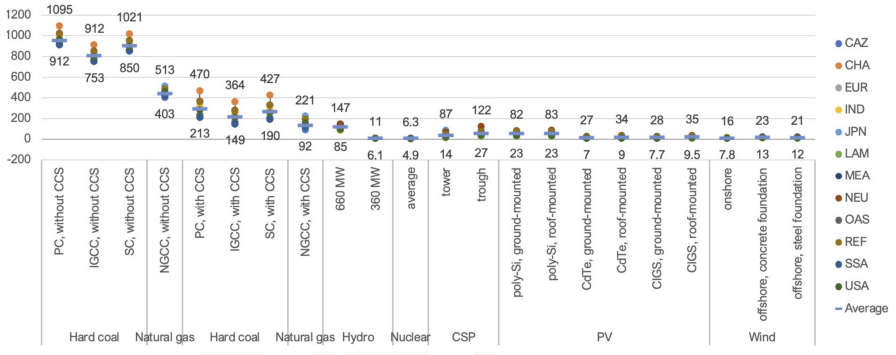

Fig. 1.4 Lifecycle GHG emissions, in g CO2 eq. per kWh, regional variation, 2020 [12]

eq./kWh (IGCC, USA) and a maximum of 1095 g CO2 eq./kWh (pulverized coal (PC), China). Equipped with a carbon dioxide capture facility, and accounting for the CO2 storage, this score can fall to 149–470 g CO2 eq./kWh (respectively). Solar technologies generate GHG emissions ranging from 27 to 122 g CO2 eq./kWh for

concentrated solar PV (CPS), and 8.0–83 g CO2 eq./ kWh for photovoltaics. Wind power GHG emissions vary between 7.8 and 16 g CO2 eq./kWh for onshore, and 13 and 23 g CO2 eq./kWh for offshore turbines.
According to IEA, looking at carbon emissions on global scale, the growth of solar PV and wind power in 2022 helped to prevent around 465 Mt of CO2 emission and further 85 Mt were saved thanks to other green energy technologies [13]. IEA estimates that this has contributed to limit the growth of energy-related CO2 emission in 2022 to about 321 Mt.
Finally, PV and wind sources are considered the most cost-effective alternatives for energy transition. Regarding solar energy, improvement in solar cell technology and financial support have helped to make solar PV capacity competitive with traditional power sources [2]. PV technology is being implemented into a wide range of applications, including building integration, roadway integration, PV-powered batteries, transport, marine, communication, and space applications [14]. Prices for PV modules have reduced by 80% in the last decade, making solar PV the most affordable electricity generation technology in many areas. Nonetheless, in 2021, solar PV only generated about 3% of global electricity production. Hence, substantial investment in PV technology is necessary to minimize its future costs while simultaneously increasing installed capacity, maintaining the trend fixed in NZE50 by IEA [2].

1.3 Research aims and thesis outline

Currently, Silicon (Si) cells dominate the PV market owing to their cost- effectiveness and high efficiency, nowadays approaching the Shockley-Queisser (SQ) limit of $\sim$29 %. A way to overcome this limit is to exploit a tandem structure, where a wide bandgap semiconductor is stacked on top of the silicon cell.
For terrestrial applications, thin-film perovskite technology has emerged as one of the most promising for the development of silicon-based tandems because of the optimal perovskite opto-electronic properties and the fast progress achieved in the last decade. To date, the most used architectures to realize tandem cells are based on 2-Terminal (2T) and 4-Terminal (4T), while the 3-Terminal (3T) solution, despite their predicted championship energy yield [15], is less explored. Some promising proof-of-concept devices have been reported, that use a silicon cell with interdigitated back contact

(IBC).
In this thesis, we propose a novel 3T-tandem architecture based on the Heterojunction Bipolar Transistor (HBT) structure, that was proposed in 2015 [16] for the realization of three-terminal double junction cells.
The 3T-Heterojunction Bipolar Transistor (3T-HBT) solar cell architecture offers an attractive alternative to realize monolithic PVK/Si (PVS) tandem solar cells compatible with Si photovoltaic technologies such as Aluminum Back-Surface-Field (AL-BSF), Passivated Emitter Rear Cell (PERC), and Silicon Hetero-Junction (SHJ) that are less expensive and more widely adopted than the IBC one. The 3T-HBT architecture overcomes several constraints of the series connected Double Junction (DJ) cell, i.e. current matching and the need of tunnel junctions or recombination layers, exploiting a simpler multi-layer structure and achieving efficiency as high as that one of the 2T tandem for optimum combination of energy bandgaps, and higher efficiency than the 2T tandem for sub-optimal gap choices because of the lack of series current constraint.
With the aim of contributing to the development of an attractive possible candidate for high-efficiency next-generation PV devices, this thesis presents a comprehensive research work to study how the HBT solar cell architecture could be used to realize monolithic 3T-PVS tandem solar cells. The thesis is organized in seven Chapters and four Appendices:

Chapter 2 reviews the basic features of solar cells, discussing their efficiency limitations. Then, a section is dedicated to perovskite and silicon technologies and to the different architectures that can be used to realize perovskite/silicon tandems. To complement this introduction, Appendix A describes the experimental work on the development and characterization of a two-step hybrid deposition process of perovskite materials, that I carried out during my four month research stay at Tor Vergata University.

Chapter 3 starts by reviewing the theoretical limiting efficiency of a 2T and 3T-HBT perovskite/silicon tandems, according to the detailed balance approach. Then, the operation of the 3T-HBT solar cell is explained in detail with the aid of a compact analytical model that I developed as a generalization of the well-known Hovel model for single junction cells. This provides a solid background for the critical interpretation of the advanced numerical simulations presented in the following chapters

aimed at developing realistic device designs. Appendices B and C complement the chapter with mathematical details of the models.

Chapter 4 describes the modeling tool flow adopted in Sentaurus Technology Computer-Aided Design (TCAD) for the coupled optical and transport numerical simulations of 2T and 3T-HBT tandems. Results in Chapter 5 and Chapter 6 are based on the opto-electronic model discussed here.

Chapter 5 presents a possible implementation of a planar (*n-p-n*) 3T-HBT tandem with silicon heterojunction bottom cell, whose photovoltaic performance are analyzed and compared to a benchmark 2T cell. Then, a textured PVS (*n-p-n*) HBT device is introduced. Moreover, the numerical model is validated against experimental data. The presented devices show promising performance and the comparative analysis with 2T cells with similar multilayer stack confirms, on a ground closer to the practical realization of the device than detailed balance models, that the efficiency of the 3T-HBT tandem can be as high as that one of a perfectly current-matched 2T tandem.

Chapter 6 deals with the most relevant potential drawback of the 3T-HBT device, i.e. the realization of the third contact at the base middle layer. In this regard, we elaborate on the feasibility of the HBT structure for 3T perovskite/silicon tandem solar cells with top interdigitated contact layout in the perspective of scaling up to large areas. To this aim, a modeling framework that mixes numerical physics-based simulations and circuit simulations is exploited, wherein parasitic electrical loss are described through a lumped modeling approach, whose details are given in Appendix D.

Finally, Chapter 7 summarizes the main outcomes of this work.

Chapter 2

Photovoltaic technology: physics and materials

The history of PV device dates back to the 19th century, when French physicist Edmond Becquerel discovered the photovoltaic effect in 1839. He noticed that certain materials, when exposed to light, generated an electric current. A few decades later, in 1883, the first working PV device was built by Charles Fritts with an energy conversion efficiency of only 1% [17]. However, it was not until the mid-1950s that scientists at Bell Laboratories, developed the first practical solar cell made of Silicon achieving an efficiency of 6%. This breakthrough paved the way up to the actual exploitation of solar cells in space and recently in terrestrial applications.
The efficiency of a PV cell, that is how effectively it converts sunlight into electricity, can be affected by several factors. Here, we will address the operating principle and basic features of PV cells, also focusing on the different efficiency losses linked to the material properties and device architecture.
Today, research continues focusing on improving the efficiency of PV cells by addressing these various sources of loss, and developing new materials and device designs.

2.1 Solar cell: theoretical background

Solar or photovoltaic cells are devices able to convert solar energy into electricity (exploiting the so-called photoelectric effect) [18]. To attain this effect, it is required a material where photons are absorbed and photogenerated charges are subsequently injected from the solar cell into an external circuit.

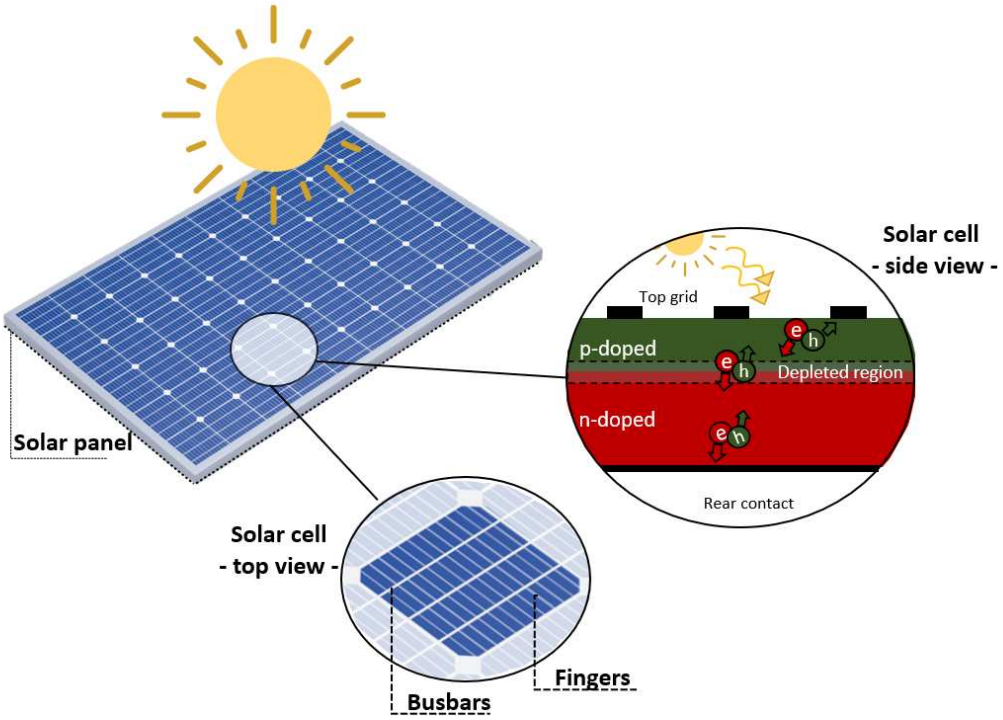

Fig. 2.1 General sketch of a typical solar panel. The enlarged sections illustrate the p-n junction under illumination (solar cell - side view) and a common scheme of top contact grid where fingers and busbars are highlighted (solar cell - top view).

The simplest solar cell consists on a *p-n* junction [1] (Fig. 2.1, side view), with a front ohmic contact grid, featured by fingers and busbars (Fig. 2.1, top view), and a rear ohmic contact covering the whole back surface.

[1] a *p-n* junction is formed when a *p*-type semiconductor, that contains a large concentration of holes (p_p, *majority carriers*) and few electrons (n_p, *minority carriers*), is in intimate contact - at crystal level - with a *n*-type semiconductor, with a high concentration of electrons (n_n, *majority carriers*) and few holes (p_n, *minority carriers*) [19]. The *p-n* interface is characterized by a negative space charge formed in the *p*-side of the junction and a positive space charge formed in the *n*-side. Thus, the overall *space charge region* creates an electric field in the direction opposite to the diffusion current for each type of charge carriers. The region is also called *depletion region* since it is depleted of free charge carriers.

2.1.1 *pn* junction under illumination

When the solar cell is under illumination condition, a photon that has energy $h\nu$ [2] lower than the bandgap E_g [3] makes no contribution to the cell output, a photon that has an energy greater than E_g is absorbed into the semiconductor delivering its energy to an electron that from the *valence band* (E_v in Fig. 2.2a) is excited to the *conduction band* (E_c in Fig. 2.2a), creating an electron-hole pair.

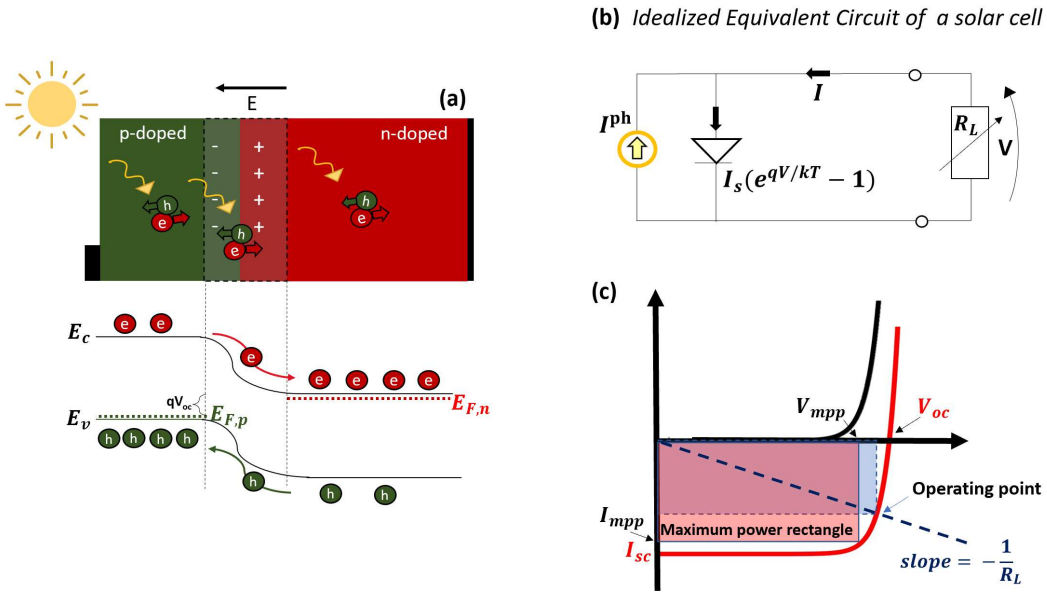

Fig. 2.2 (a) Energy band diagram of a *p-n* junction solar cell under illumination condition (b), idealized equivalent circuit of a solar cell (c) and *J-V* characteristics of a solar cell under illumination (red curve) and under dark condition (black curve).

In Fig. 2.2a, photogenerated electron minority charges (red dashed arrow, n_p) and hole minority charges (green dashed arrow, p_n), under the effect of the local electric field, sweep towards their respective contacts, and once injected in the external circuit they release an energy $\simeq E_g$ to the load in form of work. Energy greater than E_g is dissipated as heat, through carrier thermalization. Due to the current flow through the external load, the *p-n* junction is self forward biased. The difference between the two quasi-Fermi levels $E_{F,n}$ and $E_{F,p}$ [4] is equal to qV_{oc}, V_{oc} being the open-circuit

[2] here, h is the Planck's constant and ν is the frequency of light [19].

[3] A semiconductor material is characterized by a *bandgap energy* E_g between the top state of the *valence band* and the bottom one of the *conduction band*.

[4] Under illumination, electron and hole concentrations (n and p) are higher than those in *equilibrium* state, such that $pn > n_i^2$. Similarly to *equilibrium*, in which the Fermi level (E_F) determines the

voltage. Semiconductors with bandgap between 1 and 2 eV can all be considered suitable solar cell materials.

The *ideal equivalent circuit* of a solar cell is shown in Fig. 2.2b where I_{ph} is the photogenerated current, I_s is the reverse saturation current and R_L is the external load. The ideal $I-V$ characteristic for a *p-n* junction under illumination condition is given by:

$$I = I_s(e^{qV/n_{if}k_BT} - 1) - I_{ph} \tag{2.1}$$

where q is the elementary charge constant, V the voltage of the solar cell, k_B the Boltzmann constant, T the temperature, and n_{if} the ideality factor. Eq. 2.1 is often expressed in terms of current density $J = I/A$ where A is the device area. The current-voltage characteristic of Eq. 2.1 is shown in Fig. 2.2c, where several figures of merit need to be introduced:

- I_{sc} is the short-circuit current, occurring when the cell's voltage is zero (Fig. 2.2c, load in short-circuit)
- V_{oc} is the open-circuit voltage, occurring when the cell's current is zero (Fig. 2.2c, load in open circuit)
- I_{mpp} and V_{mpp} are the current and voltage, respectively, corresponding to the operating point at which the power is maximized (maximum power point, MPP).
- The Fill Factor, FF, indicates the ratio between the power at maximum power point (P_m=$I_{mpp}V_{mpp}$) (red rectangle in Fig. 2.2c) and the product $I_{sc}V_{oc}$:

$$FF = \frac{I_{mpp}V_{mpp}}{I_{sc}V_{oc}} \tag{2.2}$$

- The intersection point between the *J-V* curve under illumination (red curve) and the load (with slope -1/R_L) identifies the *operating point* of the solar cell since in that point the load and the solar cell have the same current and voltage (Fig. 2.2b). To maximize the solar cell performance it is important to choose a proper load to match the operating point with the maximum power point.

probability of carrier occupation at a certain energy level, in *non-equilibrium* state the *quasi-Fermi* levels $E_{F,n}$ and $E_{F,p}$ are used to determine the occupation of a certain energy states by electron and hole populations, separately. [19].

The power conversion efficiency of the solar cell is given by

$$\eta = \frac{I_{\text{mpp}} V_{\text{mpp}}}{P_{\text{in}}} \tag{2.3}$$

where P_{in} is the incident power density from the sun. Fig. 2.3 shows different Solar

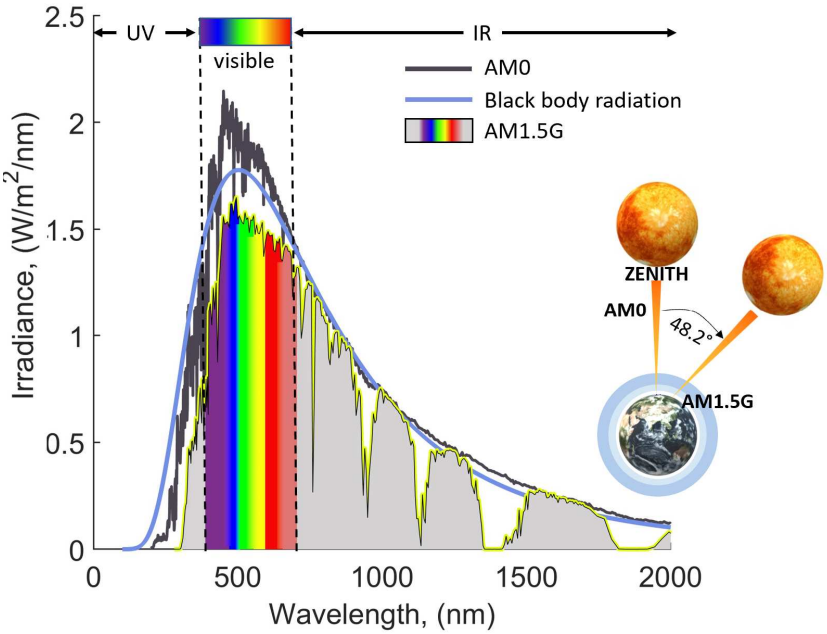

Fig. 2.3 AM0 extraterrestrial radiation (black line), Solar spectral intensity for black-body radiation at 5762 K (blue line), AM1.5 radiation (grey and rainbow filled shape).

Irradiance (E_{sun}) spectra, classified according to the Air Mass (AM), and the Planck Solar Irradiation [5]. In general, the E_{sun} with AM0 (total power of ≈ 1366 W/m^2) is used for space applications, instead E_{sun} with AM1.5G, with a total power density of 1000 W/m^2, is used for terrestrial applications. In this case, the solar spectra that arrives on the earth surface is attenuated due to the thick layer of atmosphere and the path of the light crossing it in order to reach the earth's surface [20]. From a specific E_{sun}, it is possible to define the number of photons per unit of time arriving on the solar cell surface, that is the Spectral Photon Flux (SPF) $\phi_0(\lambda)$ defined as:

$$\phi_0(\lambda) = \frac{E_{\text{sun}}(\lambda)}{h\nu} \tag{2.4}$$

[5]The amount of photons emitted by the Sun can be modeled by the Planck's law for a black-body whose surface temperature is equal to $T = 5762$ K.

The short circuit current density (J_{sc}) can be expressed as:

$$J_{sc} = \int_{\lambda_{min}}^{\lambda_{max}} q\phi_0(\lambda)EQE(\lambda)d\lambda = \int_{\lambda_{min}}^{\lambda_{max}} q\phi_0(\lambda)A(\lambda)IQE(\lambda)d\lambda \tag{2.5}$$

where λ is the wavelength in the E_{sun} range of interest, EQE(λ) is the external quantum efficiency, IQE(λ) is the internal quantum efficiency and A(λ) is the absorbance, expressed as:

$$A(\lambda) = \frac{\text{number of absorbed photons}}{\text{number of incident photons}} \tag{2.6}$$

Assuming a unitary quantum yield, i.e. one e-h pair generated for each photon absorbed, the IQE is defined as

$$IQE(\lambda) = \frac{\text{number of collected charge carriers}}{\text{number of absorbed photons}} \tag{2.7}$$

The EQE accounts for both optical and electrical loss mechanisms. It can be written as:

$$EQE(\lambda) = \frac{\text{number of collected charge carriers}}{\text{number of incident photons}} = A(\lambda)IQE(\lambda) \tag{2.8}$$

The power conversion efficiency (Eq. 2.3) of a solar cell has two main limitation factors:

- for small material E_g, the efficiency is limited by a low V_{oc}, that is proportional to the material bandgap;
- for a high E_g, the efficiency is limited by a low J_{sc} since the semiconductor is not able to absorb low energy photons.

The theoretical maximum efficiency of a single-gap E_g solar cell, that is the best trade-off between the V_{oc} and J_{sc}, can be estimated from the detailed balance model, also known as Shockley-Queisser model. Fig. 2.4 reports the SQ efficiency limit of single gap cells as a function of the material energy bandgap. The calculation has been done assuming complete absorption of photons with energy larger than the bandgap. Other details follow [22].

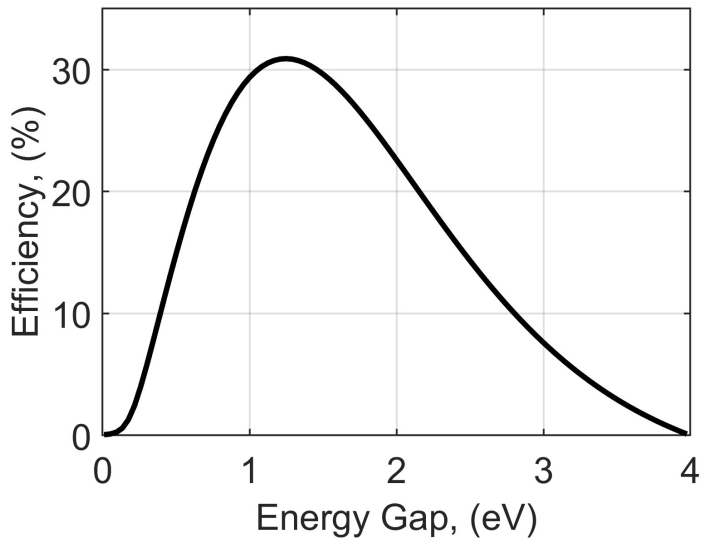

Fig. 2.4 Detailed balance limit of efficiency obtained by implementing the model in [22]. It is assumed a solar cell at temperature $T_c = 300$ K exposed to a blackbody radiation at temperature $T_s = 5762$ K (blue curve in Fig. 2.3 with a total power of ≈ 1300 W/m^2)

.

2.1.2 Loss mechanisms

Many factors can limit the efficiency of a solar cell to values below the detailed balance one: *recombination* mechanisms in the semiconductor, optical losses due to parasitic absorption or unabsorbed photons as well as resistive losses. Let's analyze the nature of the outlined mechanisms. Details can be found in [19].

Recombination losses

Under illumination, *absorption* of photons and electron-hole pair *generation* (represented by the photo-generation rate G_{ph}) brings the *p-n* junction into a $non-equilibrium$ state ($pn > n_i^2$). Whenever the steady-state is disturbed, the entire system aims to restore the equilibrium state (i.e. $pn = n_i^2$). This mechanism is the reverse process of the *generation* and it is known as *recombination* process, such that an electron and hole recombine resulting in a release of energy. Thus, generation and recombination refer respectively to the creation and annihilation of electron-hole pairs [19].
There are several mechanisms that lead to recombination of charge carriers:

- Radiative recombination
- Auger recombination
- SRH recombination
- Surface recombination

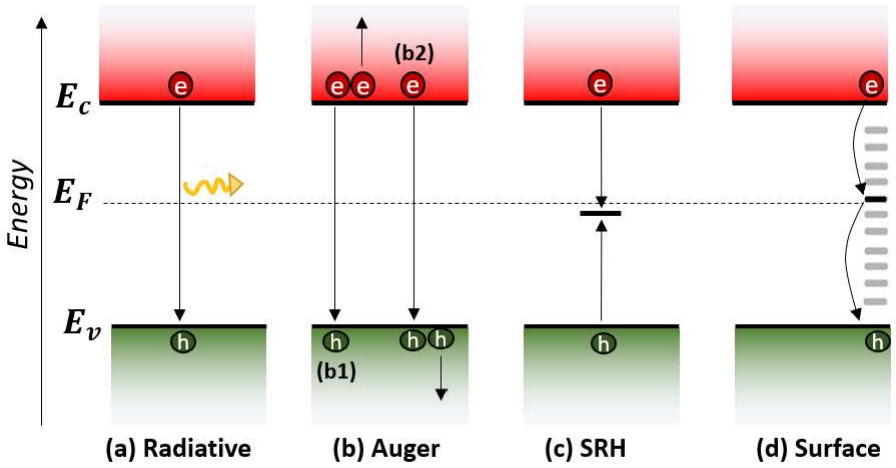

Fig. 2.5 Recombination mechanisms: (a) Radiative; (b) Auger: b1 refers to an electron assisted process and b2 to a hole assisted process; (c) Shockley-Read-Hall; (d) Surface recombination.

Among them, we can distinguish between *intrinsic* recombination mechanisms, that are related to the material property and cannot be avoided and, *extrinsic* recombination related to the impact of defects.

Radiative recombination is the spontaneous recombination of an electron-hole pair, resulting in photon emission. In Fig. 2.5a, electron makes a transition from the conduction band E_c to the valence band E_v by emitting a photon of energy similar to the band gap E_g. The radiative recombination is the reciprocal process of the absorption, limiting the maximum theoretical efficiency of a solar cell. For example, for a semiconductor with a bandgap of 1.1 eV (i.e. Silicon), the radiative recombination mechanism sets the Shockley-Queisser limit to $\sim$31.5% (Fig. 2.4) [21]. More details about SQ limit can be found in Appendix B.

Auger recombination, illustrated in Fig. 2.5b, involves three charge carriers: the

energy released by a band-to-band e-h recombination is provided to an electron (or to a hole) that is excited to a higher energy state. When two holes (electrons) and one electron (hole) are involved, the Auger process is referred as *hhe* (*eeh*) process (shown as process b2 (b1) in Fig. 2.5b). Auger recombination is mostly important at high carrier concentrations caused by heavy doping or high level injection. Auger recombination turns to be the most severe physical limitation to the charge carrier lifetime in c-Si and therefore to the solar cell efficiency. In this regard, accounting for Auger recombination, the ultimate efficiency limit for a c-Si solar cell is $\sim$29%.

Shockley-Read-Hall recombination mechanisms, illustrated in Fig. 2.5c, is related to the recombination through defects. Defects introduce energy states in the band structure. Electrons and holes transit to these energy levels, and recombine in them.

To take into account the effect of all the recombination mechanisms, it can be defined a minority carrier *lifetime* $\tau_{n,p}$ that refers to the average time it takes for a free charge carrier (either an electron or a hole) to recombine. The carrier lifetime (τ) can be formulated as:

$$\frac{1}{\tau} = \frac{1}{\tau_{rad}} + \frac{1}{\tau_{Auger}} + \frac{1}{\tau_{SRH}} \tag{2.9}$$

where τ_{rad}, τ_{Auger} and τ_{SRH} refer to the *Radiative*, *Auger*, *SRH* lifetime, respectively. Extended equations can be found in Chapter 4. Another important parameter related to the recombination rate is the minority carrier *diffusion length*

$$L_{n,p} = \sqrt{D_{n,p}\tau_{n,p}} \tag{2.10}$$

where $D_{n,p}$ is the diffusivity coefficient. It is a measure of the distance that an hole or electron minority carriers can travel before recombining. The larger the diffusion length, the more efficient the solar cell. In fact, photogenerated carriers have a higher chance of reaching the metal contacts without recombining. Thus, in order to design an efficient solar cell, both recombination lifetime and the diffusion length must be taken into account.

Surface recombination is another important phenomena in solar cells. It involves air-semiconductor, semiconductor-semiconductor or semiconductor-insulator inter-

faces where defects can occur. These defects are caused by interruptions to the crystal lattice's periodicity, leading to dangling bonds at the semiconductor surface. Similarly to the SRH recombination, defects act as intermediate energy states in the band structure, as shown in Fig. 2.5d. The parameter $S_{n,p}$, that is the surface recombination velocity (cm/s), is used to quantify the rate at which minority carriers are recombined at the surface of the semiconductor material. Surface recombination hinders the power conversion efficiency of solar cells by reducing the number of carriers available for collection in the external circuit. To minimize surface recombination, various methods can be used, such as *passivation* of defects. For example, passivation technique is used in heterojunction Silicon solar cell where Silicon surface is passivated with hydrogen, that is forming a link between *dangling bonds* (i.e. defects) and hydrogen to reduce recombination traps.

Optical losses

Ideally, when the solar cell is under illumination, all photons should cross the surface and be photoactive in the absorber layers. However, in real solar cells there are several losses sources that can diminish the optical path of photons and their absorption.

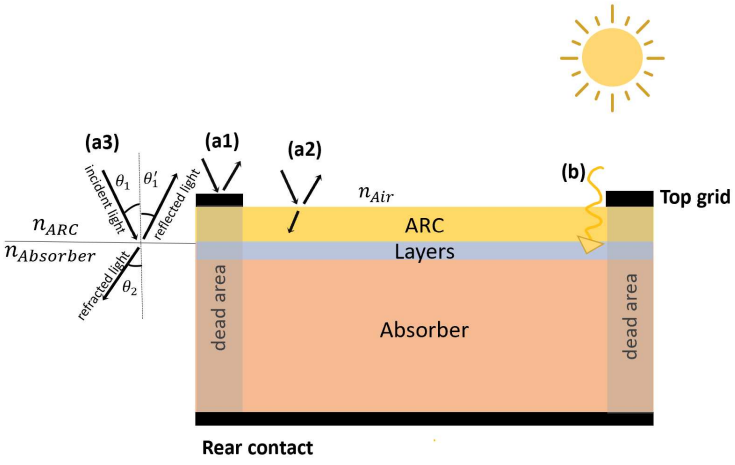

Fig. 2.6 Opticall losses: (a) reflection and (b) parasitic absorption.

In Fig. 2.6, we summarize the potential causes that can reduce the photon absorption by degrading the short circuit current J_{sc}. As seen in Fig. 2.1, solar cells exploit top/rear metal grid to provide current to the external load. Thus, top metal

grid shadows part of semiconductor material (*dead area* in Fig.2.6) by reducing the area effectively available to absorb photons. Photons are reflected at the front grid (Fig. 2.6a1). Photons that impinge in the non-shadowed area, depending on the wavelength, cross several material layers before being absorbed. Through this path, they can be reflected/refracted at each interface based on the refractive index of the material (n_{layer} in Fig. 2.6) and based on the incident angle of light at the surface (Fig. 2.6a2) and interfaces (Fig. 2.6a3). In this regard, considering a single interface and normal incidence of light on the solar cell surface, the fraction of reflected light, i.e. the reflectance, can be computed through the Fresnel equation:

$$R = \left| \frac{\tilde{n}_1 - \tilde{n}_2}{\tilde{n}_1 + \tilde{n}_2} \right|^2 \tag{2.11}$$

where $\tilde{n}$ is the complex refractive index $\tilde{n} = n - ik$ and k is the extinction coefficient. The highest the reflectance, the lowest the amount of photons absorbed into the solar cell. In this thesis, MgF_2 layer is used as Anti-Reflection Coating (ARC) to decrease the amount of reflected photons at the interface air/semiconductor.
Another optical loss mechanism is related to those layers aimed at improving electrical performance and placed on the active region, such as ITO (Indium Thin Oxide) as well as transport layers (Fig. 2.6b). These layers are not completely transparent and absorb low wavelength photons that should ideally be absorbed by the active region. As a result, e-h couples generated in these layers recombine quickly before being collected, hence worsening the IQE [23].
Once reached the photoactive region, photons are absorbed depending on the material thickness and absorption coefficient α (cm^{-1}). According to the Beer-Lambert law [24], the photon flux ($\phi(x)$) decreases exponentially as a function of depth. For the case of no back reflector, $\phi(x)$ can be written as:

$$\phi(x,\lambda) = (1 - R(\lambda))\phi_0(\lambda)e^{-\alpha(\lambda)x} \tag{2.12}$$

where $\phi_0(\lambda)$ is the incident photon flux and the expression of α is:

$$\alpha = \frac{4\pi k}{\lambda} \tag{2.13}$$

The absorption coefficient determines how far into a material photons of a particular wavelength can penetrate before they are absorbed. The intensity of photons incident

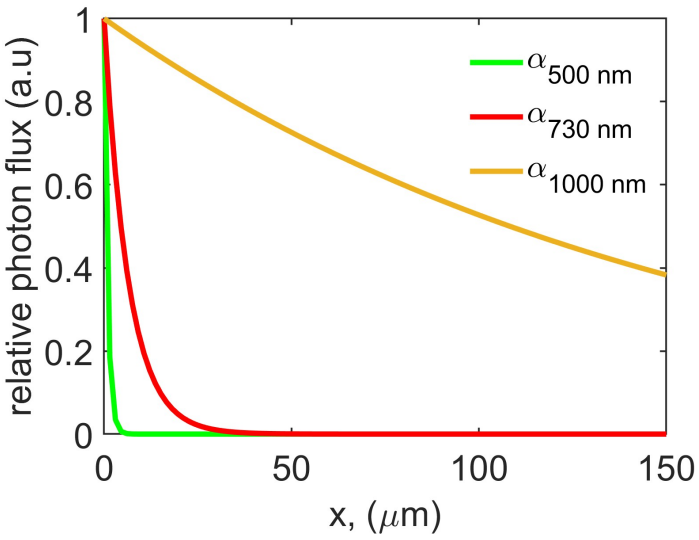

Fig. 2.7 Relative photon flux (ϕ/ϕ_0) for a Silicon wafer.

on a solar cell surface reduces by a factor of $1/e$ for each $1/\alpha$, that is the *absorption length* (Fig. 2.7) [18]. A low absorption coefficient means that the material poorly absorbs light, and if the material is thin enough it can appear as transparent at certain wavelength. Hence, photons can enter the material and pass through without being absorbed. For example, in Fig. 2.7, depending on the $\alpha(\lambda)$ of the Si material, light is absorbed at different depths (green or red curve) or escapes without being absorbed (orange curve). To design high efficient solar cells, it's crucial to optimize the ratio between light penetration depth and thickness of the cell in order to maximize the solar spectrum absorption. Additionally, the diffusion length also poses a significant constraint on solar cell thickness to prevent recombination of e-h carriers before being collected. In conclusion, designing an efficient solar cell requires considering multiple factors, including material optical and electrical properties, layers' thickness and, and device structure. For example, a possible solution to enhance the collection of long-wavelength photons is by exploiting a rear contact extended to the whole surface (Fig. 2.6). In this way, photons that are not absorbed in the first pass through the absorber layer can be reflected by the metal contact and re-absorbed in the active layer. A further approach to reduce optical losses is to exploit textured surfaces (Fig. 2.8) that increase significantly the path length (blue arrows in Fig. 2.8b) of weakly absorbed, long-wavelength photons ensuring that they can be absorbed in the active region.

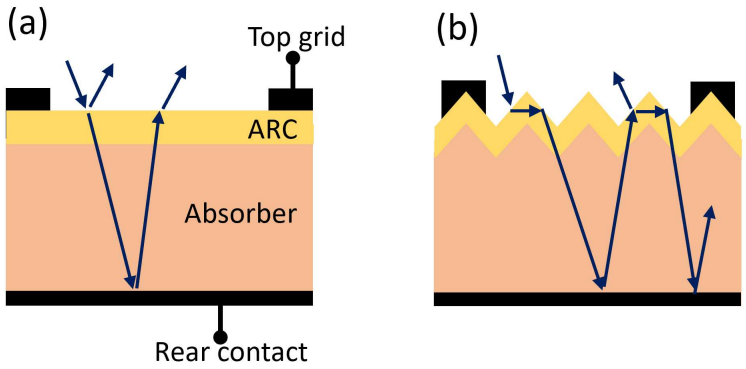

Fig. 2.8 Sketches of light path in planar (a) pyramidal texture (b) solar cell.

Resistive losses due to the front grid metal contact

An important factor that degrades the solar cell efficiency is due to resistive effects associated to the transport of photogenerated charges towards the contacts. For example, in Fig. 2.9a, photogenerated holes cross laterally the *p*-semiconductor, with a certain resistivity, towards the finger electrodes and then to the busbar before being collected.

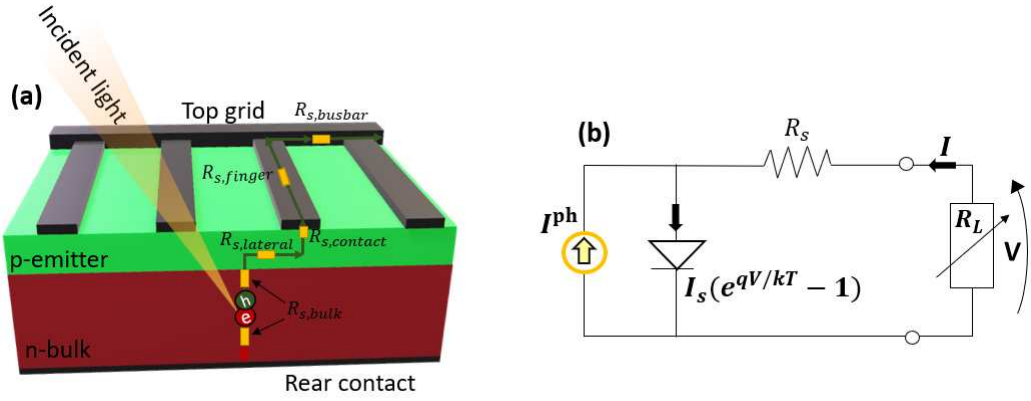

Fig. 2.9 (a) Schematic view of resistive parasitic losses from generation to collection at the contacts and (b) equivalent circuit of a solar cell taking into account series resistance.

To take into account resistive effects, in the one-diode model of Fig.2.2b, an equivalent lumped series resistance is introduced. R_s (Ωcm^2) models all the resistive effects (Fig. 2.9a) through the cell. Fig. 2.2b can be redrawn as in Fig. 2.9b.

The resistance R_s can be expressed as follows:

$$R_s = R_{s,bulk} + R_{s,lateral} + R_{s,contact} + R_{s,finger} + R_{s,busbar} \tag{2.14}$$

where $R_{s,lateral}$ and $R_{s,bulk}$ account for the lateral (in the emitter layer) and orthogonal (in the bulk layer) current flow, respectively; $R_{s,contact}$ is the contact resistance at the interface emitter/contact, $R_{s,finger}$ and $R_{s,busbar}$ account for the series resistance of the metal finger and busbar.
In general, the series resistance $R_{s,bulk}$ is small due to the bulky volume, instead the other contributions in Eq. 2.14 tend to be higher and a proper grid layout must be designed to minimize them. Taking into account R_s, Eq. 2.1 can be rewritten as follows:

$$I = I_s(e^{q(V-IR_s)/n_{if}k_BT} - 1) - I_{ph} \tag{2.15}$$

Depending on the value of the series resistance, the FF gets worse reducing the achievable power. Resistive losses can be mitigated through technology improvements, such as decreasing finger pitch (while decreasing finger width to maintain a low shadowing) as well as exploiting multi-busbar layouts.
For the sake of completeness, we highlight that other power loss can be modeled by including in the equivalent circuit a shunt resistance (Fig. 2.10), that is mainly related to material non-idealities such as defects.

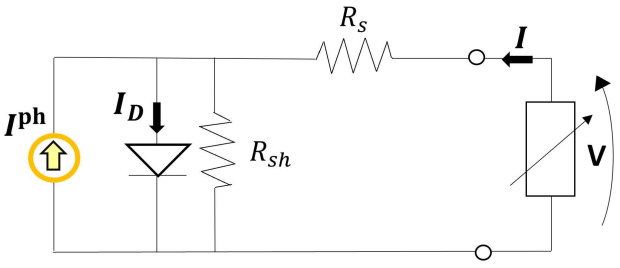

Fig. 2.10 Equivalent circuit of a solar cell taking into account series and shunt resistance.

To take into account the shunt resistance R_{sh}, Eq. 2.15 can be rewritten as follows:

$$I = -I_{ph} + I_s(e^{q(V-IR_s)/n_{if}k_BT} - 1) + \frac{V - IR_s}{R_{sh}} \tag{2.16}$$

2.2 Status and perspective of Perovskite/Silicon solar cells

For efficient PV effect, it is necessary to exploit a semiconductor material that absorbs efficiently light, generating free charges then delivered to the external load. To date, Silicon solar cells dominate the terrestrial PV market with a practical efficiency of 26% [25] and module efficiency of 24.4% [26]. Other alternatives exist, such as CdTe or CIGS technology (green lines in Fig. 2.11) with efficiencies above 19% [26]. However, they have difficulty to compete due to the better efficiency/cost ratio of Silicon cells [25]. In this regard, the module minimum sustainable price (MSP) of different c-Si technologies ranges between $0.25/W and $0.27/W; CdTe modules have a slightly higher MSP of $0.28/W, instead for CIGS modules the MSP increases up to $0.48/W owing to higher labor and equipment/facility costs [27].
Promising performance could be expected for perovskite cells (brown line with yellow circles in Fig. 2.11) that are currently in small scale or pilot production. The MSP of perovskite modules at small production scale is estimated to be $0.38/W for 2020, with potential cost reductions over the long term to $0.18/W if performance will be improved without incurring additional costs [27]. The major challenge of

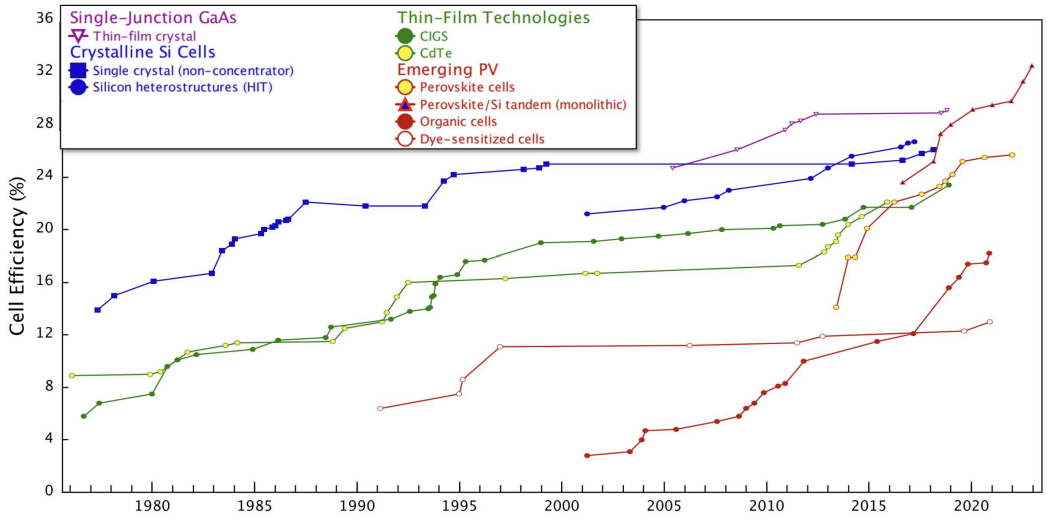

Fig. 2.11 NREL chart [28] of the highest conversion efficiencies for terrestrial research cells.

perovskite solar cell relies on the native perovskite technology that is particularly sensitive to intrinsic and extrinsic degradation mechanisms, such as those caused

by contact with air moisture, by exposure to UV light and high temperature or by electrical biasing [25]. Other technologies such as organic or dye-sensitized solar cells (brown lines in Fig. 2.11) show a low efficiency (below 15%) such that they are not competitive in the prospect of mass energy production systems. Finally, although GaAs single junction solar cells show the highest efficiency of 29.1% (purple line in Fig. 2.11), their manufacturing costs are still too high, more than 100 times higher than Si cells, to enter in the terrestrial PV market. Thus, an open question is how to obtain a solar cell that combines high efficiency, greater than the theoretical limit of Si cell, and low manufacturing costs. To date, one of the most promising candidates for next generation photovoltaics [29] relies on perovskite/silicon (PVS) tandem solar cells, that recently achieved the efficiency record of 33.7% [28], surpassing that one of costly III-V double-junction solar cells [28]. The cost analysis proposed in [30] estimated a MSP of 0.31 $/W in 2020 for a PVK/silicon tandem with 28% efficiency, that could be almost halved by 2030 if the efficiency is increased to 30%. In this regard, Si-tandem cells could relax at some extent several constraints related to the instability problem of PVK cell that sets its best lifetime up to 10,000 h (around 1 year), but with a low efficiency $\approx$ 12% and only 1000 h with an efficiency of 20 % [31]. In [31], it was estimated that a lifetime of 15 years would be the threshold for perovskite PV (with a PCE of 19 % and module size of at least 100 cm^2) to hit a target LCOE of 5.50 US-cents/kWh to enter the PV market.

2.2.1 Silicon solar cell technology

Silicon, in its crystalline form (c-Si), is the most exploited to produce PV modules, with a market share of 90%. The reason of this success relies on the fact that Silicon is the second most abundant element after oxygen in the Earth's crust and, in the last decade, manufacturing costs have been significantly decreasing [20]. As shown in Fig. 2.12, since 1980 Si solar cells improved their performance achieving an efficiency of 26.7% [26], close to their theoretical limit of 29% [21]. Until 2018, the most exploited solar cells were based on *p*-doped wafer, where the rear contact was extended to the whole bottom surface. This kind of solar cell is known as Aluminum Back-Surface-Field (Al-BSF) solar cell, shown in Fig. 2.13a where the *n*-emitter is highly doped and a passivating layer is used to reduce recombination at the emitter/contact interface. In this regard, the main problem of the BSF architecture relies on the extraction of charge carriers due to the direct full-area metal

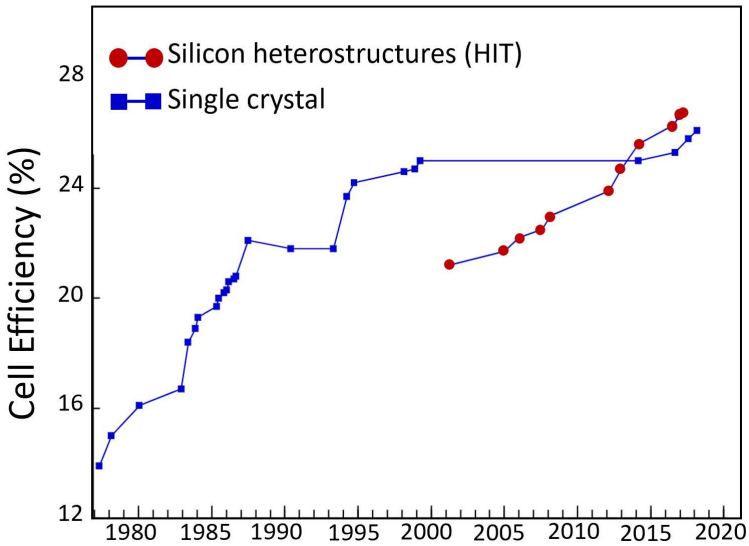

Fig. 2.12 NREL chart [28] of the highest conversion efficiencies for Silicon homojunction and heterojunction research cells.

contact-semiconductor interface that causes high surface recombination, by limiting the efficiency just above 20% [25]. The Passivated Emitter Rear Cell (PERC) architecture, shown in Fig. 2.13b, overcomes this drawback by reducing the metal contact area and passivating the surface between the metal contact and the active area, achieving an efficiency of 24% [25]. In the last decade, a fast industrial transition from Al-BSF to PERC took place and at the end of 2020 more than 70% of the cell market was PERC technology based [25]. An improvement to the standard PERC in Fig. 2.13(b) relies on a different architecture that exploits Interdigitated Back Contact (IBC) (Fig. 2.13(c)). The IBC architecture avoids shadowing due to the front metal grid putting both contacts on the rear side of the cell.

Finally, an emerging technology relies on Silicon Hetero-Junction (SHJ) solar cell with front/rear contacts (Fig. 2.13d), initially called Heterojunction with Intrinsic Thin layers (HIT), and SHJ with IBC (Fig. 2.13e) [25]. SHJ-IBC (Fig. 2.13e) solar cell achieved an efficiency of 26.7% [26], instead SHJ device (Fig. 2.13d), contacted on both sides, holds an efficiency of 25.3% [26]. With respect to PERC solar cell, SHJ technology uses different passivating contacts based on hydrogenated amorphous Silicon (a-Si:H), providing good surface passivation to c-Si. As shown in Fig. 2.13d, the HIT subcell consists of a *n*-doped c-Si sandwiched between two thin-films of hydrogenated amorphous Silicon: from the top (bottom) the *n (p)* -type

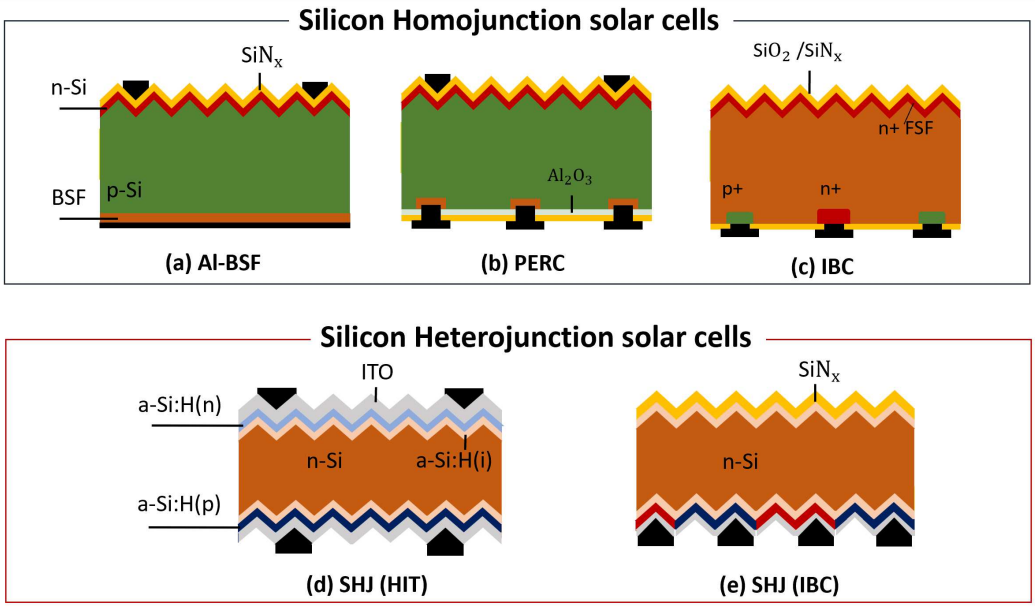

Fig. 2.13 Schematic representaion of Si solar cell architectures: (a) Al back-surface field (Al-BSF) homojunction solar cell, (b) passivated emitter rear contact (PERC) homojunction solar cell, (c) rear-contacted homo-junction using an interdigitated back contact (IBC), (d) Silicon hetero-junction (SHJ or HIT) design, (e) IBC design of SHJ solar cell [25].

a-Si:H and a thin intrinsic (*i*) a-Si:H layer. The (*i*)a-Si:H layer (< 10 nm) is used between the Si-wafer and the *n* (*p*)-doped a-Si:H layer to improve surface passivation. In fact, doping of the a-Si:H layers is not as efficient as in c-Si and by putting doped a-Si:H directly in contact with c-Si would not provide an excellent passivation.
In Fig. 2.13d, the Indium Thin Oxide (ITO) is a Transparent Conductive Oxide (TCO) used to improve the lateral transport towards the front and rear metal grid. In this regard, we will discuss in Chapter 6 about the inefficient charge transport in a-Si:H layers, compared to c-Si, due to its low mobility. A key feature of such Silicon heterojunction (SHJ) devices is their high V_{oc}, typically of 730–750 mV [25].

2.2.2 Perovskite solar cell technology

Perovskite (PVK) is originally the mineral name of calcium titanate ($CaTiO_3$), then it is applied to the class of materials showing the same structure of $CaTiO_3$. For PV applications, organic-inorganic lead halide perovskites are the most studied, with chemical structure AMX_3, where A (= cesium (Cs^+), methylammonium (MA^+) and/or formamidinium (FA^+)) are monovalent cations, M (= lead (Pb^{2+}) and/or

stannous (Sn^{2+})) are metal cations, and X (= iodide (I^-), bromide (Br^-), or chloride (Cl^-), or combinations thereof) are halide anions.

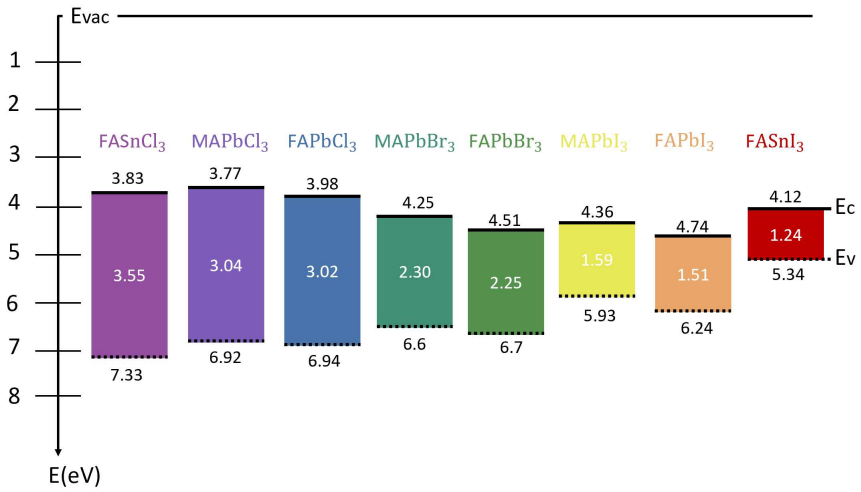

Fig. 2.14 Schematic energy level diagram showing the conduction and valence band edges of some metal halide perovskites [32].

They emerged as promising candidates for PV applications owing to their extraordinary optical and electrical properties such as high absorption coefficients, low exciton binding energy, bandgap tunability (Fig. 2.14), ambipolar transport characteristics, excellent carrier mobilities, long carrier lifetimes, long carrier diffusion lengths and high defect tolerance [14]. One of the main intriguing property is the tunability of the band-gap based on the perovskite composition. Some perovskite compositions are reported in Fig. 2.14 [32], with bandgap ranging from 1.24 eV for $FASnI_3$ to 3.55 eV for $FASnCl_3$ [32]. This is a very important property to optimize the harvesting of the solar spectrum in tandem solar cells. To date, the most studied organic-inorganic lead halide perovskites for PVK solar cells (PSC) are $MAPbI_3$ whose chemical structure is shown in Fig. 2.15 [33], and $FAPbI_3$; a mixture of them is also available with mixed cations in the A site and/or mixed anions in the X site [34].

For high efficiency perovskite solar cell, several challenges must be solved in terms of structure device engineering and excellent fabrication process. Differently from Silicon solar cells, where carrier collection is fostered by exploiting a *p-n* junction, charge collection and extraction in perovskite solar cells is helped by electron and hole selective contacts as shown in Fig. 2.16. In this regard, a PVK cell consists of a perovskite absorber material sandwiched between an electron transport layer (ETL) and a hole transport layer (HTL). The greater ETL/PVK and HTL/PVK quality

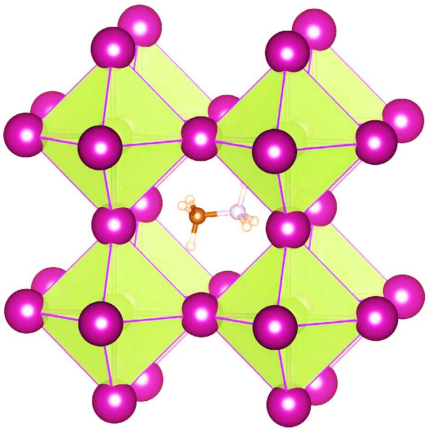

Fig. 2.15 Example of MAPI ($CH_3NH_3PbI_3$) structure: Methylammonium cation ($CH_3NH_3^+$) occupies the central A site surrounded by 12 nearest-neighbor iodide ions in corner-sharing PbI_6 octahedra [34].

interface is, the higher the PVK performance is [33]. Thus, efficient and controlled deposition methods are required. PVK cells can be classified as standard *n–i–p* or inverted *p–i–n* configurations depending on the position of the charge-selective layer. In this regard, several approaches can be used to fabricate a PVK solar cell. Appendix A presents a brief discussion about several deposition methods with a focus on the two-step hybrid deposition process (i.e. evaporation of PbI_2 mixed with spin coating of CH_3NH_3I (MAI) precursor), that I worked on during my research visit at Tor Vergata University.

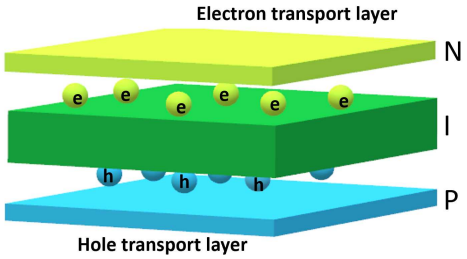

Fig. 2.16 Scketch of a *p-i-n* PVK structure.

Inorganic Electron Transport Layer Titanium dioxide (TiO_2) has been mostly used as ETL in perovskite solar cell. However, cells with TiO_2 have shown several issues, such as UV-induced photocatalytic activity that causes degradation and *JV* hysteresis [33]. SnO_2 is an alternative to TiO_2; it exhibits good conduction band alignment with perovskites, high electron mobility, high optical properties and good stability.

Another selective contact is the organic Fullerene C_{60} and its derivatives, such as PCBM, mostly exploited for *p-i-n* type PVK cell thanks to their appropriate electrical properties [33].
Regarding the HTL layer, the first material used as hole transport layer is the organic Spiro-OMeTAD material. It is characterized by a low conductivity (10^{-5} mS/cm) and low hole mobility (10^{-5} - 10^{-4} cm^2/Vs), requiring the use of several additives that cause significant instability [33]. Another widely used polymeric HTL is the PTAA that shows higher intrinsic hole mobility (10^{-3} - 10^{-2} cm^2/Vs) and enhanced stability. Interestingly, PTAA HTLs have been applied to both *n-i-p* and *p-i-n* type devices resulting in high conversion efficiencies. There are also inorganic HTLs able to overcome instability issues such as Copper thiocyanate (CuSCN) or Copper oxide (CuOx). More details can be found in [33]. In general, the excellent properties of the PVK cell and the improvement in fabrication processes kicked a boost of power conversion efficiency in few years. In 2012, a pure $MAPbI_3$ based cell had an efficiency of 9.7% and in 2022 the record efficiency of 25.7% was reported [28] by using a perovskite layer with mixed cation and mixed anion composition.

2.2.3 Perovskite/Silicon tandem solar cell

The more straightforward way to overcome the Shockley-Queisser limit of a SJ solar cell (Fig. 2.4) is to exploit a tandem configuration in which two or more subcells with different band gaps are stacked one on each other from the bottom (low-bandgap absorber) to the top (wide-bandgap absorber). Under illumination, high-energy photons are absorbed in the top sub-cell, and low-energy photons transmitted through the top cell are absorbed in the bottom one. Multi-junction (MJ) solar cells based on III-V semiconductors are most exploited in space. Instead, for terrestrial applications, their commercialization is more challenging. In this regard, among tandem technologies, PVS tandem solar cells are among the most promising candidates for next generation photovoltaics [29], combining lower fabrication costs (MSP of 0.31 $/W) and high efficiency of the PVK cells. In PVS tandem, a PVK sub-cell (tunable bandgap between 1.24 eV up to 3.55 eV) is placed on top of a Si (1.12 eV) sub-cell.
The most studied PVS tandem exploits 2-Terminal (2T) or 4-Terminal (4T) configuration [35, 36]. In 2T tandems (Fig. 2.17a), two sub-cells are monolithically fabricated on top of each other and connected in series through an interconnection layer realized by a poly- or amorphous- Silicon tunnel junction or by a recombination layer usually

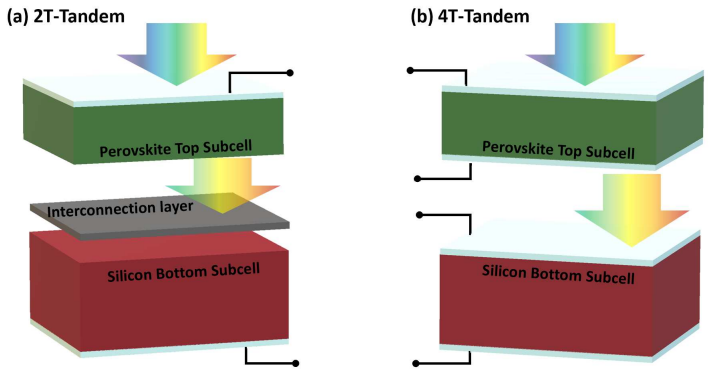

Fig. 2.17 Scheme of PVK/Si tandem solar cells with 2-Terminal (a) and 4-Terminal (b) [14].

made by a transparent conducting oxide (TCO). The series connection of the 2T configuration imposes a current matching constraint on the tandem cells, i.e. the current delivered to the external load is limited by the lowest photocurrent generated from the top and bottom subcells. Therefore, a good design of the tandem PVS cell, in terms of optical properties (band-gap matching, trasmittance of the layers, as well as light scattering [33]), is required to generate the same photo-current with the PVK and Silicon sub-cells. The current matching constraint between the subcells limits, in outdoor operation, the annual efficiency yield due to the high sensitivity to sun spectral variations [37]. Another issue of the 2T tandem is linked to the optical losses induced by the interconnection layer (tunnel junction or recombination layer in Fig. 2.17a), lowering the achievable efficiency [38].

In the 4T configuration, shown in Fig. 2.17b, two separate cells are fabricated individually and then mechanically stacked. The electrical power is extracted independently at each subcell by removing the current matching constraint required by the 2T design at the price of higher optical losses, because additional transparent layers are needed. Despite the advantages of the 4T tandem in terms of higher efficiency yield, the 2T device is more appealing for terrestrial application beacause of its lower fabrication costs.

Besides 2- and 4-terminal approaches, an alternative, less explored, solution is provided by the 3T design that aims at combining the advantages of 2T and 4T tandems. The classical 3T architecture retains the monolithic structure of the 2T one (Fig. 2.17a), by replacing the tunnel junction with a recombination layer or more commonly with a TCO layer where the third metal contact is placed [39]. This allows for the independent operation of the two sub-cells and removes the current mismatch constraint of 2T devices [15, 41–43]. The slightly higher fabrication cost might

be compensated by the looser requirements on bandgap and by the higher energy yield in real-word operation, owing to higher resilience to spectral and temperature variations [15, 44–47]. In this regard, it has been recently reported an experimental proof-of-concept 3T PVK/Si cell based on interdigitated back contact Silicon [48] (see Fig. 2.18a) with efficiency of 17.1% and a potential to reach about 27%.

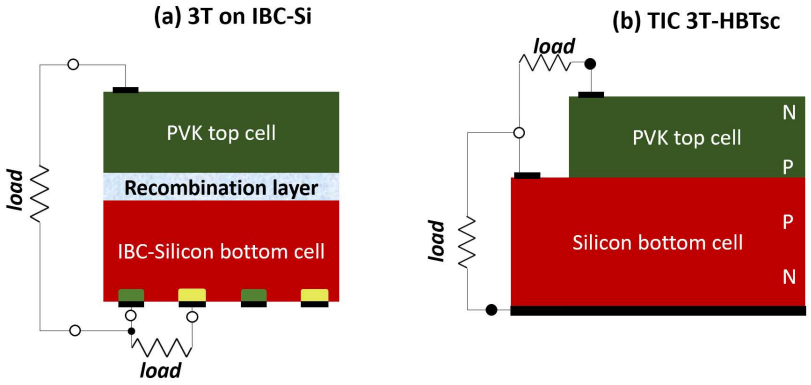

Fig. 2.18 Sketch of the 3T on IBC-Si (a) and TIC 3T-HBT (b) solar cell.

The IBC cell is an ideal candidate for 3T tandems, but its relatively high manufacturing costs are expected to limit their adoption to niche markets. In this direction, an attractive solution for developing three-terminal perovskite/silicon tandem solar cells, compatible with dominant Silicon photovoltaic technologies, is provided by the 3T Heterojunction Bipolar Transistor (3T-HBT) solar cell concept (Fig. 2.18b) [16, 43], that is introduced in the next chapter.

Chapter 3

Perovskite/Silicon 3T heterojunction bipolar transistor architecture

The theoretical limiting efficiency of silicon-based tandems is about 42%, according to Shockley-Queisser limit [21]. However, several loss mechanisms, i.e. radiative/non radiative recombination as well as optical losses, occur in the PVS tandem by worsening the ideal efficiency. Today, the efficiency record of 33.7% has been achieved for a 2T PVS [28] and 17.1% for a 3T-IBC tandem [48]. On the other hand, there are no experimental reports of PVS tandems based on the 3T heterojunction bipolar transistor (3T-HBT) architecture.
This chapter introduces the *npn* (*pnp*) bipolar transistor as photovoltaic device, and discusses the operating principle of the HBT device by introducing a generalized formulation of the analytical Hovel model [18], that will help to grasp the main features of the HBT-based solar cell. Then, based on the Hovel model, preliminary simulations will be presented for a proof-of-concept example of PVS 3T-HBT device. This chapter provides the preliminary knowledge needed to get insight from more advanced numerical models exploited to simulate both planar and textured 3T PVS HBT tandems in the next chapters.

3.1 Efficiency limit of 3T-HBT Silicon based tandem

The bipolar transistor device is based on two *pn* junctions that share the inner region, leading to the *npn* (*pnp*) structure of Figure 3.1a: from the top, *n*-Emitter, *p*-Base

and *n*-Collector. In Figure 3.1a, the three contacts of emitter, base and collector regions are indicated as E, B, C, respectively. It is possible to detect two sub-cells, Emitter/Base (EB) and Base/Collector (BC), that are electrically connected through the common base layer. From a circuital point of view, the EB and BC junctions can be represented as two *back-to-back* diodes. Once illuminated, the current photo-generated in each junction is delivered at two independent loads, connected across the E-B and B-C terminals. As will be demonstrated by the study reported in this thesis, the 3T-HBT device allows the optimal operation of both subcells, that can operate independently at their maximum power point.

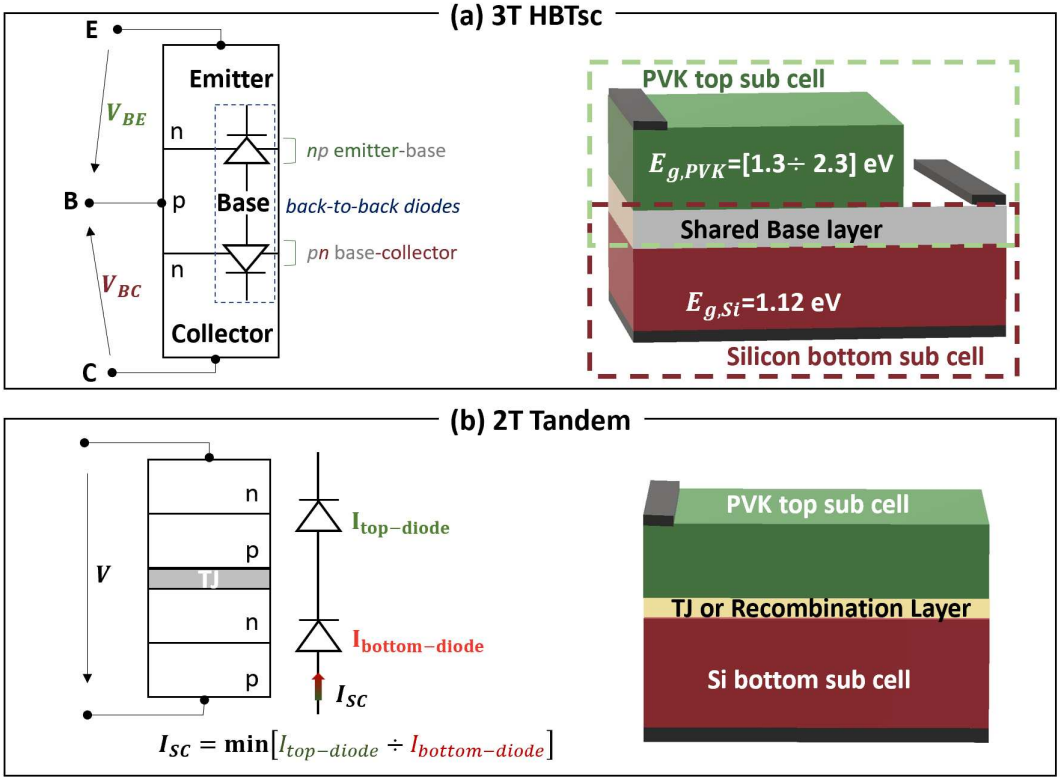

Fig. 3.1 Comparison between a *npn* PVS 3T-HBTsc (a) and a 2T PVS tandem (b).

In particular, the 3T-HBT structure removes the current matching constraint that affects conventional 2T tandem exploiting a series connection, as shown in Fig. 3.1b. In fact, in the 2T tandem the total current delivered to the external load is the minimum between the current generated by the top sub-cell ($I_{top\text{-}diode}$) and the bottom sub-cell ($I_{bottom\text{-}diode}$). This constraint has a significant effect on the choice of the band gap (Fig. 2.14) of the perovskite absorber in silicon-based tandems.

Aiming at identifying the optimum PVK bandgap range, we adopt the detailed balance limit [21] extended to deal with the 2T and 3T tandem [16]. The mathematical model is summarized in Appendix B. As a result, Fig. 3.2 shows the efficiency limit of 2T and 3T silicon based tandems as a function of the perovskite top cell's band gap in the range of [1.3 ÷ 2.3] eV. The band gap of the bottom sub-cell is equal to

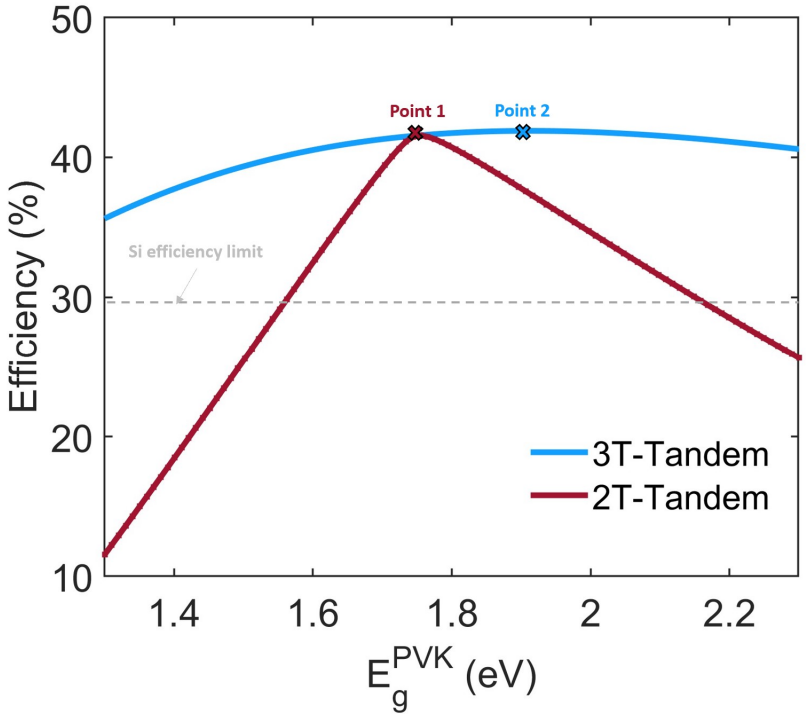

Fig. 3.2 Efficiency limit for 2T (red line) and 3T (blue line) silicon (1.12 eV) based tandem as a function of perovskite top cell's band gap [16]. Both simulated curves are obtained for a black body spectrum at $T_{sun} = 5762$ K, solar cell working temperature $T_c = 300$ K and for light concentration equal to 1. Details of the model in Appendix B. The grey dashed line indicates the theoretical efficiency limit for silicon solar cells.

1.12 eV (Si material). In this case study, we obtain a peak efficiency of 41.5% for the series-connected stack at 1.76 eV (Point 1 in Fig. 3.2) and of 42% for the 3T-tandem at 1.9 eV (Point 2 in Fig. 3.2). For high efficiency, the current matching constraint of the 2T tandem limits the choice of the band gap for the perovskite top sub cell to a narrow range around the efficiency peak (Point 1 in Fig. 3.2). Indeed, the 2T tandem overcomes the Si Shockley-Queisser limit of 29% (grey dashed line in Fig. 3.2) in the range [1.54 ÷ 2.2] eV. Instead, the 3T-HBT device relaxes the current-matching constraint of the 2T cell, allowing for a wide range of band gap combinations (blue curve in Fig. 3.2) [49–51].

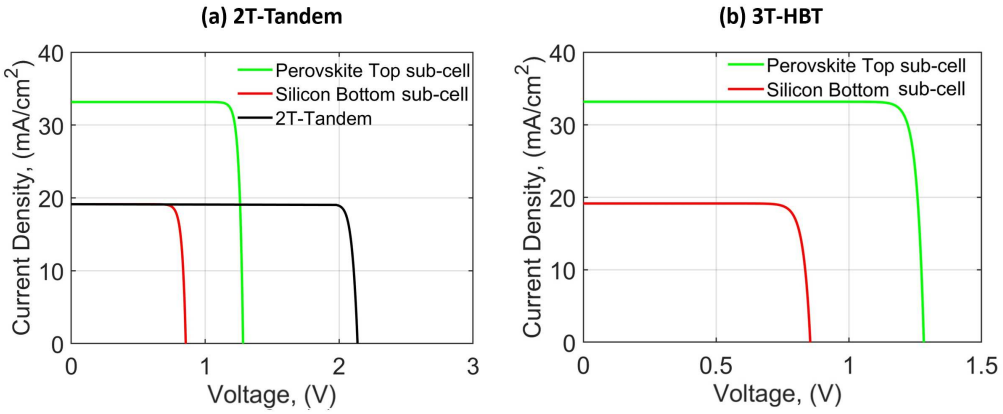

Fig. 3.3 J-V characteristics of the 2T tandem solar cell ($\eta_{2T} = 29\%$) (a). J-V characteristics of the 3T-HBT solar cell ($\eta_{3T} = 40\%$) (b). Simulations are carried out through the exdended Shlockley-Queisser model for both tandem configurations by fixing the energy gap of the perovskite to 1.55 eV (resembling that one of the $MAPbI_3$) for the top sub-cell and 1.12 eV for the silicon bottom sub-cells.

The theoretical efficiency limit for a tandem stack with 1.55 eV ($MAPbI_3$) and 1.12eV (Si) is close to 29% and 40% respectively for the 2T- and 3T-tandem (Fig. 3.2).

Fig. 3.3 shows the J-V characteristics for both tandem configurations. In Fig. 3.3a, it is possible to detect the effect of the current constraint on the 2T architecture. We highlight that the high current density of the perovskite solar cell is overestimated with respect to that one of practical devices, since we are neglecting TCO/HTL/ETL optical parasitic effects, i.e. parasitic absorption as well as reflectance, that reduce the perovskite photocurrent. In the 2T-tandem of Fig. 3.1b, the effect of the parasitic absorption will be hidden by the fact that, in this sub-optimal configuration, the current is limited by the bottom sub cell. Instead, in the 3T-tandem of Fig. 3.1a, where the two sub-cells work as they were independent, a reduction of the PVK current density would significantly worsen the power conversion efficiency to that one of the 2T-tandem eliminating, in fact, the advantage of the independent current extraction. In this regard, the SQ model shows its limitations and it is necessary carrying out opto-electronic simulations to deeply investigate the 3T-HBT device. As next step, we will study the 3T-HBT device with the aid of the extended analytical Hovel model.

3.2 Generalized Hovel model

The Hovel model [18], originally derived for *pn* junction cells, is able to describe the current flow of the minority charges under illumination into a SJ solar cell. In this section, it is extended to the case of two interacting *pn* junctions sharing the inner region, thus studying a structure akin to a *n-p-n* hetero-structure bipolar transistor. Let's consider the 1D model of Figure 3.4, where the x axis has the origin at the leftmost side of the emitter region (n-type, length w_{E}). The inner base region (p-type, length w_{B}) extends between $x = w_{\mathrm{E}}$ and $x = w_{\mathrm{E}} + w_{\mathrm{B}}$, and finally the collector region (n-type, length w_{C}) is defined between $x = w_{\mathrm{E}} + w_{\mathrm{B}}$ and $x = w_{\mathrm{E}} + w_{\mathrm{B}} + w_{\mathrm{C}}$. Light impinges from the emitter side.

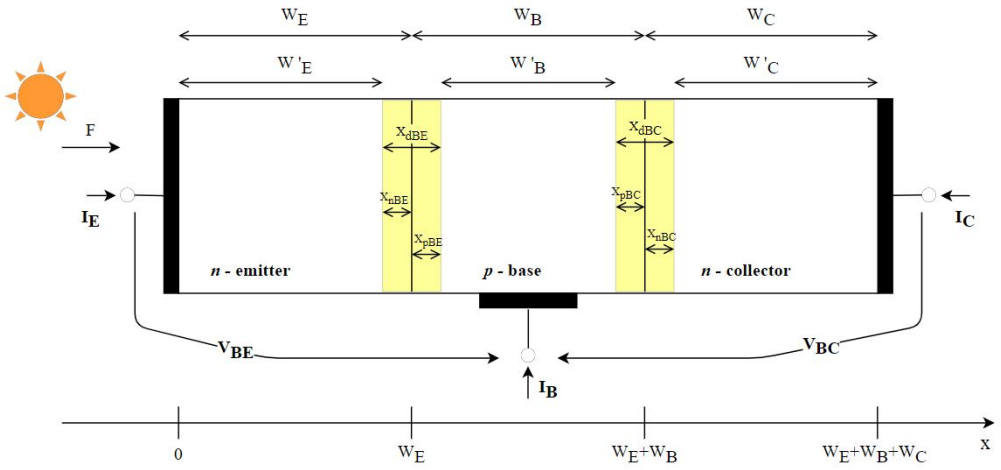

Fig. 3.4 3T-HBT structure considered in the model derivation. Yellow rectangles between the emitter-base and base-collector regions indicate the depleted regions.

Three ohmic contacts, one for each region can be found; in this model, all contacts are considered optically transparent. As the layers are uniformly doped, we assume negligible electric field in the quasi-neutral regions; hence, the electron and hole current density in the base J_{nB} and emitter (collector) J_{pE} (J_{pC}) are made of the diffusion component only and are given by:

$$J_{\mathrm{nB}}(x) = qD_{\mathrm{nB}}\frac{dn_{\mathrm{p}}}{dx} \tag{3.1}$$

$$J_{\mathrm{pE}}(x) = -qD_{\mathrm{pE}}\frac{dp_{\mathrm{nE}}}{dx} \tag{3.2}$$

$$J_{\mathrm{pC}}(x) = -qD_{\mathrm{pC}}\frac{dp_{\mathrm{nC}}}{dx} \tag{3.3}$$

where n_{p} and $p_{\mathrm{nE(C)}}$ are the electron and hole minority carrier in the base and emitter (collector) layers, respectively; D_{nB} and $D_{\mathrm{pE(C)}}$ are the *diffusion coefficients* of electrons and holes in the base and emitter (collector); q is the electrical charge. To obtain the current flow in each layer, we shall consider the continuity equation for minority carriers under *low-injection* condition and *quasi-neutrality* approximation. The following aspects were taken into account:

- different materials are accounted for in the three regions, thus considering a hetero-structure device
- the emitter and collector boundaries (at $x = 0$ and $x = w_{\mathrm{E}} + w_{\mathrm{B}} + w_{\mathrm{C}}$) are characterized by a finite surface recombination velocity S for the minority carriers
- optical generation is considered in the entire structure, including the depleted regions
- recombination rates are modeled according to the lifetime approximation.

In the p-doped quasi-neutral base region, we get:

$$\frac{1}{q}\left(\frac{dJ_{\mathrm{nB}}}{dx}\right) + G_{\mathrm{n}} - \frac{n_{\mathrm{p}} - n_{\mathrm{p0}}}{\tau_{\mathrm{n}}} = 0 \tag{3.4}$$

where G is the photogeneration term and τ_{n} is the electron lifetime. By substituting Eq. 3.1 in Eq. 3.4, the diffusion equation for electrons, n_{p}, reads as

$$\frac{d^2(n_{\mathrm{p}} - n_{\mathrm{p0}})}{dx^2} = \frac{n_{\mathrm{p}} - n_{\mathrm{p0}}}{D_{\mathrm{nB}}\ \tau_{\mathrm{nB}}} - \frac{\phi\, \mathrm{e}^{-\alpha_{\mathrm{B}}(x - w_{\mathrm{E}})}}{D_{\mathrm{nB}}} \tag{3.5}$$

where $\phi = \phi_0(1 - R_{\mathrm{E}})(1 - R_{\mathrm{B}})\alpha_{\mathrm{B}}\, \mathrm{e}^{-\alpha_{\mathrm{E}} w_{\mathrm{E}}}$. $R_{\mathrm{E(B)}}$ is the reflectance, calculated based on Eq. 2.11, at the emitter-air (base-emitter) interface, $\alpha_{\mathrm{E(B)}}$ and $w_{\mathrm{E(B)}}$ are the optical absorption and thickness of the emitter (base) layer, respectively, n_{p0} is the electron density under thermodynamic equilibrium, D_{nB} is the diffusion coefficient of electrons in the base, τ_{nB} is the electron lifetime in the base, and ϕ_0 is the incident photon flux. Eq. 3.5 has the form of a *second order non homogeneous differential*

equation that can be solved under two boundary conditions identified by the junction law:

$$n_{\mathrm{p}}(x^*) - n_{\mathrm{p0}} = n_{\mathrm{p0}} \left(\mathrm{e}^{V^*/V_{\mathrm{T}}} - 1 \right) \tag{3.6}$$

with $V^* = V_{\mathrm{EB}}$ for $x^* = w_{\mathrm{E}} + x_{p\mathrm{BE}}$, and $V^* = V_{\mathrm{CB}}$ for $x^* = w_{\mathrm{E}} + w_{\mathrm{B}} - x_{p\mathrm{BC}}$. $x_{p\mathrm{BE}}$, $x_{p\mathrm{BC}}$ are the thickness of the depleted base region at the E/B and C/B junctions respectively. By solving the continuity equation Eq. 3.5, the electron distribution in the p-type base layer results as:

$$\begin{aligned}
n_{\mathrm{p}} - n_{\mathrm{p0}} = {} & n_{\mathrm{p0}} \left[\mathrm{e}^{V_{\mathrm{BE}}/V_{\mathrm{T}}} - 1 \right] \left[\frac{\sinh\left[\dfrac{w_{\mathrm{E}} + x_{p\mathrm{BE}} + w'_{\mathrm{B}} - x}{L_{n\mathrm{B}}} \right]}{\sinh\left[\dfrac{w'_{\mathrm{B}}}{L_{n\mathrm{B}}} \right]} \right] \\
& - n_{\mathrm{p0}} \left[\mathrm{e}^{V_{\mathrm{BC}}/V_{\mathrm{T}}} - 1 \right] \left[\frac{\sinh\left[\dfrac{w_{\mathrm{E}} + x_{p\mathrm{BE}} - x}{L_{n\mathrm{B}}} \right]}{\sinh\left[\dfrac{w'_{\mathrm{B}}}{L_{n\mathrm{B}}} \right]} \right] \\
& + k_{n\mathrm{B}} \frac{\sinh\left[\dfrac{w_{\mathrm{E}} + x_{p\mathrm{BE}} - x}{L_{n\mathrm{B}}} \right]}{\sinh\left[\dfrac{w'_{\mathrm{B}}}{L_{n\mathrm{B}}} \right]} \mathrm{e}^{-\alpha_{\mathrm{B}}(x_{p\mathrm{BE}} + w'_{\mathrm{B}})} \\
& - k_{n\mathrm{B}} \frac{\sinh\left[\dfrac{w_{\mathrm{E}} + x_{p\mathrm{BE}} + w'_{\mathrm{B}} - x}{L_{n\mathrm{B}}} \right]}{\sinh\left[\dfrac{w'_{\mathrm{B}}}{L_{n\mathrm{B}}} \right]} \mathrm{e}^{-\alpha_{\mathrm{B}} x_{p\mathrm{BE}}} + k_{n\mathrm{B}}\, \mathrm{e}^{-\alpha_{\mathrm{B}}(x - w_{\mathrm{E}})}
\end{aligned} \tag{3.7}$$

Replacing the expression of the electron density (Eq. 3.7) in Eq. 3.1, we obtain the current J_{nB} along the base whose dark component depends on both the EB and BC self-bias voltages, so that the two sub-cells are not completely independent each other. To obtain the emitter (collector) current J_{pE} (J_{pC}) in the neutral region, Eq. 3.5 can be re-formulated for the hole minority carriers (p_{n}). In this case, the continuity equation will be solved under two boundary conditions identified by the surface recombination phenomena at the emitter (collector) surface and by the junction law at the boundary of the depletion region of the emitter-base (base-collector) junction. The full equations for the emitter, base and collector currents, J_{pE}, J_{nB} and J_{pC}, can be found in Appendix C.

Up to this point, we have considered only photons absorbed in the neutral regions,

however it is necessary to consider also the photo-generation of carriers into the EB and BC depleted regions. In these, the electric field is high enough that photogenerated e-h pairs are generally swept out towards their contacts and extracted before they can recombine [18]. Hence, the number of collected electron-hole pairs is assumed to be equal to the number of photons absorbed. Appendix C reports the expression for the photogenerated current in the EB (BC) depleted region $J_{\mathrm{EB}}^{\mathrm{dr}}$ ($J_{\mathrm{BC}}^{\mathrm{dr}}$), assuming unitary collection efficiency. Thus, the total current extracted at the emitter and collector contacts (Figure 3.4) results as

$$I_{\mathrm{E}} = J_{\mathrm{pE}}\big|_{W_{\mathrm{E}}'} + J_{\mathrm{nB}}\big|_{W_{\mathrm{E}}+x_{\mathrm{pBE}}} + J_{\mathrm{EB}}^{\mathrm{dr}} \tag{3.8a}$$

$$I_{\mathrm{C}} = J_{\mathrm{nB}}\big|_{W_{\mathrm{E}}+x_{\mathrm{pBE}}+W_{\mathrm{B}}'} + J_{\mathrm{pC}}\big|_{W_{\mathrm{E}}+W_{\mathrm{B}}+x_{\mathrm{nBC}}} + J_{\mathrm{BC}}^{\mathrm{dr}} \tag{3.8b}$$

where J_{pE}, J_{nB} and J_{pC} are calculated at the proper junction edge. Once obtained the expression for all current contributions, we get, through a few algebraic manipulations, a general expression for the emitter and collector currents that reads as

$$I_{\mathrm{E}} = a_{11}\left[\mathrm{e}^{V_{\mathrm{BE}}/V_{\mathrm{T}}}-1\right] + a_{12}\left[\mathrm{e}^{V_{\mathrm{BC}}/V_{\mathrm{T}}}-1\right] + I_{\mathrm{phE}} \tag{3.9a}$$

$$I_{\mathrm{C}} = a_{21}\left[\mathrm{e}^{V_{\mathrm{BE}}/V_{\mathrm{T}}}-1\right] + a_{22}\left[\mathrm{e}^{V_{\mathrm{BC}}/V_{\mathrm{T}}}-1\right] + I_{\mathrm{phC}} \tag{3.9b}$$

Eq. 3.9 provides a set of equations under illumination where both emitter and collector current (I_{E}, I_{C}) are expressed as a function of the EB and BC voltages. The formulation extends the so-called Ebers-Moll model of bipolar transistors [19] to the operation under illumination. In Eq. 3.9, I_{ph} represents the photo-current contribution to the corresponding terminal current and the four $a_{\mathrm{i,j}}$ parameters (dimensionally currents) are:

$$a_{11} = -qA\frac{D_{p\mathrm{E}}}{L_{p\mathrm{E}}}\frac{n_{\mathrm{iE}}^2}{N_{D\mathrm{E}}}\chi_{\mathrm{E}} - qA\frac{D_{n\mathrm{B}}}{L_{n\mathrm{B}}}\frac{n_{\mathrm{iB}}^2}{N_{A\mathrm{B}}}\coth\left[\frac{w_{\mathrm{B}}'}{L_{n\mathrm{B}}}\right] \tag{3.10a}$$

$$a_{22} = -qA\frac{D_{p\mathrm{C}}}{L_{p\mathrm{C}}}\frac{n_{\mathrm{iC}}^2}{N_{D\mathrm{C}}}\chi_{\mathrm{C}} - qA\frac{D_{n\mathrm{B}}}{L_{n\mathrm{B}}}\frac{n_{\mathrm{iB}}^2}{N_{A\mathrm{B}}}\coth\left[\frac{w_{\mathrm{B}}'}{L_{n\mathrm{B}}}\right] \tag{3.10b}$$

$$a_{12} = a_{21} = qA\frac{D_{n\mathrm{B}}}{L_{n\mathrm{B}}}\frac{n_{\mathrm{iB}}^2}{N_{A\mathrm{B}}}\frac{1}{\sinh\left[\frac{w_{\mathrm{B}}'}{L_{n\mathrm{B}}}\right]} \tag{3.10c}$$

where A is the device cross section area, D and L are the minority carrier diffusivity and diffusion length, n_i is the intrinsic concentration, and

$$\chi_\beta = \frac{N_\beta}{D_\beta} \qquad \beta = \mathrm{E,C} \tag{3.11a}$$

$$N_\beta = \sinh\left[\frac{w'_\beta}{L_{p\beta}}\right] + \frac{S_{p\beta}L_{p\beta}}{D_{p\beta}}\cosh\left[\frac{w'_\beta}{L_{p\beta}}\right] \tag{3.11b}$$

$$D_\beta = \cosh\left[\frac{w'_\beta}{L_{p\beta}}\right] + \frac{S_{p\beta}L_{p\beta}}{D_{p\beta}}\sinh\left[\frac{w'_\beta}{L_{p\beta}}\right] \tag{3.11c}$$

The primed lengths w'_β refer to the physical size of the neutral portion of side β, i.e. the total length w_β minus the amplitude of the depleted portion of the same side. The amplitude of the depleted regions can be evaluated according to the following expressions ($\beta = \mathrm{E,C}$)

$$x_{\mathrm{dB}\beta} = \sqrt{2\frac{(\varepsilon_\mathrm{B}N_\mathrm{AB})||(\varepsilon_\beta N_{\mathrm{D}\beta})}{qN^2_{\mathrm{eq,A}\beta}}\left(V_{\mathrm{bi,B}\beta} - V_{\mathrm{B}\beta}\right)} \tag{3.12a}$$

$$x_{n\mathrm{B}\beta} = x_{\mathrm{dB}\beta}\frac{N_{\mathrm{D}\beta}}{N_\mathrm{AB}+N_{\mathrm{D}\beta}} \quad x_{p\mathrm{B}\beta} = x_{\mathrm{dB}\beta}\frac{N_\mathrm{AB}}{N_\mathrm{AB}+N_{\mathrm{D}\beta}} \tag{3.12b}$$

where $V_{\mathrm{bi,B}\beta}$ is the built in voltage of the Bβ hetero-junction, $N_{\mathrm{eq,A}\beta} = N_\mathrm{AB}||N_{\mathrm{D}\beta}$ is the equivalent doping, and $a||b = ab/(a+b)$. Once defined the $a_{i,j}$ parameters of Eq. 3.9, let's write the photocurrents I_phE and I_phC terms. To this aim, once defined the absorption coefficient α_β for side $\beta =$ E, B, C and the following constants

$$k_{p\mathrm{E}} = \phi_0(1-R_\mathrm{E})\frac{\alpha_\mathrm{E}\tau_{p\mathrm{E}}}{1-\alpha^2_\mathrm{E}L^2_{p\mathrm{E}}} \tag{3.13a}$$

$$k_{n\mathrm{B}} = \phi_0(1-R_\mathrm{E})\,\mathrm{e}^{-\alpha_\mathrm{E}w_\mathrm{E}}(1-R_\mathrm{B})\frac{\alpha_\mathrm{B}\tau_{n\mathrm{B}}}{1-\alpha^2_\mathrm{B}L^2_{p\mathrm{B}}} \tag{3.13b}$$

$$k_{p\mathrm{C}} = \phi_0(1-R_\mathrm{E})\,\mathrm{e}^{-\alpha_\mathrm{E}w_\mathrm{E}}(1-R_\mathrm{B})\,\mathrm{e}^{-\alpha_\mathrm{B}w_\mathrm{B}}(1-R_\mathrm{C})\frac{\alpha_\mathrm{C}\tau_{p\mathrm{C}}}{1-\alpha^2_\mathrm{C}L^2_{p\mathrm{C}}} \tag{3.13c}$$

where ϕ_0 is the impinging photon flux, R the reflection coefficients, calculated based on Eq. 2.11, and τ the minority carrier lifetime. At short circuit, the emitter and

collector photocurrents I_{phE} and I_{phC} read as

$$\frac{I_{\mathrm{phE}}}{qA} = \frac{D_{p\mathrm{E}}}{L_{p\mathrm{E}}} k_{p\mathrm{E}} \left[\mathrm{e}^{-\alpha_{\mathrm{E}} w'_{\mathrm{E}}} G_{\mathrm{E}} - \frac{\alpha_{\mathrm{E}} L_{p\mathrm{E}} + \dfrac{S_{p\mathrm{E}} L_{p\mathrm{E}}}{D_{p\mathrm{E}}}}{D_{\mathrm{E}}} \right] + D_{p\mathrm{E}} \alpha_{\mathrm{E}} k_{p\mathrm{E}} \mathrm{e}^{-\alpha_{\mathrm{E}} w'_{\mathrm{E}}} +$$

$$- D_{n\mathrm{B}} \alpha_{\mathrm{B}} k_{n\mathrm{B}} \mathrm{e}^{-\alpha_{\mathrm{B}} x_{p\mathrm{BE}}} + \frac{D_{n\mathrm{B}}}{L_{n\mathrm{B}}} k_{n\mathrm{B}} \mathrm{e}^{-\alpha_{\mathrm{B}} x_{p\mathrm{BE}}} \frac{\cosh\left[\dfrac{w'_{\mathrm{B}}}{L_{n\mathrm{B}}}\right] - \mathrm{e}^{-\alpha_{\mathrm{B}} w'_{\mathrm{B}}}}{\sinh\left[\dfrac{w'_{\mathrm{B}}}{L_{n\mathrm{B}}}\right]} +$$

$$+ F(1-R_{\mathrm{E}}) \left\{ \mathrm{e}^{-\alpha_{\mathrm{E}} w'_{\mathrm{E}}} \left[1 - \mathrm{e}^{-\alpha_{\mathrm{E}} x_{n\mathrm{BE}}}\right] + (1-R_{\mathrm{B}}) \mathrm{e}^{-\alpha_{\mathrm{E}} w_{\mathrm{E}}} \left[1 - \mathrm{e}^{-\alpha_{\mathrm{B}} x_{p\mathrm{BE}}}\right] \right\} \tag{3.14a}$$

$$\frac{I_{\mathrm{phC}}}{qA} = \frac{D_{p\mathrm{C}}}{L_{p\mathrm{C}}} k_{p\mathrm{C}} \mathrm{e}^{-\alpha_{\mathrm{C}} x_{n\mathrm{BC}}} \times \left[-G_{\mathrm{C}} + \frac{\left(-\alpha_{\mathrm{C}} L_{p\mathrm{C}} + \dfrac{S_{p\mathrm{C}} L_{p\mathrm{C}}}{D_{p\mathrm{C}}} \right) \mathrm{e}^{-\alpha_{\mathrm{C}} w'_{\mathrm{C}}}}{D_{\mathrm{C}}} \right] +$$

$$+ D_{p\mathrm{C}} \alpha_{\mathrm{C}} k_{p\mathrm{C}} \mathrm{e}^{-\alpha_{\mathrm{C}} x_{n\mathrm{BC}}} - D_{n\mathrm{B}} \alpha_{\mathrm{B}} k_{n\mathrm{B}} \mathrm{e}^{-\alpha_{\mathrm{B}} (w_{\mathrm{B}} - x_{p\mathrm{BC}})} +$$

$$- \frac{D_{n\mathrm{B}}}{L_{n\mathrm{B}}} k_{n\mathrm{B}} \mathrm{e}^{-\alpha_{\mathrm{B}} x_{p\mathrm{BE}}} \frac{\mathrm{e}^{-\alpha_{\mathrm{B}} w'_{\mathrm{B}}} \cosh\left[\dfrac{w'_{\mathrm{B}}}{L_{n\mathrm{B}}}\right] - 1}{\sinh\left[\dfrac{w'_{\mathrm{B}}}{L_{n\mathrm{B}}}\right]} +$$

$$+ F(1-R_{\mathrm{E}})(1-R_{\mathrm{B}}) \mathrm{e}^{-\alpha_{\mathrm{E}} w_{\mathrm{E}}} \left\{ \mathrm{e}^{-\alpha_{\mathrm{B}} (w'_{\mathrm{B}} + x_{p\mathrm{BE}})} \right.$$

$$\left. \times \left[1 - \mathrm{e}^{\alpha_{\mathrm{B}} x_{p\mathrm{BC}}}\right] + (1-R_{\mathrm{C}}) \mathrm{e}^{-\alpha_{\mathrm{B}} w_{\mathrm{B}}} \left[1 - \mathrm{e}^{-\alpha_{\mathrm{C}} x_{n\mathrm{BC}}}\right] \right\} \tag{3.14b}$$

Finally, from Eq. 3.14, it is possible to compute the EQE of the 3T-HBT device as follows

$$EQE(\lambda) = \frac{J_{\mathrm{phE}}(\lambda)}{q\phi_0(\lambda)} + \frac{J_{\mathrm{phC}}(\lambda)}{q\phi_0(\lambda)} \tag{3.15}$$

where J_{phE} and J_{phC} are the emitter and collector photo-current density.
The Ebers-Moll equations (Eq. 3.9 to Eq. 3.14) provide a complete analytical

model to study the behavior of the 3T-HBT device. From these equations, it is straightforward to derive the equivalent circuit model shown in Figure 3.5. The 3T-HBTsc equivalent electrical model consists of the classical Ebers-Moll circuit of bipolar transistors, complemented with one current generator for each junction, thats model the photogeneration. In Figure 3.5, we can identify three components for each junction: the photogenerated current generator I_{phE} (I_{phC}) in parallel to the diode with reverse saturation current I_{E0} (I_{C0}) and to the current-controlled current source $\alpha_{\mathrm{R}} I_{\mathrm{R}}$ ($\alpha_{\mathrm{F}} I_{\mathrm{F}}$). The latter one accounts for the interplay of the two junctions through the common base layer.

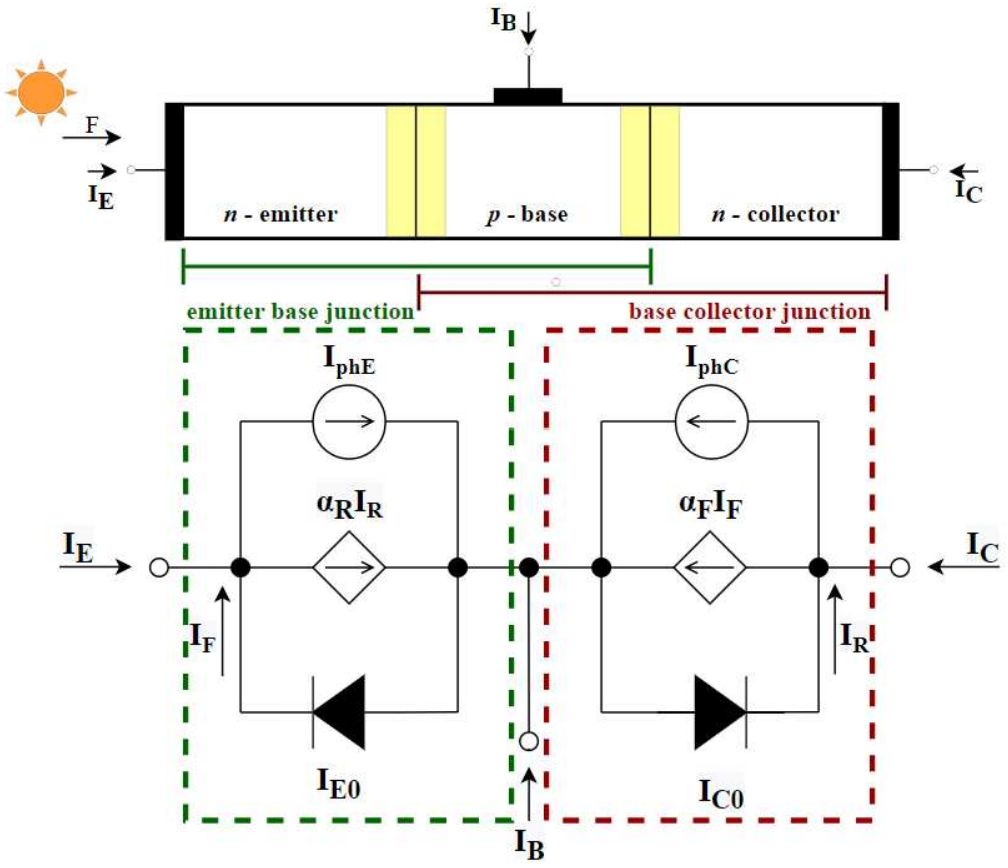

Fig. 3.5 Equivalent circuit representing the electrical behaviour of the interacting heterojunctions.

Let's find a link between the Ebers-Moll equations (Eq.3.9) and the equivalent electrical model of Figure 3.5. To this aim, we derive the expression $(\exp(V_{\mathrm{BC}}/V_{\mathrm{T}}) - 1)$ from Eq.3.9b and substitute it into Eq.3.9a (and analogously for $\exp(V_{\mathrm{BE}}/V_{\mathrm{T}}) - 1$).

Thus, the system of Eq.3.9 can be rewritten as

$$I_{\mathrm{E}} = -\alpha_{\mathrm{R}} I_{\mathrm{C}} - I_{\mathrm{ES}} \left[\mathrm{e}^{V_{\mathrm{BE}}/V_{\mathrm{T}}} - 1 \right] + I_{\mathrm{phE}} + \alpha_{\mathrm{R}} I_{\mathrm{phC}} \tag{3.16a}$$

$$I_{\mathrm{C}} = -\alpha_{\mathrm{F}} I_{\mathrm{E}} - I_{\mathrm{CS}} \left[\mathrm{e}^{V_{\mathrm{BC}}/V_{\mathrm{T}}} - 1 \right] + I_{\mathrm{phC}} + \alpha_{\mathrm{F}} I_{\mathrm{phE}} \tag{3.16b}$$

where we have defined the *common base current amplifications* in forward and reverse operation

$$\alpha_{\mathrm{F}} = -\frac{a_{21}}{a_{11}} \qquad \alpha_{\mathrm{R}} = -\frac{a_{12}}{a_{22}} \tag{3.17}$$

and the *reverse saturation currents*

$$I_{\mathrm{ES}} = \frac{a_{12}a_{21} - a_{11}a_{22}}{a_{22}} \qquad I_{\mathrm{CS}} = \frac{a_{12}a_{21} - a_{11}a_{22}}{a_{11}} \tag{3.18}$$

The reciprocity condition of Eq. 3.10, i.e. $a_{12} = a_{21}$, imposes that $\alpha_{\mathrm{F}} I_{\mathrm{ES}} = \alpha_{\mathrm{R}} I_{\mathrm{CS}}$. Again, by substituting Eq.3.16b into Eq.3.16a, and Eq.3.16a into Eq.3.16b, we get to

$$I_{\mathrm{E}} = \alpha_{\mathrm{R}} I_{\mathrm{R}} - I_{\mathrm{F}} + I_{\mathrm{phE}} \tag{3.19a}$$

$$I_{\mathrm{C}} = \alpha_{\mathrm{F}} I_{\mathrm{F}} - I_{\mathrm{R}} + I_{\mathrm{phC}} \tag{3.19b}$$

where

$$I_{\mathrm{F}} = I_{\mathrm{E0}} \left[\mathrm{e}^{V_{\mathrm{BE}}/V_T} - 1 \right] \qquad I_{\mathrm{E0}} = \frac{I_{\mathrm{ES}}}{1 - \alpha_{\mathrm{R}}\alpha_{\mathrm{F}}} \tag{3.20a}$$

$$I_{\mathrm{R}} = I_{\mathrm{C0}} \left[\mathrm{e}^{V_{\mathrm{BC}}/V_T} - 1 \right] \qquad I_{\mathrm{C0}} = \frac{I_{\mathrm{CS}}}{1 - \alpha_{\mathrm{R}}\alpha_{\mathrm{F}}} \tag{3.20b}$$

with the reciprocity condition $\alpha_{\mathrm{F}} I_{\mathrm{E0}} = \alpha_{\mathrm{R}} I_{\mathrm{C0}}$. The model of Eq.3.19 corresponds to the equivalent circuit shown in Figure 3.5 where the current-controlled current source $\alpha_{\mathrm{R}} I_{\mathrm{R}}$ ($\alpha_{\mathrm{F}} I_{\mathrm{F}}$) accounts for the effect of the BC voltage on the EB junction due to the injection of minority carriers from the collector to the emitter (and vice versa) through the common base layer. The coefficients α_{R}, α_{F} model this electrical coupling, the so-called *transistor effect*, whose strength depends on a few physical device parameters, such as doping levels, energy band discontinuities, minority carrier diffusion length, and layer thickness. As well known from bipolar transistor theory [19], the closer α_{R} (α_{F}) gets to 1, the stronger the transistor effect is. On the other hand, as firstly argued in [16], the power conversion efficiency of the HBT solar cell is maximized when the transistor effect is negligible. In fact, by design, the HBT

tandem shall exploit emitter and base layers with higher bandgap than the collector layer. Therefore, diffusion of minority carriers from the E/B junction towards the B/C one implies a flow of carriers in the direction of decreasing splitting of the quasi-Fermi levels, with a reduction of the electrical power produced by the solar cell. This is reflected, in the behavior of the equivalent electrical circuit in Fig. 3.5, by the fact that the $\alpha_F I_F$ ($\alpha_R I_R$) current adding up to the B/C (E/B) photocurrent is more than compensated by the increased dark current at the corresponding junction, yielding to a net reduction of the electrical power delivered to the load [52].
The analytical Ebers-Moll model provides a useful means to assess the possible efficiency penalty due to the subcells' interplay mediated by the transistor effect. To this aim it is useful to introduce two further figures of merit of bipolar transistors, recalling that under photovoltaic action both junctions develop a forward bias condition such that, given the Emitter/Base and Collector bandgap difference, at maximum power point $V_{BE} > V_{BC}$.

- The *emitter (collector) injection efficiency* $\gamma_{E(C)}$, which measures the effectiveness of minority carrier injection into the base from the emitter (collector), defined as

$$\gamma_{E(C)} = \frac{J_{nB}\big|_{W_E + x_{pBE}(+W'_B)}}{J_{nB}\big|_{W_E + x_{pBE}(+W'_B)} + J_{pE(C)}\big|_{W'_E(W_E + W_B + x_{nBC})}} \approx \frac{1}{1 + \dfrac{D_p n^2_{i,E(C)} N_{AB} \zeta_B}{D_n n^2_{i,B} N_{DE(C)} \zeta_{E(C)}}} \tag{3.21}$$

  where the approximated expression holds in the limit of short or long layers (with respect to the diffusion length), ζ being the physical length or the diffusion length of minority carriers of that layer.

- The *base transport factor* α_T, which measures the effectiveness of minority carrier transport through the base, defined as

$$\alpha_T = \frac{J_{nB}\big|_{W_E + x_{pBE} + W'_B}}{J_{nB}\big|_{W_E + x_{pBE}}} \tag{3.22}$$

  for a minority carriers flow directed from the emitter towards the collector, as it is the case when $V_{BE} > V_{BC}$.

It can be easily verified that $\alpha_F \approx \gamma_E \alpha_T$ and analogously for α_R. Thus, considering again the high/low gap structure, it is apparent that in the HBT tandem γ_C and α_R will be negligibly small and any possibile penalty will be caused by the minority carrier injection from the E/B junction towards the B/C one.
To make the discussion more quantitative, let us consider a representative structure built upon the two main design requirements for the HBT tandem: i) high/low gap design; ii) high base doping to ensure low resistive loss associated to the third (base) terminal and low emitter/collector doping to maximize carrier collection efficiency. Fig. 3.6 analyzes how the HBT figures of merit change as a function of the ratio between base thickness and diffusion length of minority electrons in the base.

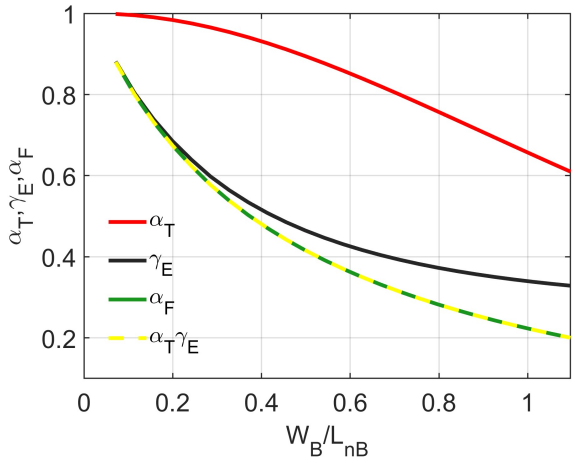

Fig. 3.6 Figures of merit of a representative HBT solar cell with emitter and base bandgap of $E_H = 1.55$ eV, collector bandgap of $E_L = 1.12$ eV, and B/E and B/C doping level ratio ≈ 100. The forward gain ratio α_F is calculated according to Eq. 3.17 and as product of γ_E and α_T. Calculated parameters are representative of any operating condition between short circuit and maximum power point.

The example considers a structure with E/B bandgap $E_H = 1.55$ eV, collector bandgap $E_L = 1.12$ eV, and $N_{AB}/N_{DE} \approx N_{AB}/N_{DC} \approx 100$. Calculations were done imposing unitary absorptivity in the emitter and collector sides, such as the change of base geometry does not affect the photogenerated currents. It is apparent that the aforementioned design rules make the emitter injection efficiency rather low, thus limiting the forward current gain α_F to ≈ 0.9 even in the case of short base and $\alpha_T \approx 1$. Corresponding to this, Fig. 3.7 shows the predicted reduction of efficiency as a function of α_F. The efficiency penalty as α_F grows (base width much shorter that the diffusion length) remains rather limited, lower than 2%, demonstrating that the

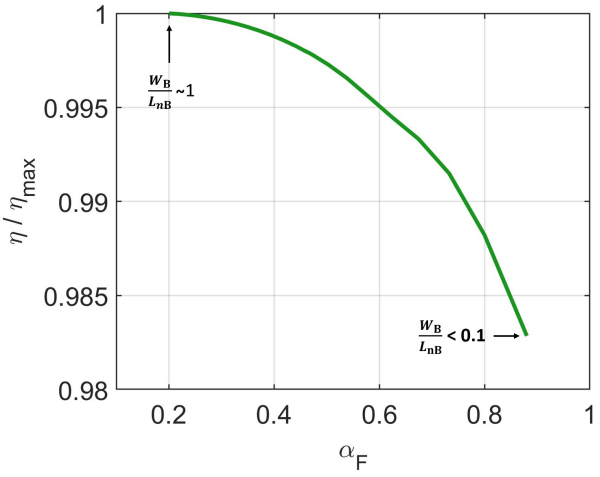

Fig. 3.7 Variation of the normalized HBT efficiency at maximum power point as a function of the forward current gain α_F.

HBT tandem structure ensures - *by design* - a high decoupling between the top and bottom subcells, approaching the theoretical efficiency limit of two independently connected junctions. There preliminary conclusions will be verified in the next part of the dissertation on the basis of more advanced physics-based models.

3.3 Modeling results

The generalized Hovel model has been used to carry out a preliminary simulation study of the PVS 3T-HBT tandem architecture [53]. For this case study, we consider a *pnp* HBTsc consisting of *p*-doped PVK ($CH_3NH_3PbI_3$) emitter, *n*-doped a-Si:H base and *p*-doped c-Si collector. The HTL layer is taken into account only from the optical point of view. The PVK/a-Si:H layers form the emitter-base sub-cell, and the a-Si:H/Si layers the base-collector one. For this case study, we have considered a doping of $\sim 10^{16}\,\mathrm{cm}^{-3}$ for the emitter [54] and collector layers. Table 3.1 summarizes a range of the material parameters used in the simulations for intrinsic carrier density [54, 55], energy gap [54, 55], radiative recombination coefficient (B_{rad}) [55–57], mobility [54, 57, 58]. Simulations neglect surface recombination and consider both radiative and non-radiative recombination [57, 59], according to the lifetime constants reported in Table 3.1. In particular, under low injection condition, the radiative lifetime has been calculated as $1/(B_{rad}N_{dop})$.

Table 3.1 Main parameters value. E_g: Bandgap n_i: Intrinsic concentration μ: Mobility χ: Electron affinity τ: Lifetime. (e/h): electron/hole.

	$CH_3NH_3PbI_3$	a-Si:H	c-Si
Thickness (nm)	350	600	2×10^5
E_g (eV)	1.55 ÷ 1.6	1.7	1.1
Doping (cm^{-3})	10^{16}	3×10^{18}	10^{16}
n_i (cm^{-3})	$8\times10^4 \div 3.8\times10^5$	9×10^4	9.6×10^9
μ (cm^2/Vs)	11.8[e]	5[h]	1177[e]
χ (eV)	3.73	3.9	4.05
B_{rad} (cm^3s^{-1})	$8\times10^{-10} \div 10^{-9}$	1.8×10^{-15}	1.1×10^{-14}
τ_{rad}	97 ÷ 125 ns	0.15 ms	9 ms
τ_{SRH}	736 ns	-	1 ms
τ_{tot}	85 ÷ 106 ns	150 ns	0.9 ms

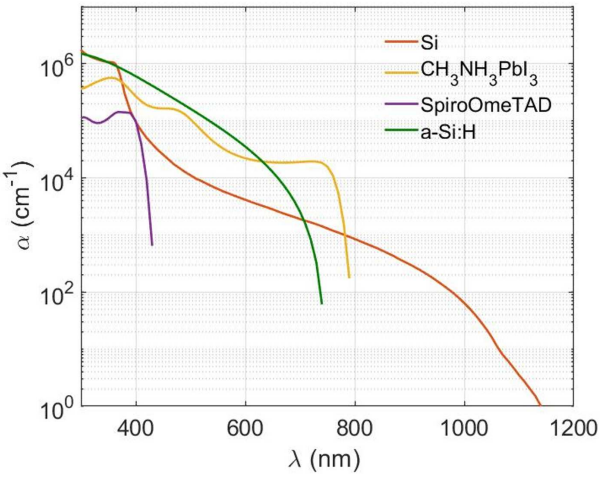

Fig. 3.8 Absorption coefficient α of the HTL (purple line), PVK (yellow line), a-Si:H (green line) and silicon (red line).

Figure 3.9 shows the total External Quantum Efficiency (EQE) and the partial contributions from emitter (E), base (B) and collector (C) for both quasi-neutral (qnr) and depleted regions (dr) obtained for a perovskite absorber layer with $E_g = 1.6$ eV. The device is simulated without anti-reflection layer, hence the EQE shows a significant penalty due to the air-HTL reflectance. Most photons, absorbed in the emitter layer, generate e-h pairs close to the surface since the direct bandgap of the PVK material has strong absorption at short wavelengths (Figure 3.8). Although the base layer has energy gap higher than that one of the emitter, it absorbs part of the

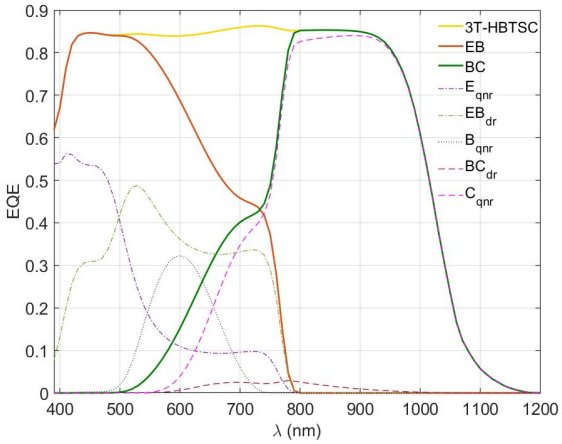

Fig. 3.9 External quantum efficiency of the 3T-HBTSC (yellow line) and of the sub-cells components (dashed lines), including quasi neutral regions (qnr) and depleted regions (dr). Reproduced from [53].

solar spectrum contributing to the total amount of photo-generated current. Indeed, the emitter is thin ($W_E \sim 350$ nm) and a certain fraction of photons are not absorbed and escape towards the base and collector layers.
Figure 3.10 [53] shows the EB and BC current voltage characteristics.

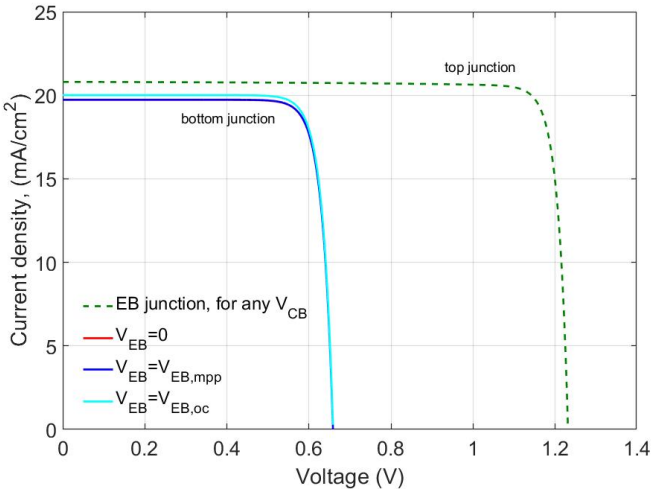

Fig. 3.10 Current-voltage characteristics of the emitter-base and base-collector junctions at different V_{CB} and V_{EB}, respectively.

The EB (BC) JV curve is obtained by considering the BC (EB) at several operating conditions, i.e. short circuit (SC), maximum power point (MPP) and open circuit

(OC), in order to analyze the possible impact of the transistor effect discussed in Sec. 3.2.

As seen in Figure 3.10, the JV curve for the EB top sub-cell is the same at any operating condition since the injection from BC to EB junction is totally negligible owing to the higher EB open-circuit voltage with respect to that one of the BC junction. For the bottom sub-cell, the JV curves are the same except when the EB voltage V_{EB} approaches the OC value. Indeed, in this case, the transistor effect takes place enhancing the BC photo-current biased at their individual MPP. This effect has been observed experimentally in HBT tandems based on III-V semiconductors [60], arguing that it could be attributed either to photoluminescence coupling and/or transistor effect between the sub-cells. Further experiments supported by device modeling are needed to disentangle the impact of these two mechanisms. Nevertheless, the fact that carrier injection through the base is negligible for voltages lower or equal to the MPP voltage demonstrates the absence of a transistor effect in this device under useful operation conditions. Thus, the two junctions substantially work as independent and the total HBTsc efficiency at MPP is the sum of the efficiency achieved by each sub-cell biased at their individual MPP. The calculated photovoltaic parameters are reported in Tab. 3.2. The cell achieves a total efficiency ranging between $\sim$27.1% and 28.6% [53], depending on the assumed values for radiative recombination coefficient and intrinsic carrier density of the PVK layer (Tab. 3.1).

	Voc	**Jsc**	**Vmpp**	**Jmpp**	**FF**	**eff**
	[V]	$\left[\frac{\mathbf{mA}}{\mathbf{cm^2}}\right]$	**[V]**	$\left[\frac{\mathbf{mA}}{\mathbf{cm^2}}\right]$	**[%]**	**[%]**
EB	1.17 ÷ 1.25	20.8	1.05 ÷ 1.13	20.1	86.6 ÷ 87.4	17.89 ÷19.4
BC	0.66	19.7	0.58	18.8	83.9	9.21

Table 3.2 Calculated photovoltaic figures of merit of the proof-of-concept 3T-HBT according to the generalized Hovel model.

Chapter 4

TCAD Modeling of Perovskite/Silicon tandem

Device modeling plays a crucial role in optimization and development of solar cells. Several Technology Computer-Aided Design (TCAD) tools, based on partial differential equations are available. In this work, Sentaurus TCAD software from Synopsys [61] is used to simulate 2T and 3T-HBT PVS solar cells.

4.1 Simulation methodology

Sentaurus device is an advanced numerical tool capable of simulating the opto-electronic behavior of semiconductor devices. A set of physical equations, able to describe optical and transport mechanisms inside the device, are solved to compute currents and voltages at the external terminals. With this aim, we can divide the modeling tool flow (Fig.4.1) of a solar cell into two parts.
In the first part, we describe the geometry of the solar cell, meaning that we approximate a real solar cell device in a 'virtual' one whose physical properties are discretized onto a non-uniform grid of nodes. It is possible generate the device structure using the graphical user interface (GUI) or using scripts based on the Scheme scripting language (our case). The 'virtual' solar cell could have a 1D, 2D as well as 3D geometry. When we simulate devices based on several layers, such as a solar cell, each of them is described through its thickness, doping profile and material. Also, location of electrical contacts, boundaries and grid discretization are specified.

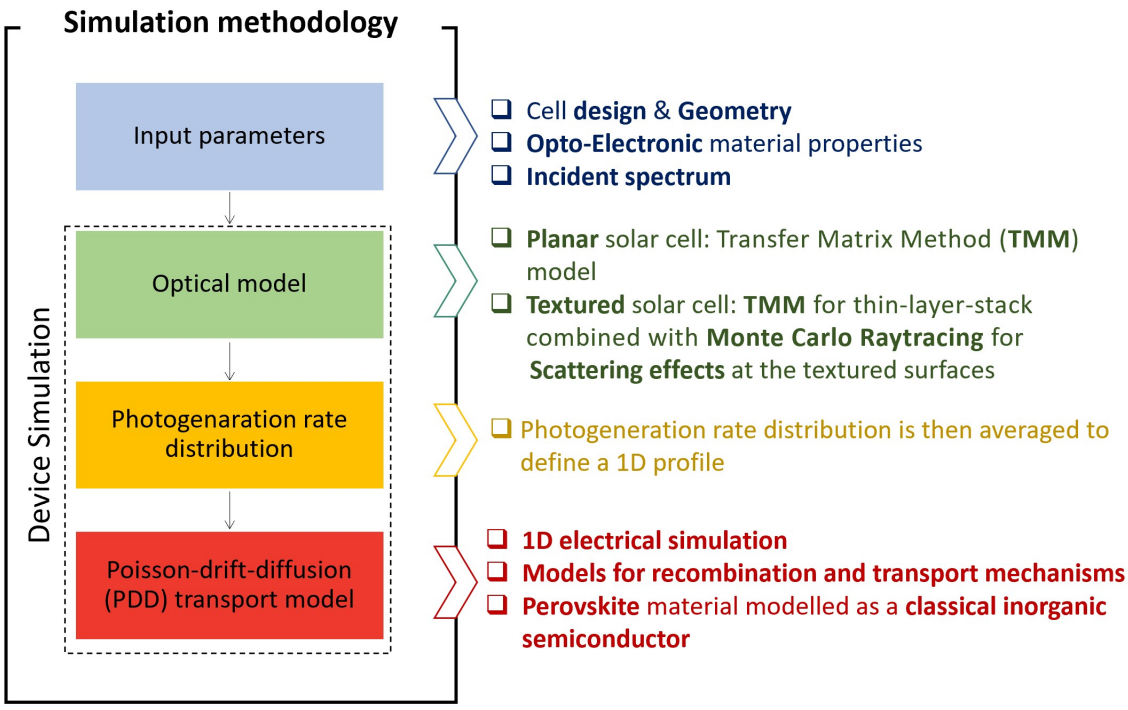

Fig. 4.1 Simulation Methodolgy: Opto-electronic model developed into Sentaurus TCAD software able to perform simulation of both planar/textured 2T and 3T solar cells.

For an optimal level of accuracy, a suitable mesh for the device under study must be created. In this regard, the main guidelines are that the mesh must be densest at semiconductor/semiconductor (oxide) interface, where there is a high electric field, or in those regions characterized by high carrier generation or high current density as well as in tunnel junction regions.

For each material involved in the device structure, optical and electronic properties such as carriers mobility, band structure, recombination properties, refractive index and absorption coefficient must be specified. The choice of material properties is fundamental to ensure accuracy of simulation results. A library, containing several material files, is available by Synopsys, however if the material description is not available, it can be defined by the user.

The second part of the tool flow (dashed box in Fig. 4.1) depends on the operating condition of the device. Indeed, if the solar cell is under illumination condition, it is necessary to evaluate the optical response before performing the electrical simulation. The choice of the electromagnetic model to be used depends on the geometry and design of the solar cell under study. For example, simulating a textured solar cell requires a hybrid optical model that combine Transfer Matrix Method (TMM)

for thin-layer-stack combined with Monte Carlo Raytracing to take into account scattering effects at the textured surface.
At the end of the optical simulation, the resulting photo-generation rate distribution (orange box in Fig. 4.1) is averaged to define an equivalent 1D profile and then given as input to the electrical modeling part (red box in Fig. 4.1) where the Poisson-drift-diffusion (PDD) transport model can be performed. Indeed, electrical simulations are carried out in 1D only because the simulation of a 2D or even 3D geometry would imply a very unfavorable (from the computational point of view) geometric aspect ratio between the direction of deposition of the multi-layer stack (which involves layers with nm and μm scale) and the direction parallel to the layers where one shall take into account of the spacing between the metal contacts (which is typically on the mm scale as discussed in Chapter 6). Therefore, in this work we have combined the mixed approach of 1D physics-based simulations with circuit level ones by identifying an equivalent lumped model for the device. Further development of the modeling strategy could involve the implementation of distributed 2D or 3D equivalent circuits like e.g. done in [62].

4.2 Optical model

Figure 4.2 shows the optical modeling flow implemented in TCAD. Whether the solar cell structure, planar or textured, the input parameter to the optical model are: the device design, optical properties of each material, i.e. extinction coefficient (k) and real part of the refractive index (n), as well as the illumination spectrum. The optical model must be run before the transport simulation to provide the 2D map of the optical generation rate as a function of wavelength. Optical simulations carried out in this work use the one-sun AM1.5G spectrum with incident power of 1000 W/m^2.
Once generated the desidered geometry and uploaded parameters of all materials used in the device, the second step is to develop an optical model whose resulting optical characteristics are the reflectance, transmittance, absorbance and the generation rate across the device. The absorbed photon density is calculated by the optical solver from the absorption coefficient and the spatial distribution of the electromagnetic field. Then, to calculate how many of the absorbed photons generate electron-hole pairs, it is possible to act on the *quantum yield* (QY) model. In TCAD Sentaurus, the

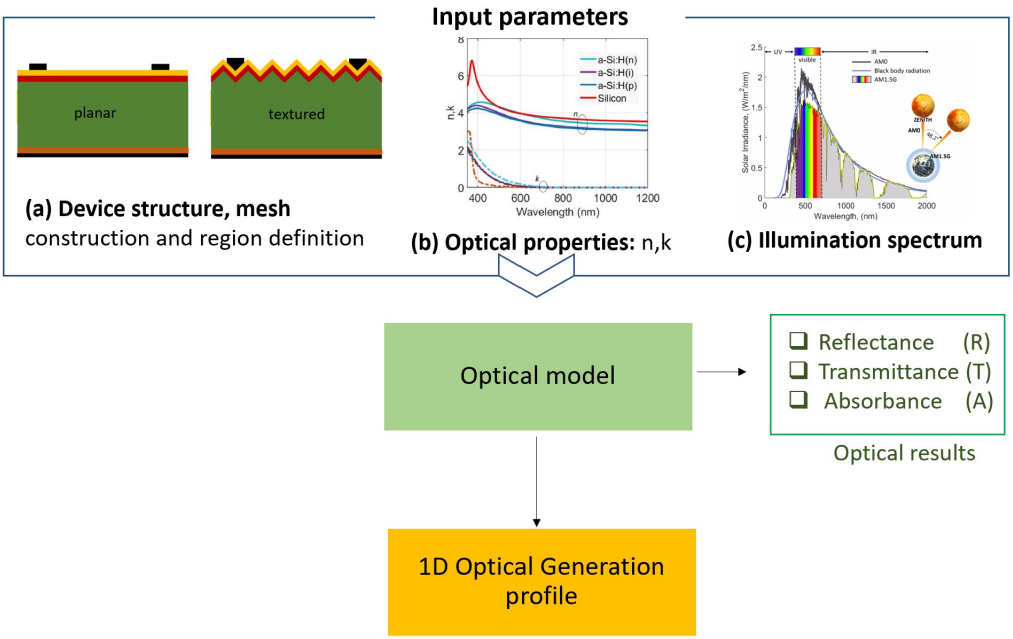

Fig. 4.2 Optical modeling flow implemented in TCAD

QY is set to zero, by default, for non-semiconductor regions. For semiconductors, the QY is defined as a step-function with respect to the energy bandgap, E_g: if the photon energy is greater or equal to the band gap, the QY is set to one, otherwise it is zero.

Among several optical solvers supported by TCAD Sentaurus, we use the transfer matrix method (TMM) to model flat solar cell structures and a hybrid method, TMM combined with RayTracing (RT), for textured PVS tandem cell. The Transfer Matrix Method is a formalism to describe the electromagnetic propagation in thin-film planar layered media where coherence effects are relevant. Details about the TMM model can be found in Appendix A.

In Sentaurus TCAD, it is possible simulate several types of textures such as *regular-pyramid* or *random-pyramid* in both two and three dimensions [63].

Let's consider a PVS device with periodic texture in two dimensions (Fig. 4.3). The periodicity assumption is mandatory to compute the optical generation profile only on the smallest optical symmetry element, i.e. one pyramid, obtaining fast and accurate results. The dashed box in Fig. 4.3 shows an example of TCAD Electrical grid where a PVS solar cell with inverted pyramidal texture is generated. The main issue to design the inverted pyramid relies on the fact that, to obtain accurate results,

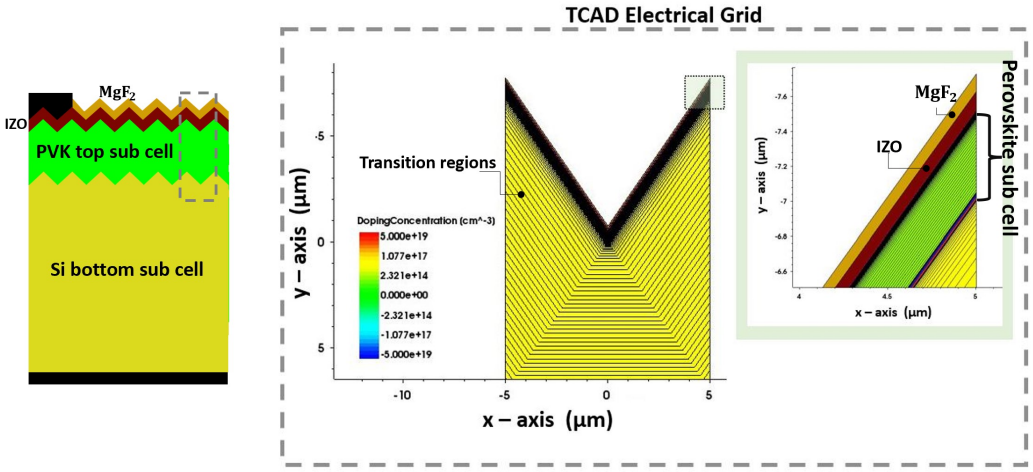

Fig. 4.3 Schematic view of a PVK/silicon tandem cell with textured front surface. In the dashed box, a zoom of the unit cell defining the TCAD simulation grid.

the pyramid cannot be built by simply stacking layers one on each other (as in flat solar cell), but it must be divided in several 'transition regions', whose area increases from the top to bottom, as shown in the TCAD Electrical Grid of Fig. 4.3, for the silicon substrate.

Considering the textured surface of Fig. 4.3, the optical absorption varies as a function of both vertical and horizontal direction. To obtain an accurate optical generation profile, it is necessary to use a finer mesh close to the regions underneath the top surface, hence performing the integral in each transition region [63].

The optical simulations of textured PVS solar cell is more complex not only for the geometry generation (Fig. 4.3), but also for the optical solver to be implemented. In fact, the simulations shall deal with both interference effects and absorption through the sub-wavelength multi layer stack (ARC, ITO, perovskite top-sub cell as well as a-Si:H thin films for hetero-junction based tandem) and scattering effects at the textured surfaces. Also, typical state-of-the-art PVS tandem is made on $\sim 180\ \mu$m silicon with a texture depth of $\sim 7\ \mu$m; these geometrical features are much larger than the wavelength. Thus, it is necessary to implement an optical model that is able to treat electromagnetic propagation across thin coherent and thick incoherent layers, and to include textured surfaces. In [64], Tonita et al. model bi-facial textured SHJ solar cells in Sentaurus TCAD. In details, the interference effects of ITO and a-Si:H layers are modeled with the TMM, then applied as boundary conditions at the front and

rear face of the c-Si substrate for the Monte Carlo Raytracing simulation. We have adapted the hybrid optical model in [64] to deal with the textured perovkite/silicon solar cell of Fig. 4.3.

Raytracing is based on geometric optics, it is robust but it is characterized by a high computation time [65]. In TCAD Sentaurus, raytracer optical solver uses a recursive algorithm; starting by a source ray, it builds a binary tree that tracks the transmission and reflection of the ray. These phenomena occur at each interface based on the refractive index of the regions involved, as illustrated in Fig. 4.4.

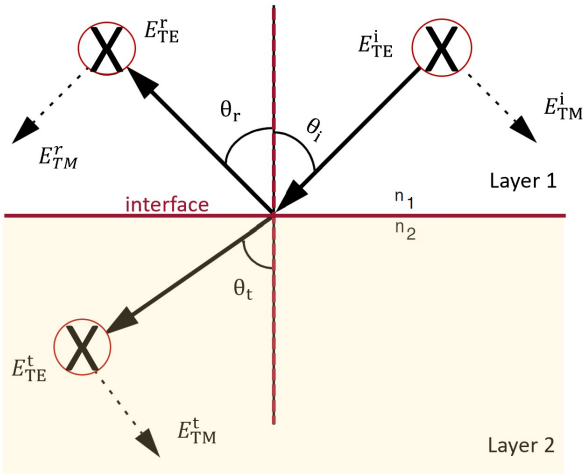

Fig. 4.4 Incident ray splits into reflected and transmitted ray at the interface. TE and TM components of the polarization vector are depicted as E_{TE} and E_{TM}, respectively.

In Fig. 4.4, an incident (i) ray impinges on the interface of two layers (Layer 1 / Layer 2) with different refractive index (n_1 and n_2), resulting in a reflected and transmitted ray. θ_{i}, θ_{r} and θ_{t} are the incident, reflected and transmitted angles linked by the *Snell's law*:

$$\theta_{\mathrm{i}} = \theta_{\mathrm{r}} \tag{4.1}$$

$$n_1 sin(\theta_{\mathrm{i}}) = n_2 sin(\theta_{\mathrm{t}}) \tag{4.2}$$

Once defined a plane of incidence that contains both the normal to the interface and the vector of the ray, it is possible to establish the concept of TE and TM polarization. If we consider a ray as a plane wave that travels in a specific direction, whose polarization vector is perpendicular to the direction of propagation, then the length of the polarization vector represents the amplitude, and the square of its length denotes the intensity [66]. The TE (TM) polarization is referred as the ray polarization vector

that is perpendicular (parallel) to the plane of incidence. The TE and TM components of the ray polarization vector, depicted respectively as E_{TE} and E_{TM} in Fig. 4.4, are characterized by different reflection (r_{TE}, r_{TM}) and transmission coefficients (t_{TE}, t_{TM}).
Lets's define $k_{1z} = n_1 k_0 cos(\theta_{\mathrm{i}})$ and $k_{2z} = n_2 k_0 cos(\theta_{\mathrm{t}})$ where $k_0 (= 2\pi/\lambda_0)$ is the free space wave number, and $\varepsilon_{1/2} = n_{1/2}^2$.
The field amplitude reflection coefficients read as [66, 67]:

$$r_{\mathrm{TE}} = \frac{k_{1\mathrm{z}} - k_{2\mathrm{z}}}{k_{1\mathrm{z}} + k_{2\mathrm{z}}} \tag{4.3}$$

$$r_{\mathrm{TM}} = \frac{\varepsilon_2 k_{1\mathrm{z}} - \varepsilon_1 k_{2\mathrm{z}}}{\varepsilon_2 k_{1\mathrm{z}} + \varepsilon_1 k_{2\mathrm{z}}} \tag{4.4}$$

The transmission coefficients for the TE and TM components are:

$$t_{\mathrm{TE}} = \frac{2k_{1\mathrm{z}}}{k_{1\mathrm{z}} + k_{2\mathrm{z}}} \tag{4.5}$$

$$t_{\mathrm{TM}} = \frac{2\varepsilon_2 k_{1\mathrm{z}}}{\varepsilon_2 k_{1\mathrm{z}} + \varepsilon_1 k_{2\mathrm{z}}} \tag{4.6}$$

Power reflection coefficients are:

$$R_{\mathrm{TE}} = |r_{\mathrm{TE}}|^2 \tag{4.7}$$

$$R_{\mathrm{TM}} = |r_{\mathrm{TM}}|^2 \tag{4.8}$$

Power transmission coefficients are:

$$T_{\mathrm{TE}} = \frac{k_{2\mathrm{z}}}{k_{1\mathrm{z}}} |t_{\mathrm{TE}}|^2 \tag{4.9}$$

$$T_{\mathrm{TM}} = \frac{\varepsilon_1 k_{2\mathrm{z}}}{\varepsilon_1 k_{1\mathrm{z}}} |t_{\mathrm{TM}}|^2 \tag{4.10}$$

For power coefficients, the sum of R and T must be equal to one. For normal incidence, $R_{\mathrm{TE}} = R_{\mathrm{TM}}$. At each interface, the raytracer solver computes the reflection and transmission coefficients of the TE and TM components depending on the angle of incidence.
Here, we adopt a Monte Carlo (MC) raytracing to account for rays randomly scatterd at the textured surface. Based on MC raytracing, reflectivity is taken as probability constraint to decide if the ray will be reflected or transmitted. As more rays impinge on the interface, the amount of reflected power is given by the total power of reflected rays (see [66], pp. 598-599). In textured PVS solar cell, the thickness of the thin-

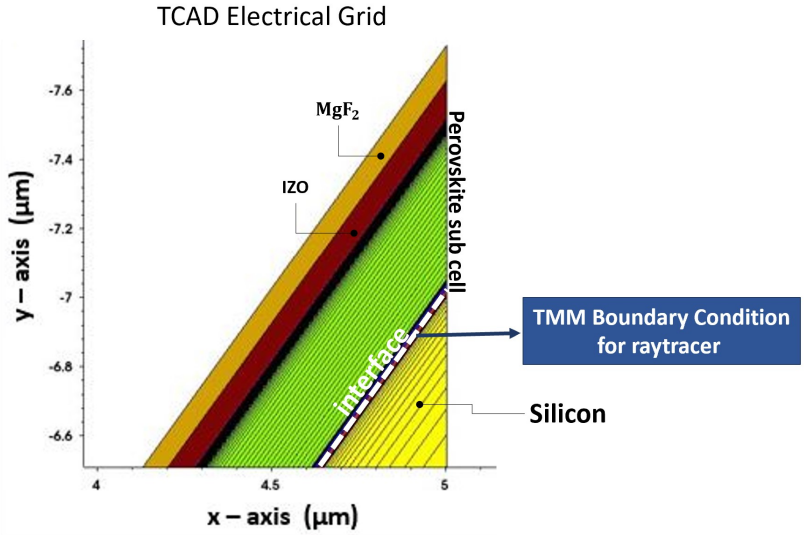

Fig. 4.5 TCAD simulation grid: the dashed line highlights the interface between the thin-layer-stack and the silicon substrate where the TMM BC is defined.

layer-stack of the PVK top sub cell is $\sim$ 500 nm (Fig. 4.5). Hence, to account for interference effect through the subwavelength multi-layered media, it is necessary to exploit the TMM simulation. In this regard, it possible to define special and spatially arbitrary boundary conditions (BC), at a certain interface, to include interference effects in raytracing [66]. The angle at which the ray is incident on the first layer of the textured surface is passed as input to the TMM solver, which simulates the incidence-angle-dependent propagation across the thin film layers; the resulting optical characteristics, i.e. reflectance, transmittance and absorbance for the two polarization, are then used to set the boundary condition for the raytracer at the front of the c-Si substrate [66, 68]. For the structures analyzed in this thesis, the whole stack of thin films above the Si thick layer (Fig. 4.5) is handled as boundary

condition (TMM BC) to the raytracer.
A key aspect is that layers specified in the boundary condition are defined only in the optical model and are not considered in the electrical grid. Fig. 4.6 clarifies

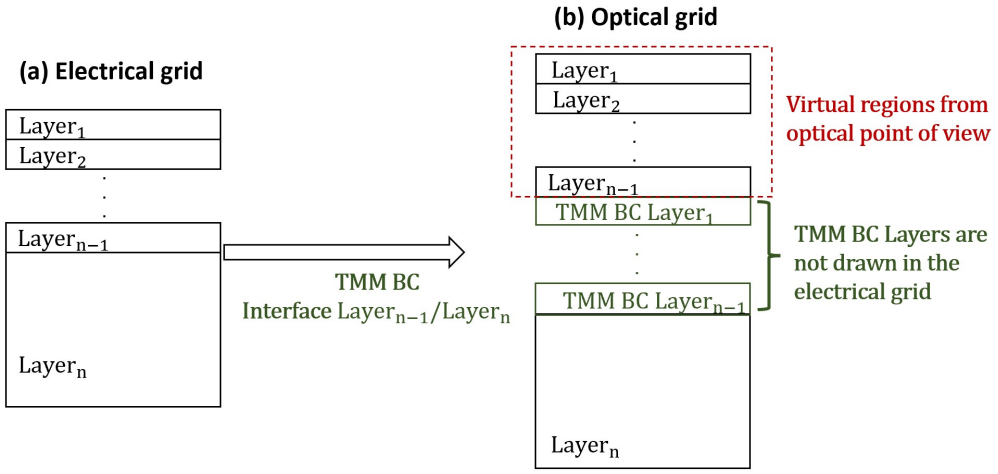

Fig. 4.6 Example of an application in which TMM BC are considered in the raytracer algorithm: (a) sketch of TCAD electrical grid, (b) optical grid where all the n-1 layers ($Layer_i$, i=1,..,n-1) are defined as virtual regions and n-1 TMM BC layers are added at the interface $Layer_{n-1}$/ $Layer_n$ to set the combined TMM-RayTracing simulation.

this point. Let us suppose that the first n-1 layers ($Layer_i$, i=1,..,n-1) are the thin film layers and $Layer_n$ represents the silicon thick region of the PVS solar cell. As discussed above, the thin n-1 layers must be treated with TMM. With this aim, let us define at the interface ($Layer_{n-1}$/$Layer_n$) of the electrical grid, the TMM BC for the raytracer (TMM BC $Layer_i$, i=1,..,n-1 in Fig. 4.6b). The TMM BC layers are considered only from the optical point of view, and are neglected in the transport model. Then, to correctly perform the optical simulation, the n-1 layers ($Layer_i$, i=1,..,n-1) are defined as 'virtual regions' [66] (red dashed box in Fig. 4.6b) such that, under illumination condition, the Ray tracing simulation ignores the presence of these regions. Thus, when optical simulation is performed, rays that enter or leave virtual regions are transmitted without change; no reflection or refraction occurs. It is important to highlight that, when we perform transport simulations, the device structure that we take into account is that one drawn in the Electrial grid. Hence, the concept of 'virtual regions' is relevant only for the sake of the optical simulation. In order to couple the optical and transport simulation, we need to define the optical generation profile across the whole device. In particular, since the first n-1 layers

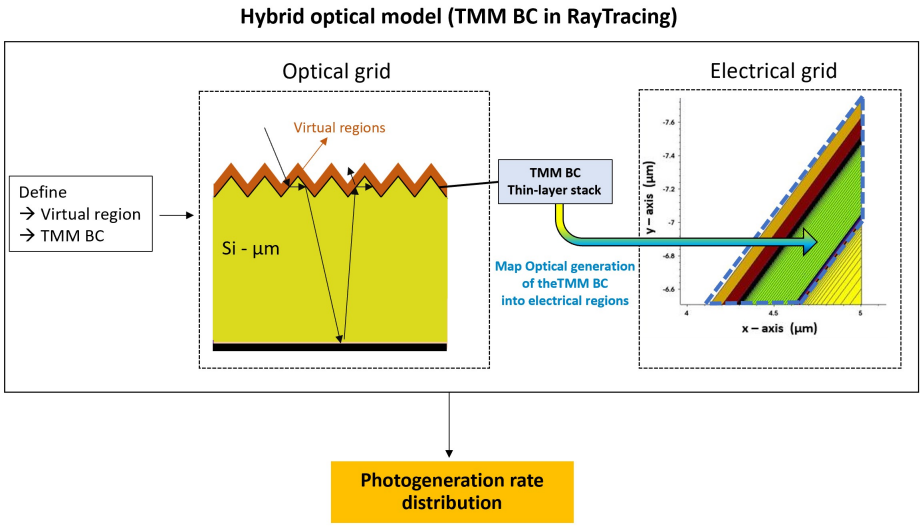

Fig. 4.7 Details of the optical modeling flow adopted to define the Hybrid optical model: from the definition of the virtual regions and TMM BC to the optical generation mapped from the TMM BC to the thin-layer-stack of interest.

are defined as virtual regions, the detailed electromagnetic field profile across them remains unknown. On the other hand, the optical simulation provides as output the fraction of absorbed photon flux in the whole domain identified as TMM BC. Thus, the optical generation in the thin-film layers (1,..,n-1) defined in the electrical grid, is calculated as a piecewise constant profile with a value, in each layer, given by the product of the Quantum Yield and the absorbed photon flux in the whole TMM BC domain weighted by the fractional volume of the single layer.

For textured PVS solar cells simulated in this work, it is assumed that the absorption in the top sub cell is due only to the perovskite layer. In this regard, the perovskite transition regions (green areas in Fig. 4.5) are designed of equal volume allowing a uniform distribution of the BC absorbed photon flux in that regions. Thus, across the whole PVK absorber material, we obtain a constant optical generation.

As a result, the simulation provides a 2D map of the optical generation rate across the device. Then, the obtained photo-generation rate distribution has been averaged to define an equivalent 1D profile given as input to the Poisson-drift-diffusion (PDD) transport model.

4.3 Transport model

At the end of the optical simulation, the device structure, proper material properties and the 1D generation profile are given as input to the electrical part of the device modeling, as shown in Fig. 4.8. Transport simulation is based on the PDD model. It

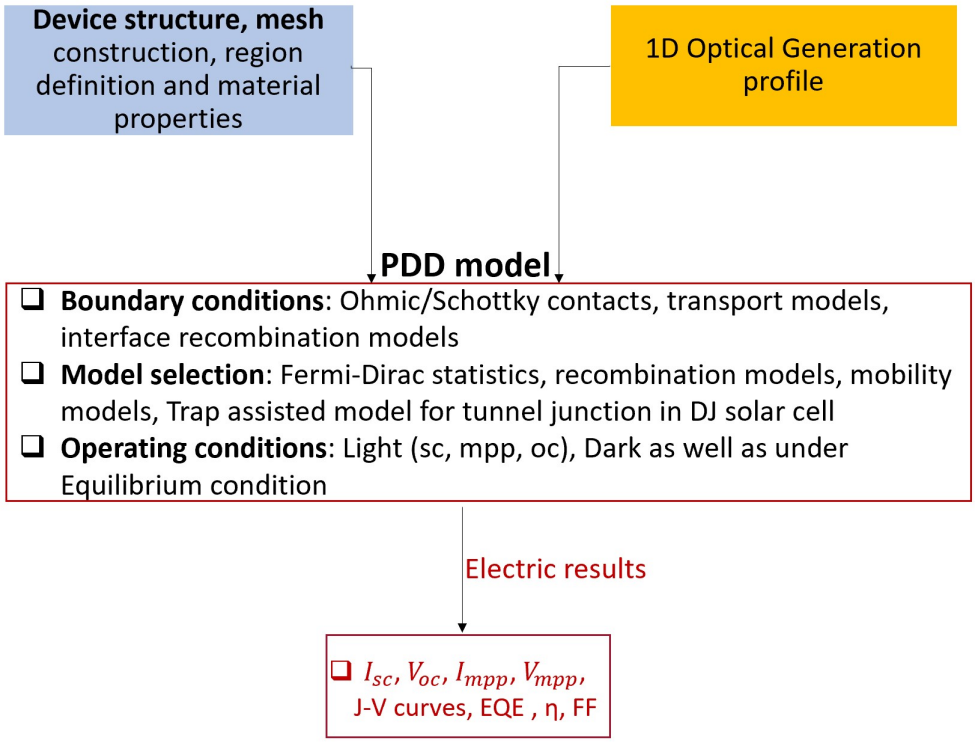

Fig. 4.8 Flowchart describing the electrical modeling approach implemented in Sentaurus TCAD for this thesis.

is formulated in terms of electron and hole continuity equations (Eq. 4.12 and Eq. 4.13) coupled to the Poisson equation (Eq 4.11).

$$\nabla \cdot (\varepsilon \nabla \psi) = q(n - p - N_{\mathrm{D}}^{+} + N_{\mathrm{A}}^{-}) \tag{4.11}$$

$$\frac{\partial n}{\partial t} - \frac{1}{q}\nabla \cdot \overrightarrow{J_{\mathrm{n}}} + U_{\mathrm{n}} - G^{\mathrm{ph}} = 0 \tag{4.12}$$

$$\frac{\partial p}{\partial t} + \frac{1}{q}\nabla \cdot \overrightarrow{J_{\mathrm{p}}} + U_{\mathrm{p}} - G^{\mathrm{ph}} = 0 \tag{4.13}$$

U_{n} and U_{p} are the net electron and holes recombination rates, G^{ph} is the photo-generation rate, $\overrightarrow{J_{\mathrm{n}}}$ and $\overrightarrow{J_{\mathrm{p}}}$ are the electron and hole current density, and finally n and p are the electron and hole density, respectively.
In Eq. 4.12 and Eq. 4.13, the net recombination rate $U_{\mathrm{p/n}}$ accounts for the effect of the Radiative, SRH and Auger recombination processes, previously mentioned in Section 2.1.2.
Radiative recombination rate is modeled as:

$$U_{\mathrm{rad}} = B_{\mathrm{rad}}(np - n_{\mathrm{i}}^2) \tag{4.14}$$

where B_{rad} is the bimolecular recombination coefficient, and n_{i} is the intrinsic carrier density. Under *low injection* condition, the equivalent carrier lifetime results as:

$$\tau_{\mathrm{rad}} = \frac{1}{B_{\mathrm{rad}} N_{\mathrm{A}}} \tag{4.15}$$

where n_0 and p_0 are the electron and hole carrier density at thermal equilibrium.
Auger recombination rate can be modeled as:

$$U_{\mathrm{Auger}} = (C_{\mathrm{n}} n + C_{\mathrm{p}} p)(np - n_{\mathrm{i}}^2) \tag{4.16}$$

where C_n and C_p are the Auger coefficients for electrons and holes. In a p-type material, in *low injection* condition, the equivalent Auger lifetime reads as:

$$\tau_{\mathrm{Auger,p}} = \frac{1}{C_{\mathrm{p}} N_{\mathrm{A}}^2} \tag{4.17}$$

Shockley-Read-Hall recombination rate through defects can be written as:

$$U_{\mathrm{SRH}} = \frac{np - n_{\mathrm{i}}^2}{\tau_{\mathrm{n0}}(p + p_1) + \tau_{\mathrm{p0}}(n + n_1)} \tag{4.18}$$

with:

$$n_1 = n_{\mathrm{i}} \exp\left(\frac{E_{\mathrm{trap}}}{k_{\mathrm{B}} T}\right) \tag{4.19}$$

$$p_1 = n_{\mathrm{i}} \exp\left(\frac{-E_{\mathrm{trap}}}{k_{\mathrm{B}} T}\right) \tag{4.20}$$

where E_{trap} is the difference between the defect level and intrinsic level, and τ_{n0} and τ_{p0} are the capture time constants for electrons and holes expressed as:

$$\tau_{\text{n0,p0}} = \frac{1}{\sigma_{\text{n,p}} v_{\text{th}} N_{\text{t}}} \tag{4.21}$$

v_{th} being the thermal velocity, N_{t} the defect concentration, $\sigma_{\text{n,p}}$ the capture cross-section for electron and hole.
Under *low injection* condition and assuming $\tau_{\text{n0}} \simeq \tau_{\text{p0}} = \tau_0$, the equivalent SRH carrier lifetime results as

$$\tau_{\text{SRH}} = \tau_0 \left[1 + \frac{2n_{\text{i}}}{N} cosh\left(\frac{E_{\text{Fi}} - E_{\text{trap}}}{k_{\text{B}} T} \right) \right] \tag{4.22}$$

where N is the net doping, and E_{Fi} the intrinsic Fermi level. For defects with energy at midgap ($E_{\text{trap}} \simeq E_{\text{Fi}}$), it turns out that $\tau_{\text{srh}} \simeq \tau_0$ regardless the doping level.
Finally, the *surface recombination* rate at the air-semiconductor, semiconductor-semiconductor or semiconductor-insulator interfaces is modeled using an expression analogous to that one in Eq. 4.18 for the bulk SRH recombination rate, and it reads as:

$$U_{\text{SRH}}^{\text{Surf}} = \frac{np - n_{\text{i}}^2}{\frac{(p+p_1)}{S_{\text{n}}} + \frac{(n+n_1)}{S_{\text{p}}}} \tag{4.23}$$

The S_{p} and S_{n} parameters are the recombination velocities (cm/s) for holes and electrons, respectively.
For the simulations presented in this study, only radiative recombination is assumed in the layers forming the perovskite top cell, while Auger and SRH are included in the simulation of the silicon bottom-cell. Although interface recombination play a critical role, especially in the perovskite cell, at this stage of the study the focus was on comparing the performance of the novel 3T-HBT architecture with respect to the classical 2T one. We expect that these assumptions affect in a similar way the performance of the two cells and therefore their comparative analysis remain valid. The inclusion of these mechanisms will however be essential to support the analysis of fabricated devices and guide their further development [69–71].
Eq. 4.11, Eq. 4.12 and Eq. 4.13 form a set of three coupled non-linear differential equations that enables the computation of carrier densities and electrostatic potential. The current densities for electrons (J_{n} in Eq. 4.12) and holes (J_{p} in Eq. 4.13), read as:

$$\overrightarrow{J_{\mathrm{n}}} = -qn\mu_{\mathrm{n}}\nabla\psi + qD_{\mathrm{n}}\nabla_{\mathrm{n}} \tag{4.24}$$

$$\overrightarrow{J_{\mathrm{p}}} = -qp\mu_{\mathrm{p}}\nabla\psi - qD_{\mathrm{p}}\nabla_{\mathrm{p}} \tag{4.25}$$

where ψ is the electrostatic potential. Alternatively, considering the electron and hole carrier density dependence on the of the Quasi-Fermi level ($E_{\mathrm{F,n}}$ and $E_{\mathrm{F,p}}$):

$$n = n_{\mathrm{i}} \exp\left(\frac{E_{\mathrm{F,n}} - E_{\mathrm{F,i}}}{k_{\mathrm{B}}T}\right) \tag{4.26}$$

$$p = n_{\mathrm{i}} \exp\left(\frac{E_{\mathrm{F,i}} - E_{\mathrm{F,p}}}{k_{\mathrm{B}}T}\right) \tag{4.27}$$

Eq. 4.24 and Eq. 4.25 can be written as a function of the electron and hole Quasi-Fermi levels:

$$\overrightarrow{J_{\mathrm{n}}} = \mu_{\mathrm{n}} n \nabla E_{\mathrm{F,n}} \tag{4.28}$$

$$\overrightarrow{J_{\mathrm{p}}} = \mu_{\mathrm{p}} p \nabla E_{\mathrm{F,p}} \tag{4.29}$$

Physical properties of the solar cell device are discretized onto a nonuniform (or uniform) 'grid' as discussed in Sec. 4.4, thus Eq. 4.11 to Eq. 4.13 are solved by Newton numerical method, available in Sentaurus.
The 2T PVS solar cells simulated in Chapter 5 exploit Si (*pn*) tunnel junction to allow current flow between top and bottom sub cell as depicted in Fig. 4.9. The Tunnel diode can be modeled in TCAD Senaturus by exploiting several band-to-band tunneling models such as Hurkx, Schenk and more simple ones [66]. Here, the tunnel diode is modeled by using the Schenk model with default material parameters[1], and the tunnel current is calculated by solving the Schrödinger equation in one dimension ([72], [66] pp. 722-734).

[1]Coefficients for band-to-band Schenk model: A = 8.97 $\times$ 10^{20} cm^{-1} s^{-1} V^{-2}, B = 2.14 $\times$ 10^{7} Vcm^{-1} $\mathrm{eV}^{-3/2}$, $\hbar\omega$=18.6 meV [66]

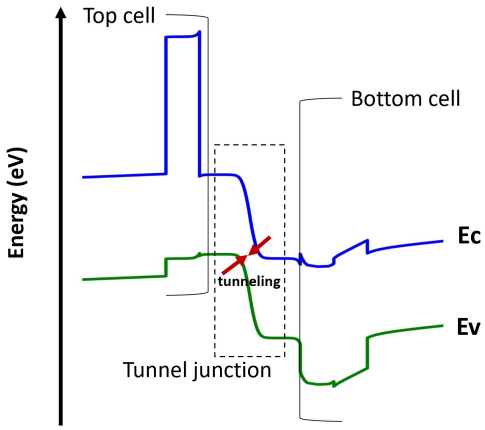

Fig. 4.9 Illustration of a band diagram in 2T tandem solar cell.

4.4 Simulation set-up

Sentaurus TCAD tool is able to perform 1D, 2D, 3D simulations with growing computational effort and accurate and predictive results. In general, a trade-off between accuracy and computation time is the key to choose the dimension of the simulation domain. For example, performing 3D simulations helps to describe with high accuracy real geometries, however the computation time is so high that executing them routinely is not feasible. In this work, since the geometry of the solar cell is such that a 1D description of the transport process is generally exhaustive, we have adopted the 1D and 2D domain for planar and textured device, respectively. For textured cells this implies some amount of underestimation of the predicted efficiency, without invalidating the general outcomes since the performance assessment of the 3T-HBT is always carried out with respect to a benchmark 2T device. In this regard, Fig. 4.10 illustrates the conceptual workflow of how a 2T tandem can be transformed into a 3T-HBT tandem.
We can identify three main steps:

- removing the n++/p++ tunnel junction
- flipping the *n-i-p* PVK layer into a *p-i-n* one (or equally the *n-p* bottom sub-cell into a *p-n* one)
- adding the base metal contact

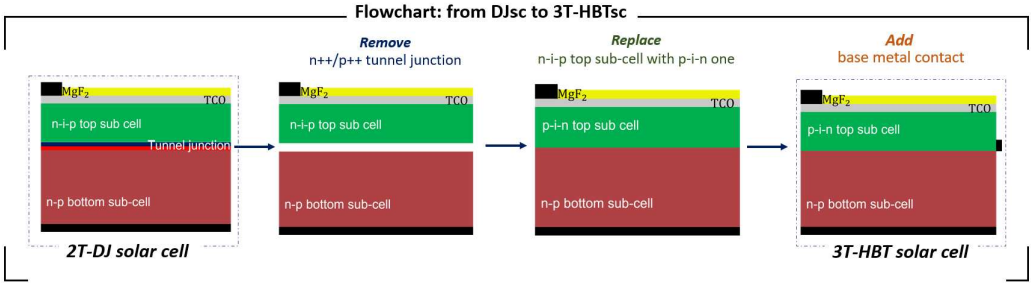

Fig. 4.10 A flowchart of the steps to turn the 2T tandem into a 3T-HBT tandem. The two structures are representative of the simulated geometries.

In Fig. 4.10, the base contact is schematically sketched as an additional lateral terminal, as done for the sake of simulating the *intrinsic* device performance. The possible implementation of a real device using interdigitated emitter/base contacts and their impact on the device efficiency is discussed in Chapter 6. Moreover, Sec 5.1.1 presents a brief discussion of a possible fabrication flow of the multilayer structure.

The optical and transport equations must be complemented with suitable boundary conditions at the edges of the device.

All the electrical contacts have been assumed as ideal ohmic contacts, with Quasi-Fermi levels of the semiconductor coincident with the contact one and charge neutrality at equilibrium. This turns into Dirichlet conditions for the electrostatic potential and charge carrier density.

At the interfaces perpendicular to the stacking direction (i.e. parallel to the x axis in Fig. 4.11), boundary conditions impose that the current density component normal to the interface is equal to the surface recombination rate, and the continuity of the electric displacement field. The boundaries parallel to the stacking direction (i.e. parallel to the y axis in Fig. 4.11) are treated with Neumann boundary conditions, ensuring no exchange of energy or particles with the surrounding domain.

Even though the structure of the simplest possible cell is inherently 2D (at least) due to the presence of local contacts at the top surface (Fig. 4.11a), in order to reduce the simulation domain to 1D, it is usual to extend the top contact to the whole front surface, analogously to the rear one. However, from the optical point of view, the front ohmic contact is treated as a transparent one and does not affect the optical simulation. Analogously, for the HBT structure, the lateral base contact in Fig. 4.10 is treated as transparent.

In Sentaurus Device, the concept of *illumination window* is used to confine the

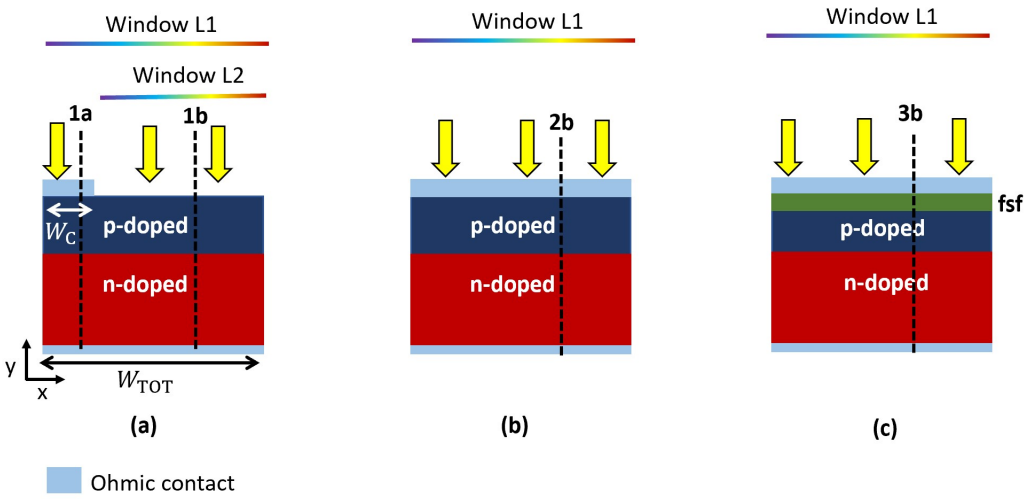

Fig. 4.11 Sketch of SJ solar cells: (a) with a contact width (W_C) lower than that one of the entire solar cell (W_{TOT}) (b) front contact extended to the whole surface (c) Ohmic contact (W_C=W_{TOT}) placed on the top of the front surface field. L2 (L1) is the illumination window that takes (do not take) into account possible shading effect.

incident light to a certain surface region. In this regard, considering the illumination window L1 (Fig. 4.11), simulation of the illuminated *pn* junction of Fig. 4.11a or that one of Fig. 4.11b is equivalent, and for both of them 1D simulations can be carried out. Otherwise, if one wants to account for shadowing effect due to the metal contacts, it is necessary to reduce the width of the illumination window (L2 in Fig.4.11a), scaling properly the width of the contact with respect to that one of the solar cell. In this case, we deal with a truly 2D case where the charge density varies strongly not only as a function of the y-direction, but also horizontally (x-axis). Indeed, in the illuminated region there is a significant amount of electron-hole pairs photo-generated, instead in the shadowed one beneath the contact (width W_C in Fig. 4.11a), carriers photo-generation does not take place. Thus, there is a strong gradient of minority carrier concentration at the interfaces of shaded/illuminated regions. The structure of Fig. 4.11a, that exploits the L2 illumination window, requires a highly non-uniform mesh: more dense under the metal contact and at the interface of shaded/illuminated regions. This increases the simulation computation time.
In general, the first strategy adopted to obtain a suitable mesh is considering a mesh

resolution limited by the Debye length D_{L} (Eq. 4.30).

$$D_{\mathrm{L}} = \sqrt{\frac{\varepsilon k_{\mathrm{B}} T}{N q^2}} \tag{4.30}$$

where N is the doping density of the considered semiconductor. In some cases, it can be necessary to refine the mesh density after the first simulation run, according to the region where strong charge variations occur.
The simulations presented in this work neglect the shadowing effect; both solar cells are entirely illuminated from the front surface to exploit a simpler mesh with low computation time.
However, with this set-up, another important aspect to consider is the boundary condition imposed on the surface nodes by the Ohmic contact. Indeed, from an electrical point of view, extending the Ohmic contact to the whole top/bottom surface imposes a different boundary condition at the surface affecting the solar cell simulation. Let's consider Fig. 4.11a, it is possible to identify two different boundary conditions (b.c.):

- at the contact/semiconductor interface (x=W_{C}, vertical cut 1a)

$$n_{\mathrm{p}} = n_{\mathrm{p0}} \tag{4.31}$$

- at the semiconductor/air interface (x>W_{C}, vertical cut 1b)

$$D_{\mathrm{n}} \frac{d(n_{\mathrm{p}} - n_{\mathrm{p0}})}{dy} = S_{\mathrm{n}}(n_{\mathrm{p}} - n_{\mathrm{p0}}) \tag{4.32}$$

We highlight that Eq. 4.32 is equivalent to Eq. C.2, that is the surface boundary condition in the Hovel model for the emitter region. Eq. 4.32 leads to Eq. 4.31, at the surface ($y = 0$), when the surface recombination velocity S $\rightarrow \infty$ (Ohmic contact case). Under illumination, depending on the extinction coefficient of the absorber material, absorption and carrier generation can occur well below the semiconductor surface (in the photoactive layers with high collection efficiency) or very close to the surface, depending also on the incident wavelength [18]. In any case, the minority carrier profile will be affected by the presence of the electrical contact, leading to inaccurate results. In particular, the higher the surface recombination rate, the worse the collection efficiency of photogenerated carriers. However, this issue occurs only

when the photoactive region is placed directly in contact with the Ohmic contact. Indeed, when a high-gap layer, the so-called front surface field (FSF), is placed between the photoactive region and the metal contact, only the collection of short-wavelength photogenerated carriers worsen, while most of the cell spectral response remains unaffected. Thus, we obtain that simulations carried out with the structure of Fig. 4.11c provide sufficiently accurate results, with a marginal difference with respect to those obtained with the structure of Fig. 4.11a for the same illumination window L1.

For the PVS solar cells under study, 1D simulations, with the metal contact covering the whole surface, provide accurate results because between the perovskite absorber and the Ohmic contact there is always, at least, a HTL or ETL high-gap material acting as FSF.By exploiting a 1D model, we neglect both electrical and optical losses. This allows to assess the performances of the multi-layer stack. Then, as discussed in Chapter 6, power losses associated to the middle contact can be conveniently evaluated through circuit-level simulations.Finally, a critical aspect to ensure accurate and somehow predictive simulation results for the devices under study is to employ material parameters and models suitable for the technology under study. Since in literature, for perovskite cells, opto-electronic models and parameters are not so well consolidated as for silicon ones, we have verified that the presented simulations are able to reproduce quite accurately published experimental results, as it will be discussed in Section 5.2. This, and the background laid by the analytical model described in Chapter 3, makes us confident that the presented results are capable to grasp the fundamental mechanisms underlying the proposed device. Clearly, a refinement of the model and material parameters will be needed at the time when some prototype is realized.

Once concluded the optical-transport simulation, it is possible to obtain the External Quantum Efficiency (EQE) and current-voltage characteristics of the solar cell device. In TCAD Sentaurus, the parameters extraction can be performed by using the extraction library of Sentaurus Visual [61]. However, to obtain the EQE as well as the JV characteristic of a certain device, it is necessary to perform suitable physics simulations depending on the case study.

Under short-circuit conditions, the EQE reads as

$$EQE(\lambda) = \frac{J_{\mathrm{sc}}(\lambda)}{J_{\mathrm{in}}(\lambda)} \tag{4.33}$$

where $J_{sc}(\lambda)$ is the short-circuit current density, and $J_{in}(\lambda)$ the equivalent incident photon current density. Thus, the emitter-base (base-collector) EQE of the 3T-HBT solar cell is obtained putting in short-circuit the corresponding sub-cell. Instead, the emitter-base (base-collector) J-V curve, is computed performing the simulation by sweeping the emitter-base (base-collector) voltage, once the base-collector (emitter-base) voltage is set at a certain operating point. Thus, the output current density, at each voltage point, is evaluated at the emitter or collector terminal depending on the bias condition of both junctions.
The EQE and J–V curve of each sub-cell of the 2T DJ tandem are more tricky to compute due to its series-connected architecture. The J–V curve of the tandem cell (Figure 4.12a) is obtained by sweeping the tandem voltage (V_T). To compute the JV curves of each sub-cell, a constant doping profile is added to deactivate the other cell [72]. As sketched in Figure 4.12b (c), the J–V curve of the top (bottom) sub cell is computed by replacing the other cell and tunnel junction with a region with a constant doping.

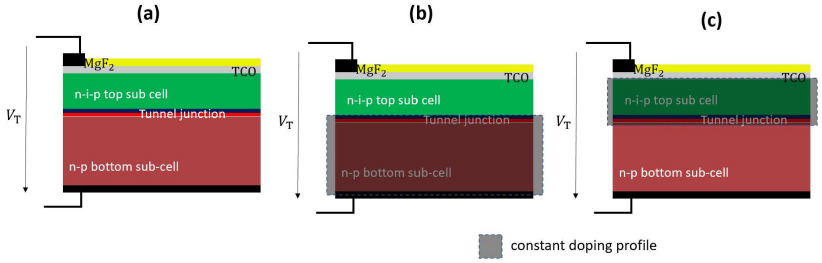

Fig. 4.12 Simulation set-up for the 2T tandem cell in order to evaluate: (a) the current-voltage characteristic, (b) the EQE and J-V of the top cell only, by adding a constant doping profile over the entire bottom cell and the tunnel diode that short-circuits the bottom cell, (c) the EQE and J-V of the bottom cell only, by adding a constant doping profile over the entire top cell and the tunnel diode that short-circuits the top cell.

Moreover, in order to compute the EQE curves for the individual cells of the 2T tandem, different illumination spectra are applied [72], taking advantage of the current matching constraint of the tandem cell. To this aim, part of the spectrum file of the light source is scaled based on the sub cell being investigated, as sketched in Fig. 4.13. A scaling factor is applied to the long (short) wavelength range of the spectrum to investigate the EQE of the top (bottom) cell. The scaling factor is chosen in such a way that the bottom (top) cell produces enough current, so that the other cell is current limiting. For example, in Fig. 4.13 it is defined a scaling factor

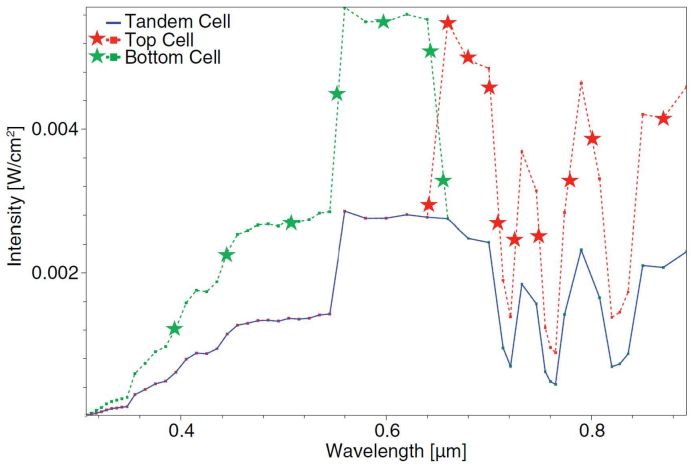

Fig. 4.13 Illumination spectra to calculate the individual EQE of the top and bottom cells [72].

equal to 2 and a crossover wavelength that separates the upper and lower sides of the illumination spectrum equal to 0.65 μm. Thus, by considering the top (bottom) cell illumination spectra (red (green) curve in Fig. 4.13), the $J_{sc}(\lambda)$ is current limited by the top (bottom) sub-cell. Then, from Eq. 4.33, one obtains the EQE of the current-limiting sub-cell.

Chapter 5

Physics-based simulation of planar and textured 3T-HBT solar cell

In this chapter, we carry out a thorough analysis of the 3T hetero-junction bipolar transistor photovoltaic behavior [43] by exploiting the numerical tool discussed in Chapter 4. Firstly, we focus on a planar perovskite/silicon three-terminal tandem based on the hetero-junction bipolar transistor architecture to investigate its potential, and possible bottlenecks, with respect to more conventional two-terminal double junction tandems. Then, we propose a second design of HBT cell developed starting from a fully textured monolithic perovskite/silicon 2T tandem solar cell reported in literature [73]. In this regard, simulations are firstly verified against experimental data and then used to analyze the performance of the proposed PVS 3T-HBT solar cell with respect to the 2T one. For both planar and textured HBT tandem, the extra terminal is implemented at the common selective layer between the perovskite and silicon sub-cells. By optical and transport simulations of the tandem multilayer stack, we show that the efficiency of the 3T-HBT architecture can compete with the series-connected tandem one under nominal operating conditions,while relying on standard materials and layer thickness.

5.1 Planar HBT PVS tandem

Figure 5.1a shows a schematic drawing of a PVS 3T-HBT tandem where a *n-i-p* perovskite sub-cell is stacked on top of a HTJ (or HIT) bottom cell made of *p*-type c-Si. The *emitter* is formed by the HTL and perovskite absorbing layer. Then, the ETL and the a-Si:H layers form the *base*; finally, the *p*- type c-Si acts as the HBT *collector*. The three contacts, for *emitter*, *base*, and *collector* are named as T, Z, and R, respectively, following the notation in [74]. Figure 5.1b shows the equivalent electrical circuit of the HBT tandem. The top *emitter-base* (EB) and bottom *base-collector* (BC) junctions form two back-to-back connected solar cells, modeled by a photogenerated current generator (J^{ph}_{BE} and J^{ph}_{BC}) in parallel to a diode with reverse saturation current J^{D}_{Top} and J^{D}_{Bot}, and connected to two separate loads. Thus, under illumination, the total electrical power generated by the tandem is the sum of the electrical powers provided to the loads connected across the T-Z and Z-R terminals.

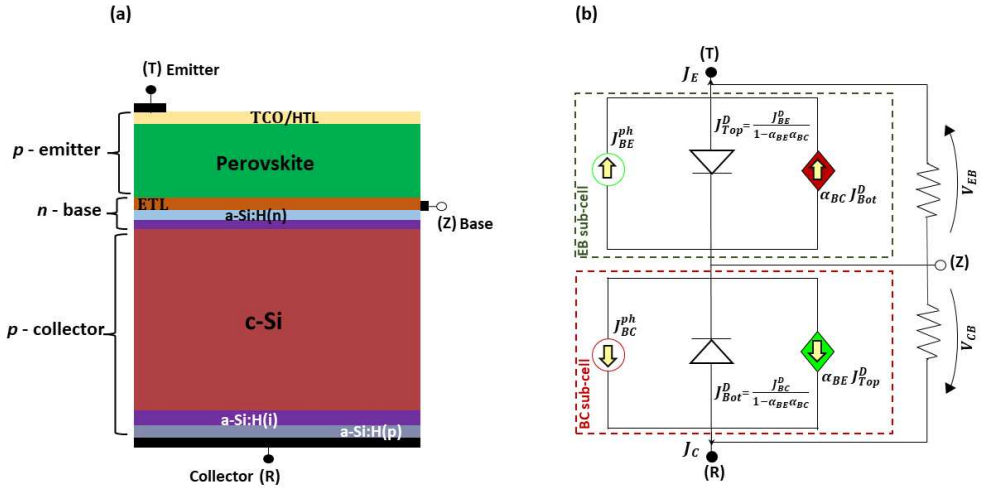

Fig. 5.1 (a) Schematic view of a 3T-HBT perovskite/HIT-silicon tandem. The three contacts for emitter, base, and collector are named as T, Z,and R, respectively. (b) Equivalent electrical circuit of the p-n-p 3T-HBT solar cell sketched on the left under illumination.

As discussed in Section 3.2, the current-controlled current source $\alpha_{BE}J^{D}_{Top}(\alpha_{BC}J^{D}_{Bot})$ accounts for the transistor action, *i*.e. the effect of the EB voltage on the BC junction due to the injection of minority carriers from the emitter toward the collector (and vice versa) through the common base layer. From the perspective of photovoltaic

operation, the transistor action shall be minimized [60, 52] because it would cause a reduction, albeit limited, of the maximum achievable power conversion efficiency. With the aim at verifying the preliminary findings discussed in Section 3.2 on the basis of the analytical model, in the following, we analyze the performance of the proposed 3T-HBT solar cell (Figure 5.1) with respect to its 2T tandem counterpart.

5.1.1 Device structure and model parameters

Figure 5.2 sketches the 2T-DJ and the 3T-HBT solar cells studied in this work.

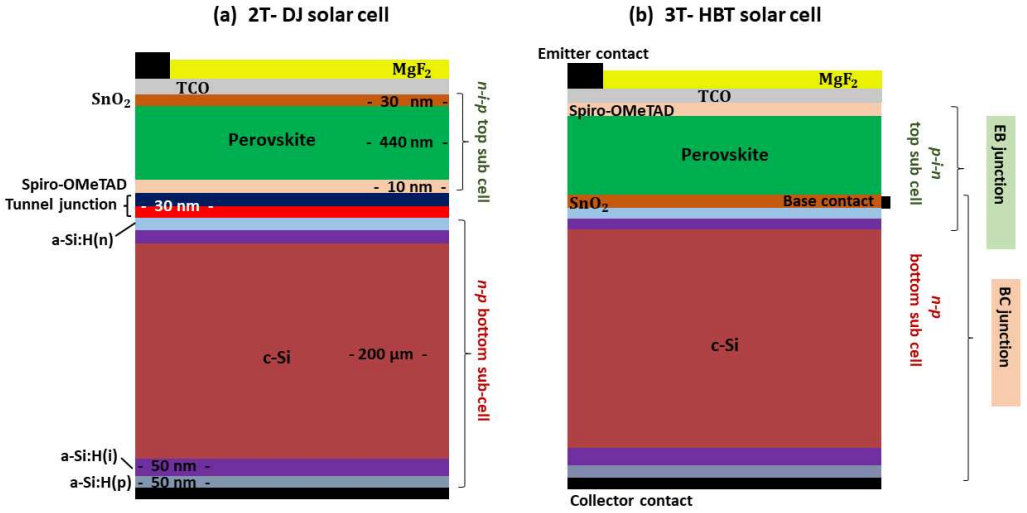

Fig. 5.2 Schematic view of the simulated PVS tandem with (a) 2T DJ structure and (b) 3T-HBT structure.

The 2T tandem is made of a *n-i-p* PVK solar cell stacked on top of an *n-p* Si HIT bottom cell. The two sub-cells are connected through a p^{++}/n^{++} Si tunnel junction (Figure 5.2a). The PVK sub-cell consists of a 440 nm perovskite absorbing layer [75, 57] sandwiched between a 30 nm thick SnO_2 ETL [76, 77] and a 10 nm thick Spiro-OMeTAD HTL [76, 75]. The HIT sub-cell consists of 200 μm *p*-doped c-Si sandwiched by two thin films of hydrogenated amorphous silicon (a-Si:H), made of 50 nm of *n*- (*p*-)doped a-Si:H and 50 nm of intrinsic a-Si:H. In the simulations, we assume a 107 nm thick MgF_2 anti-reflection layer and fully transparent TCO layer. Regarding the perovskite top sub-cell, the ETL and HTL materials are chosen based

on previous literature studies [73, 78, 79].

As discussed in Section 4.4, from a conceptual point of view, the 3T-HBT solar cell structure can be obtained by the DJ cell through three simple steps: removing the tunnel junction, flipping the *n-i-p* PSC and implementing the third lateral *base* contact at the SnO_2 layer. In a typical fabrication flow [43], SnO_2 would be deposited directly over the a-Si:H layer by solution processing: for instance, by using the colloidal dispersion of nanoparticles [80]. In case of textured substrates, conformal deposition could be based on chemical bath deposition as well as sputtering [81, 82]. The perovskite layer can be deposited either by solution processing or by thermal evaporation [83]. The same type of wet or vacuum deposition can also be used for the Spiro-OMeTAD [80]. The transparent electrode can be deposited by the sputtering of indium tin oxide, which is followed by the deposition of the antireflection layer of MgF_2 [84]. Finally, two metal grids can be deposited on the emitter and base contacts after a laser ablation step to remove the MgF_2 or the entire PSC stack, respectively. The resulting device sketched in Figure 5.2b consists of: Spiro-OMeTAD and PVK layers to form the *emitter* region, SnO_2 and (*n*)-(*i*) a-Si:H layers to form the *base* region, and finally, c-Si and (i)-(p) a-Si:H layers to form the *collector* region. Thus, one obtains a tandem with two sub-cells made by the *p-i-n* EB and the *n-p* BC junctions.

To assess the photovoltaic performance, the opto-electronic model discussed in Chapter 4 is exploited. Since both devices under study are characterized by a flat surface, the optical carrier generation profile is calculated using the Transfer Matrix Method (TMM) and then given as an input to the Poisson drift diffusion transport model. In this regard, we have verified that the choice to adopt the TMM rather than an hybrid optical model (Sec. 4.2), including the RayTracing (RT) for thicker Silicon region, still provides accurate results with lower computational costs. Optical simulations are carried out assuming AM1.5G illumination spectrum (total power of $\approx$100 mW/cm^2) at normal incidence.

Following previous work in literature [75, 76, 85, 86], perovskite, ETL and HTL materials are modeled as classical crystalline semiconductors. Table 5.1 summarizes the main material parameters and doping levels. We exploit, as perovskite absorbing layer, the widely used methylammonium lead triiodide $CH_3NH_3PbI_3$ with $E_g = 1.5$ eV, covering the entire visible region ($\lambda < 800$ nm) [76]. Spiro-OMeTAD and SnO_2 band parameters were also taken from [76]. Figure 5.3 reports a schematic representation of the assumed band alignment between the different materials and

Table 5.1 Main parameters value. E_g: Bandgap χ: Electron affinity ε_r: Permittivity $N_c(N_v)$: Density of states mu: Mobility τ: Lifetime. (e/h): electron/hole; if not specified, the shown value is the same for both carriers.

	PVK Top Cell			**HIT Bottom Cell**	
	Spiro-OMeTAD	**Perovskite**	**SnO_2**	**a-Si:H** [57]	**c-Si** [61]
E_g **(eV)**	2.95 [76]	1.5 [76]	3.28 [76]	1.7	1.1
$q\chi$ **(eV)**	2.18	3.93	4.35	3.9	4.05
ε_r	3	6.5 [57]	9.6	11.9	11.9
N_c **(cm^{-3})**	2.2×10^{18}	2×10^{18}	4.1×10^{18}	2.8×10^{19}	2.8×10^{19}
N_v **(cm^{-3})**	1.8×10^{19}	2×10^{18}	4.1×10^{18}	1.0×10^{19}	2.6×10^{19}
μ **(cm^2/Vs)**	0.0002 [75]	11.8 [75]	240 [77]	$20^{[e]}$ $5^{[h]}$	$1177^{[e]}$ $424^{[h]}$
N (cm^{-3})	5×10^{18}	2×10^{14}	5×10^{18}	$10^{19}_{doped}/10^{14}_{intrinsic}$	1×10^{16}

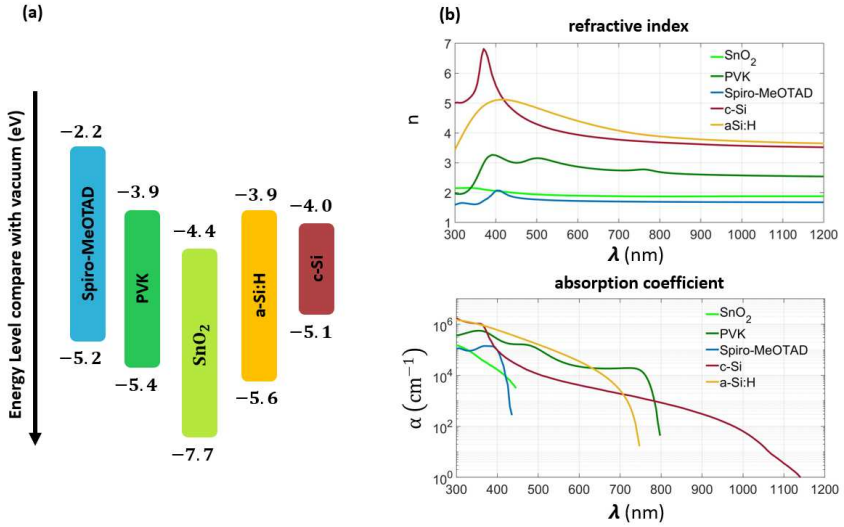

Fig. 5.3 (a) Schematic representation of band structure and energy levels of various materials used in the perovskite/silicon tandem analyzed in our study. (b) Real part of the refractive index (top) and wavelength-dependent absorption coefficient (bottom) for the materials used in the PVK and HIT sub-cells.

the wavelength-dependent refractive index and absorption coefficient used in the TMM optical simulation. Simulations consider radiative recombination only, with the radiative recombination coefficient set to 8×10^{-10} cm^3/s [87] for all the PVK sub-cell materials, 1.8×10^{-15} cm^3/s for a-Si:H [57] and 4.73×10^{-15} cm^3/s for c-Si [61].

Figure 5.4 shows the energy band diagram under thermal equilibrium condition for

the 2T DJ and HBT solar cells. In Figure 5.4, it is well visible the flipping of the PVK top cell and the presence of the tunnel junction made by highly doped ($5 \times \sim 10^{19}\text{cm}^{-3}$) silicon in the DJ structure. The tunnel diode of the 2T DJ is modeled by using the tunneling model discussed in Section 4.3.

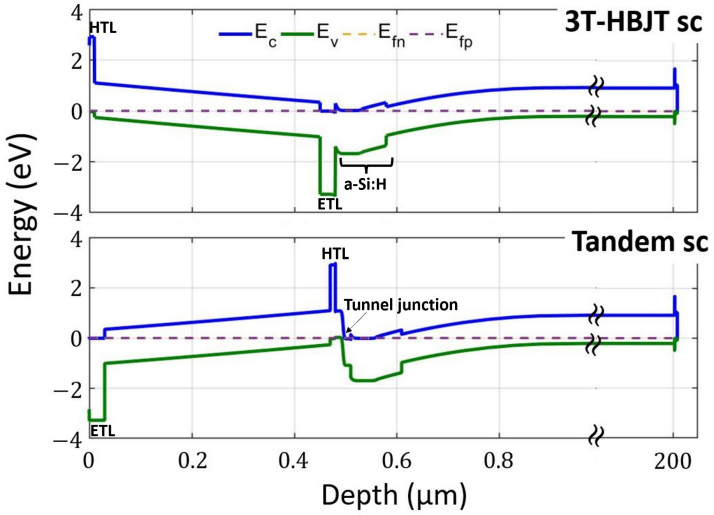

Fig. 5.4 Energy band diagram of the 3T-HBT (top) and DJ (bottom) tandems under thermal equilibrium condition.

5.1.2 Simulation results

Figure 5.5, shows the calculated reflectance and absorbance of the DJ and 3T-HBT devices. We can observe that reflectance of the 3T-HBT device, at low wavelength (<500 nm) and in the silicon harvesting range (800 –1000 nm), has a slight penalty with respect to the DJ tandem, therefore worsening the EQE, as seen in Figure 5.6. The penalty in the reflectance relies on the different top sub-cell architecture: *n-i-p* and *p-i-n* top sub-cell for the DJ and HBT tandem, respectively. Indeed, the HBT is illuminated from the Spiro-OMeTAD layer whose refractive index is higher than that one of the SnO_2 layer [88]. To improve the optical performance of the HBT tandem, it would be possible flipping the bottom silicon sub-cell, instead of the top one, to obtain an *n-p-n* 3T-HBT solar cell [68]. In this case, the solar cell would be illuminated from the *n*-side (SnO_2 layer), the Spiro-OMeTAD layer being below the PVK one, analogously to the 2T DJ solar cell in Figure 5.2, thus preventing the spectral loss induced by the Spiro-OMeTAD layer in the HBT under study [68].
On the other hand, we anticipate that the choice of a *n-i-p* rather than *p-i-n* top

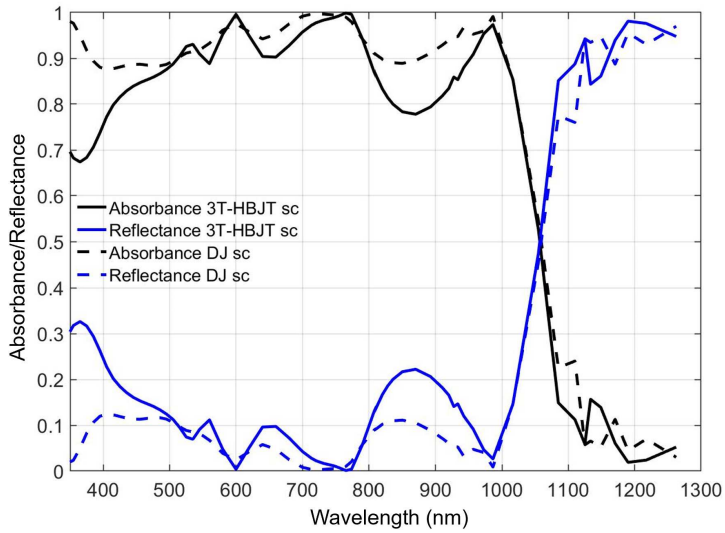

Fig. 5.5 Absorbance and Reflectance for the 3T-HBT (solid line) and 2T-DJ (dashed lines) solar cells.

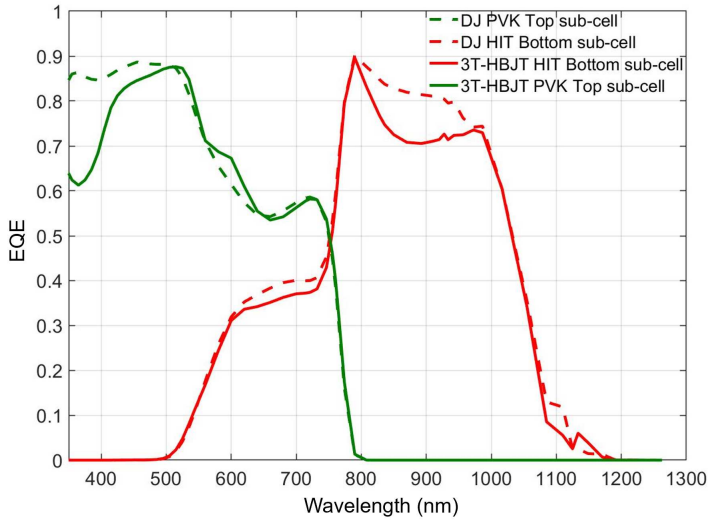

Fig. 5.6 External Quantum Efficiency for the 3T-HBT (solid line) and 2T-DJ (dashed lines) solar cells. EQE, for both devices, is computed by following guidelines discussed in Section 4.4.

sub-cell architecture, could worsen the electrical performance of the HBT tandem on HTJ silicon bottom cell. Indeed, the third base metal contact prompts lateral transport in the base layer generating resistive power losses. In this sense, we will show, in Chapter 6, that a different HBT architecture based on homo-junction Silicon bottom sub-cell can relax the electrical constraints on the *npn* or *pnp* configuration

to be adopted. An overview about several aspects affecting the design of HBT architectures made on hetero and homo-junction silicon bottom cell will be given in Chapter 6.
For the sake of the following discussion, we notice that the penalty in the EQE of the HIT cell turns to be almost irrelevant in terms of the comparative performance of the HBT and DJ tandems. In fact, as reported in Table 5.2, the current in the DJ tandem is limited by the top cell.

		Voc [V]	**Jsc** $\left[\frac{\mathbf{mA}}{\mathbf{cm^2}}\right]$	**Vmpp** [V]	**Jmpp** $\left[\frac{\mathbf{mA}}{\mathbf{cm^2}}\right]$	**FF** [%]	**eff** [%]
3T-HBT sc	**PVK Top sub-cell**	0.99	17	0.89	16.42	87.21	14.73
	HIT Bottom sub-cell	0.59	17.2	0.51	16.3	82.16	8.33
	Tandem Cell	-	-	-	-	-	23.06
DJ sc	**PVK Top sub-cell**	0.99	17.2	0.9	16.68	87.65	15.01
	HIT Bottom sub-cell	0.58	18.44	0.48	17.37	78.18	8.44
	Tandem Cell	1.57	17.2	1.39	16.8	85.88	23.38

Table 5.2 3T-HBT & DJ solar cells: Figures of merit.

In this regard, Figure 5.7 shows the simulated *J-V* characteristics of the 2T-DJ and of the 3T-HBT tandems obtained based on the guidelines of Sec. 4.4. At short circuit, we can observe that the bottom cell provides a higher current in the 2T-DJ structure than in the 3T-HBT one, which is due to the above-mentioned penalty in the EQE.

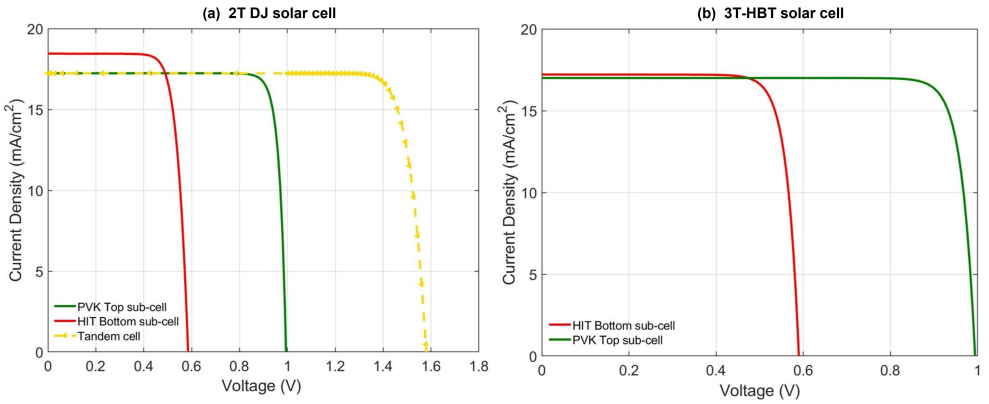

Fig. 5.7 On the left, J-V characteristics of the flat 2T PVK/Si DJ solar cells. On the right, J-V characteristics of the flat 2T PVK/Si 3T-HBT solar cell.

This difference, however, does not affect the tandem efficiency, because the short circuit current of the DJ tandem is limited by the top cell due to the current matching constraint. As a result, the two devices deliver a comparable current flow to the loads. The open circuit voltages are similar in the two devices, with a difference of the order of 10 mV (Table 5.2).

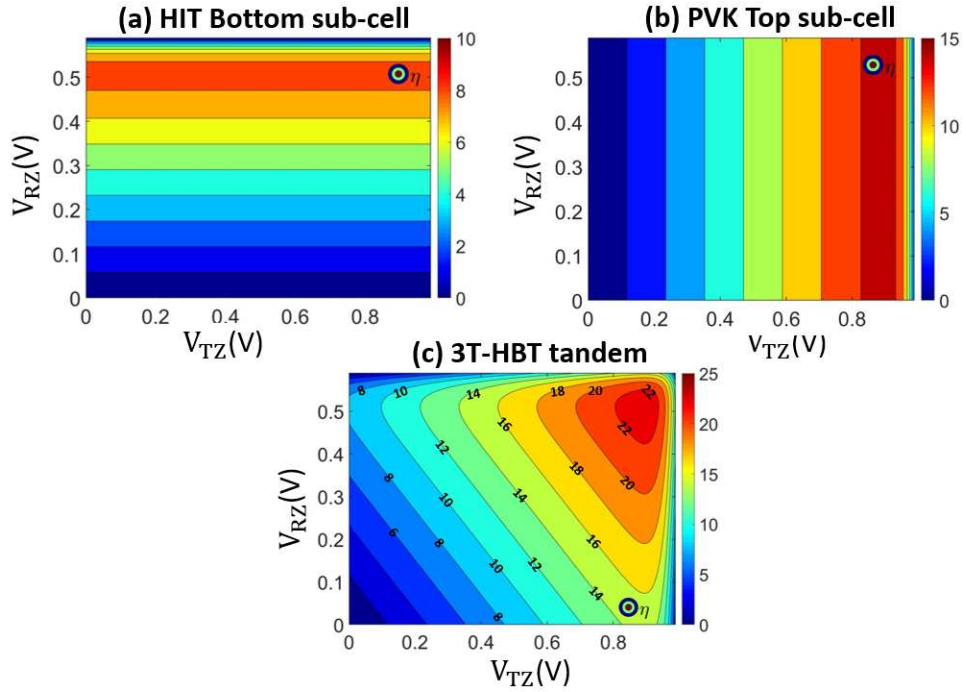

Fig. 5.8 (a) Efficiency as a function of the TZ and RZ voltages for: (a) HIT bottom sub-cell; (b) PVK bottom sub-cell; (c) 3T-HBT tandem.

As discussed in Section 3.2, and also pointed out in Sec. 5.1, the EB and BC junctions of the 3T-HBT solar cell might be influenced each other owing to the transistor action through the common base layer. Thus, to assess the impact of this effect on the photovoltaic performance, we have simulated the current–voltage characteristic of each sub-cell taking into account the operating condition of the other one. Figure 5.8 reports three contour maps, showing how the efficiency of the two sub-cells and of the entire device changes as a function of the emitter-base and base-collector voltages, V_{TZ} and V_{RZ} respectively.
It can be observed that the efficiency of each sub-cell varies with its own voltage only, and is practically independent on the operating voltage of the other one. Therefore, the Maximum Power Point (MPP) of the tandem corresponds to the MPP of the two sub-cells working as if they were isolated from each other. This is reflected in the energy band diagram under MPP operating condition shown in Figure 5.9. Here, the different splitting of the quasi-Fermi levels in the PVK and HIT sub-cells is well visible: the hole quasi-Fermi level bends in the base region so that the voltage of the top cell is not limited by the low gap of the HIT cell [60].

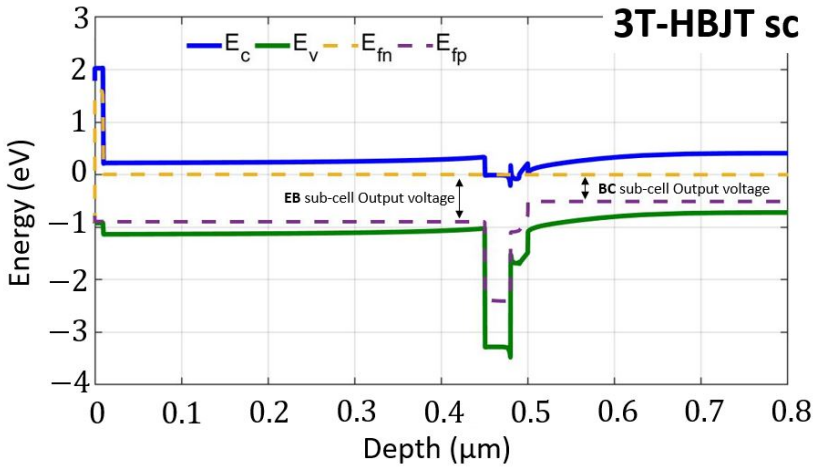

Fig. 5.9 Energy band diagram of the *p-n-p* 3T-HBT (Figure 5.2) with each junction biased at maximum power point. The dashed yellow and pink lines are the electron and hole quasi-Fermi levels, respectively.

In other words, there is no cross-talk between the two junctions, in line with the experimental findings in [60] for a 3T-HBT fabricated on III–V compound semiconductors. This demonstrates the robustness of the HBT solar cell architecture regardless of the particular material system.

Overall, our analysis of the 3T-HBT and DJ tandems, based on realistic material parameters and device model, shows that they attain comparable efficiency as expected according to more idealized detailed balance models [16]. The proof-of-concept devices in this work demonstrate an efficiency of 23% that can be further improved by design optimization as shown in the next section.

5.2 Fully textured HBT PVS tandem

The device discussed in the previous section can be further engineered by optimizing the PVS device design and using a different perovskite composition, that is $FA_{0.3}MA_{0.17}Pb(I_{0.83}Br_{0.17})_3$ because of its higher optical absorption [89]. Here, we propose a PVS 3T-HBT tandem developed starting from the fully textured monolithic perovskite/silicon 2T tandem solar cell reported by Sahli et al. [73]. Since the 3T-HBT under study exploits a textured surface, we have firstly validated the opto-electronic model discussed in Chapter 4 for textured solar cells, against the experimental data in [73]. Then, we have used the same model to analyze the potential performance of the proposed fully textured PVS 3T-HBT solar cell [68].

5.2.1 Model validation

The 2T DJ reference device [73] is shown in Figure 5.10. It consists of a PVK top cell and a silicon HTJ (HIT) bottom cell interconnected through a p^{++}/n^{++} c-Si tunnel junction. The conformal deposition of textured perovskite layers leads not only to a high compatibility with industrial silicon cells with front/rear textures, but also to improved light management [73, 90]. For the textured surface of Figure 5.10, we assume a regular inverted pyramidal texture with silicon characteristic base angle of 54.7° and height of 7μm [64]. Then, from the top, the 100 nm thick MgF_2 layer is the anti-reflection coating layer, and the 110 nm thick indium zinc oxide (IZO) layer acts as transparent front electrode [73]. The PVK sub-cell consists of: 10 nm SnO_2 layer [76, 77], 15 nm C_{60} [91] electron selective layer, 440 nm of photo-absorbing mixed perovskite layer [89, 75, 57] and 12 nm thick Spiro-TTB hole transport layer [76, 75]. The HIT sub-cell consists of 260 μm *n*-doped c-Si ($N_D = 2 \times 10^{15}$ cm^{-3}) [64] sandwiched by two thin-films of hydrogenated amorphous silicon: from the top (bottom) 5 (11) nm of *n*- (*p*-) doped a-Si:H [64] and 6 nm of intrinsic a-Si:H. The

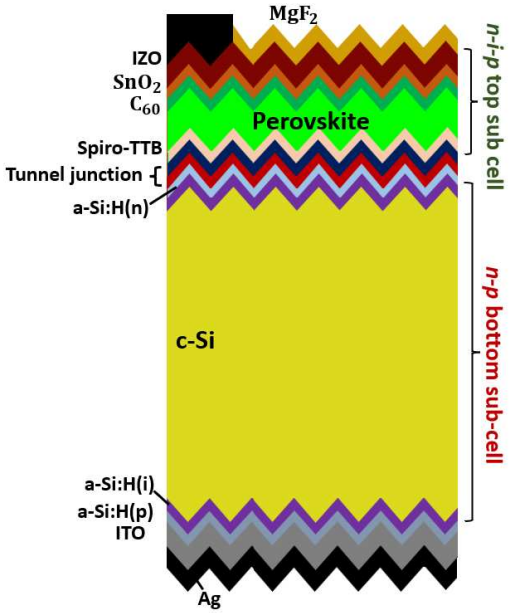

Fig. 5.10 Schematic view of the simulated fully textured 2T PVK/HIT-silicon tandem solar cell.

bottom cell is capped on its rear side by a 70 nm thick indium tin oxide (ITO) layer. The opto-electronic model used to simulate the PVS textured structure is discussed in Chapter 4. In summary, we have developed in TCAD Sentaurus an hybrid optical model which combines TMM and Monte Carlo RayTracing to asses both interference effects through the sub-wavelength multilayered media and scattering effects at the textured surfaces. Taking advantage of the assumed periodicity, optical simulations are done on the smallest symmetry element of the structure, i.e. a single pyramid unit. We assume normal incidence and an input optical power of 100 $\mathrm{mW/cm^2}$ (AM1.5G spectrum). Fig. 5.11 reports the wavelength-dependent complex refractive index for the optical simulation, while the main material parameters for the electrical simulation are summarized in Table 5.3.

As in the previous example, the perovskite material is modeled as a classical inorganic semiconductor [75, 85, 86]. The model includes Shockely-Read-Hall recombination in the c-Si substrate only, with e/h time constants of 1 ms; Auger recombination in silicon is modeled following [93] with C coefficient equal to 3.2×10^{-32} $\mathrm{cm^6\ s^{-1}}$. Finally, the radiative recombination coefficient is set to: 1.8×10^{-15} $\mathrm{cm^3/s}$ for a-Si:H ($\tau_{\mathrm{rad}}^{\mathrm{a\text{-}Si:H(n/p)}} = 55\ \mu\mathrm{s}$), 4.73×10^{-15} $\mathrm{cm^3/s}$ for c-Si ($\tau_{\mathrm{rad}}^{\mathrm{c\text{-}Si}} = 105$ ms), and 8×10^{-10} $\mathrm{cm^3/s}$ for all the materials of the PVK sub-cell ($\tau_{\mathrm{rad}}^{\mathrm{PVK}} = 6.2\ \mu\mathrm{s}$

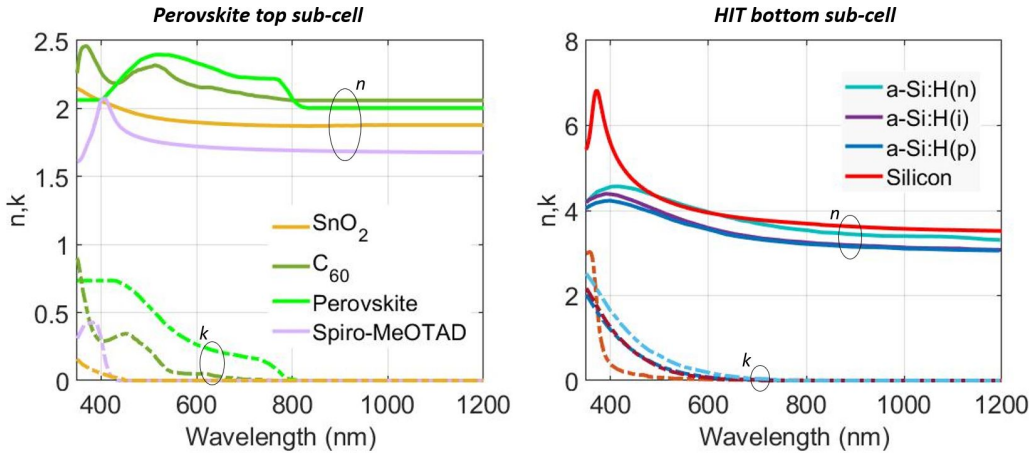

Fig. 5.11 Refractive index (n - solid line) and extinction coefficient (k - dashed line) of the materials forming the PVK and HIT sub-cells.

	PVK Top cell			HIT Bottom cell		
	Spiro-TTB	**Perovskite**	**SnO_2**	**C_{60}** [92]	**a-Si:H(n/p/i)** [64]	**c-Si** [61]
E_g [eV]	2.95 [76]	1.54 [76]	3.28 [76]	1.7	1.7	1.1
$q\chi$ [eV]	2.18	3.93	4.35	4.2	3.9	4.05
ε_r	3	6.5 [57]	9.6	4.1	11.9	11.9
N_c [cm^{-3}]	2.2×10^{18}	2×10^{18}	4.1×10^{18}	1.44×10^{21}	2.5×10^{20}	2.9×10^{19}
N_v [cm^{-3}]	1.8×10^{19}	2×10^{18}	4.1×10^{18}	1.44×10^{21}	2.5×10^{20}	1.8×10^{19}
$\mu^{[e]}$ [cm^2/Vs]	0.0002[75]	11.8 [75]	240 [77]	1.6	5/5/20	1417
$\mu^{[h]}$ [cm^2/Vs]	0.0002[75]	11.8 [75]	240 [77]	1.6	1/1/5	470
N [cm^{-3}]	-5×10^{18}	2×10^{14}	5×10^{18}	5×10^{18}	10^{19}/-10^{19}/10^{14}	2×10^{15}

Table 5.3 Main material parameters. E_g: bandgap; χ: electron affinity; ε_r: relative permittivity; $N_c(N_v)$: effective density of states in conduction (valence) band; μ: mobility; N: net doping; [e/h]: electron/hole; if not specified, the value shown applies to both carriers.

and $\tau_{\text{rad}}^{\text{ETL/HTL}} = 0.25$ ns). Among the various recombination mechanisms, the Auger one sets the upper limit of the BC open circuit voltage, by worsening it of ~ 20 mV with respect to the ideal case (radiative recombination only), for both 2T and 3T-HBT devices.

As first, we have simulated the External Quantum Efficiency (EQE) spectrum and the current-voltage ($J-V$) characteristics (Fig. 5.12) of the PVK/HIT-silicon tandem to validate the model against experimental data [73]. Simulated and experimental EQE spectra are in very good agreement. We attribute the slightly lower calculated

EQE of the HIT-silicon sub-cell with respect to the measured one to the fact that we have carried out 2D simulations of the triangular texture. Thus, the light trapping effect is underestimated. On the other hand, the mismatch in the PVK wavelength range could be attributed to some uncertainty in the material parameters, such as the extinction coefficient of the perovskite material which is heavily dependent on the composition of the perovskite [94]. The calculated short circuit current density (J_{sc})

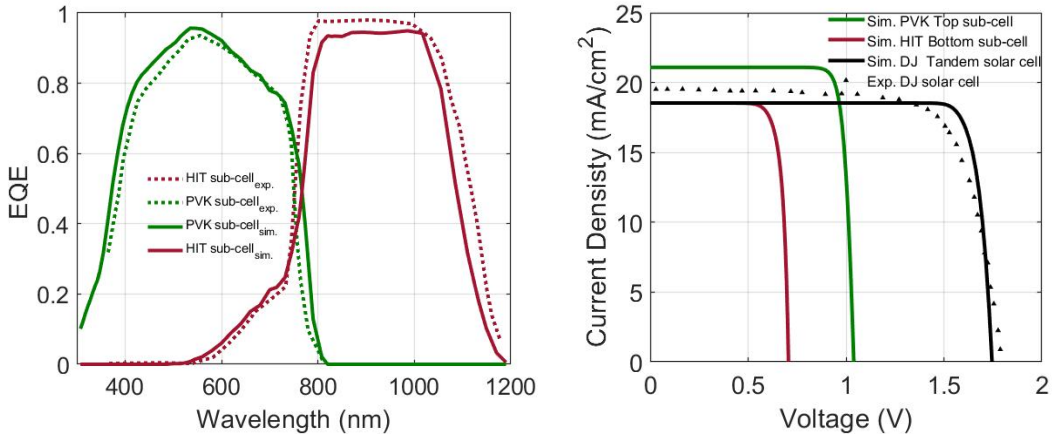

Fig. 5.12 Comparison between simulated (solid lines) and measured (dashed lines) EQE and $J-V$ characteristics of the fully-textured 2T PVK/Si tandem in [73].

for the PVK and HIT-silicon sub-cells results as 21.1 and 18.5 $\mathrm{mA/cm^2}$, respectively, against the measured ones of 20.1 and 20.3 $\mathrm{mA/cm^2}$. The calculated open circuit voltage (V_{oc}) of the standalone PVK and HIT cells results as ~ 1.04 V and ~ 0.71 V, respectively, well matched to the experimental values. The tandem cell reaches a total V_{oc} of ~ 1.75 V, about 30 mV lower than the measured one, and an estimated tandem efficiency of 28.1 % against 25.2 % of the experimental one. From the comparison in Fig. 5.12, it is apparent that the predicted fill factor (FF) is significantly higher than the measured one. This stems from the fact that the model neglects any enhanced recombination at the textured surfaces as well as defect assisted recombination in the thin film layers. Despite these slight discrepancies, the results show that the TCAD model provides a quite accurate picture of the experimental findings.

5.2.2 Simulation results

Once validated the opto-electronic model, we have studied the performance of the fully textured 3T-HBTsc depicted in Figure 5.13. The 3T-HBTsc consists of two sub-cells, i.e. the *n-i-p* emitter-base (EB) and the *p-n* base-collector (BC), that are electrically connected through the common base layer. In particular, the SnO_2, C_{60}, and PVK layers form the *n*-doped emitter region, the Spiro-TTB and *(p)-(i)* a-Si:H layers form the *p*-doped base region and finally the c-Si and *(i)-(n)* a-Si:H layers form the *n*-doped collector region. Fig. 5.13 shows the simulated EQE of the

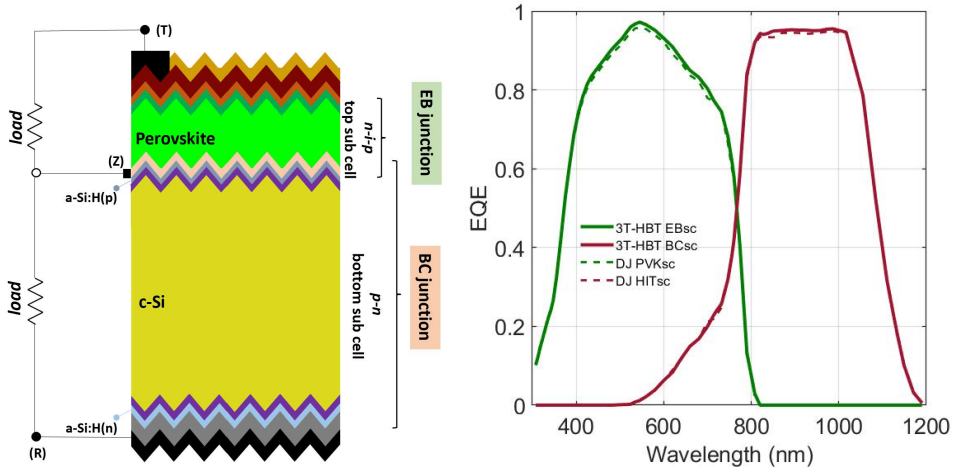

Fig. 5.13 Schematic view of the proposed fully textured PVK/HIT-silicon 3T-HBT solar cell. On the right, a comparison between simulated EQE of the fully-textured 3T-HBTsc (solid lines) and the 2T PVK/Si tandem (dashed lines).

3T-HBTsc in comparison to that one of the 2T DJ solar cell. The EQE of the HBT solar cell is almost identical to that one of the simulated DJ tandem, because the high diffusion length of the HIT cell ensures a high collection efficiency regardless of the illuminated side, and the PVK cell is unchanged.

Fig. 5.14a shows a contour map of the 3T-HBT tandem analyzing how the efficiency of the entire device changes as a function of the voltages V_{TZ} and V_{RZ}. We can observe that the MPP of the tandem corresponds to the MPP of the two individual sub-cells. This implies that current-voltage characteristic of the bottom BC cell is invariant with respect to the bias condition of the top EB cell (at least up to the maximum power point) and conversely for the EB cell with respect to the operating voltage of the BC one. Therefore, the individual J–V characteristics shown in Fig.

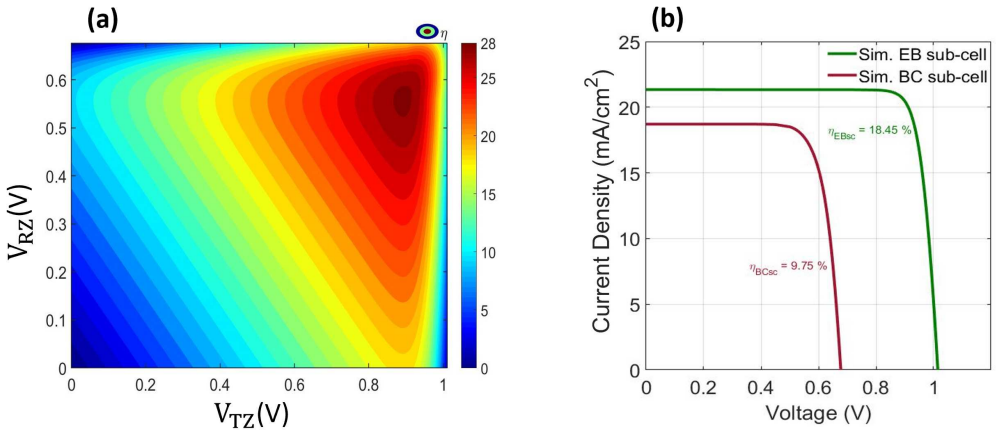

Fig. 5.14 (a) Efficiency as a function of the TZ and RZ voltages for the 3T-HBT tandem. (b) J–V characteristics of the fully textured 3T-HBT solar cell.

5.14b, are representative of the photovoltaic operation of the HBT tandem. The device achieves a total power conversion efficiency of $\sim 28.2\%$ with the two EB and BC sub-cells at maximum power point (0.89 V, 0.56 V), in line with the efficiency of the baseline 2T tandem.

In conclusion, the 3T-HBT textured device achieves an efficiency significantly higher than that one provided by the planar HBT proposed in Sec. 5.1. The main causes of the efficiency improvement are related to the textured design and to the different perovskite absorbing layer. In this regard, the PVK top sub-cell, characterized by a mixed perovskite material ($FA_{0.3}MA_{0.17}Pb(I_{0.83}Br_{0.17})_3$) [89], has an absorption coefficient higher than that one of the MAPI ($CH_3NH_3PbI_3$) material used in the planar device in Sec. 5.1, allowing for a higher EQE in the wavelength range [600 $\div$ 800] nm (Fig. 5.6). Also, the textured HBT exploits a *n-i-p* PVK architecture instead of the *p-i-n* one used in the planar HBT, thus minimizing optical loss. Finally, there is the effect of the textured surface that increases significantly the path length of the weakly absorbed long-wavelength photons (Sec. 2.1.2). In fact, by observing the EQE in Fig. 5.13 (of the textured HBTsc) and the one in Fig. 5.6 (of the planar HBTsc), one can notice that, exploiting a textured surface, the BC EQE improves at long wavelengths [900$\div$1200] nm. Moreover, we have also simulated the same HBT stack of Fig. 5.13, but with a flat surface verifying a current loss of 6.5% and 10.6%, in the EB and BC sub-cells of the planar cell, and a total efficiency loss of 4% with respect to the textured case.

The promising performance of the intrinsic 3T-HBT solar cell demonstrated in this chapter prompt for further studies to take into account the parasitic loss due to the current collecting grids of a realistic device layout. In particular, the implementation of the additional base contact and of the associated metal grid introduces shadow and resistive loss that affect the device performance and need to be carefully considered, as we will discuss in the next chapter.

Chapter 6

Impact of current collecting grids

Opto-electronic simulations of the intrinsic PVS 3T-HBT solar cell, carried out in Chapter 5, have shown that the efficiency of this architecture can compete with the series connected PVS tandem, exploiting a simpler structure because the top and bottom sub cells are seamlessly connected, without the need of any additional interconnecting layer. Thus, the HBT architecture has the potential for developing 3T PVS tandems compatible with cheap and widely used Si photovoltaic technologies such as PERC and HTJ. However, in contrast to 3T tandems based on interdigitated back contact silicon cells (Chapter 2), the three-terminal HBT requires the introduction of a third contact at the interface layer between the two sub-cells. The simplest solution to access the base layer is from the cell front side by implementing a grid layout with Top Interdigitated Contacts (TIC). However, the adoption of a top interdigitated grid for current collection provides additional optical and resistive losses affecting the device performance. In this chapter, with the aim to analyze the parasitic effect of a TIC grid layout, we present electro-optical simulations of the "intrinsic" 3T-HBT device combined with circuit-level simulations, accounting for shadow and resistive losses connected to the current collecting grids. Also, we analyze the impact of such losses on the scalability of the cell size.

6.1 TIC grid layout for HBT-based tandem

There are two solutions to access the base layer: from the cell front side by implementing a grid layout with top interdigitated contacts (TIC) (Figure 6.1a) or from the

back side by implementing a grid layout with bottom interdigitated contacts (BIC) (Figure 6.1b) [60].

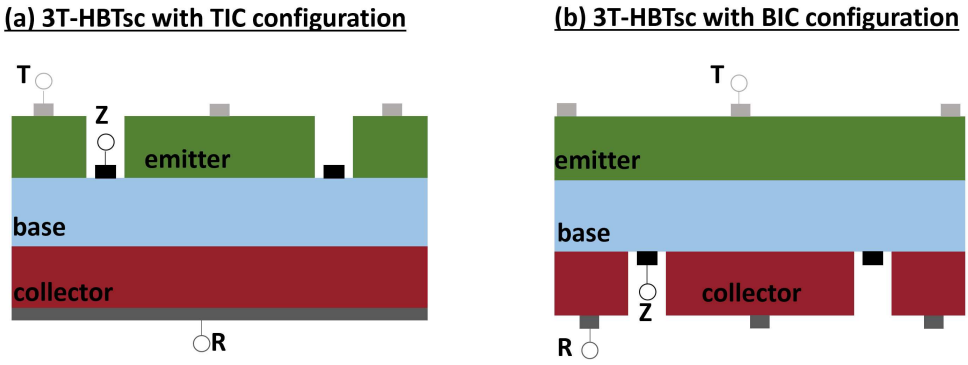

Fig. 6.1 Illustration of interdigitated contact scheme in which (a) the base is contacted from the top (TIC scheme) and (b) from the bottom (BIC scheme)

The BIC scheme has the advantage of minimizing the shading losses since, as shown in Figure 6.1b, only the emitter grid covers part of the front surface. However, the BIC configuration for a perovskite/silicon 3T-HBTsc is not the ideal solution because of fabrication complexity and manufacturing costs. Indeed a high amount of Si-substrate should be etched to contact the base layer from the bottom causing a lot of wasted material. Thus, the TIC scheme arises as the best candidate for PVS HBT solar cells. The TIC layout can be used for both textured *n-p-n* and flat *p-n-p* HBT devices made on HIT platform discussed in Chapter 5, placing the base metal contact on the a-Si:H or SnO_2 layer. However, as discussed in Chapter 2, the SHJ technology, by exploiting a-Si:H passivating layers on top and bottom of the c-Si absorbing layer, provides inefficient lateral charge transport with respect to PERC or BSF silicon cell. Thus, considering also the novelty of the device architecture, we decided to firstly evaluate the effect of the TIC architecture on a *p-n-p* 3T-HBT perovskite/silicon made on homojunction n^+/p Si bottom cell with the base contact placed on the *n*-Si layer, by ensuring a good lateral charge transport.
The PVS HBT tandem under study is shown in Fig. 6.2. It is made of a *n-i-p* PVK subcell on top of a planar homojunction n^+/p Si bottom cell. From the top, the TCO/PTAA/PVK layer stack constitutes the *p*-emitter layer; the SnO_2 electron transport layer (ETL) and *n*-Si one form the base layer on top of the thick *p*-type c-Si collector. As shown in Fig. 6.2a, the emitter contact is placed on the TCO layer, the base on the c-Si and a full-area contact is used at the collector. Under illumination, photogenerated carriers flow throughout the layers and are collected at the emitter,

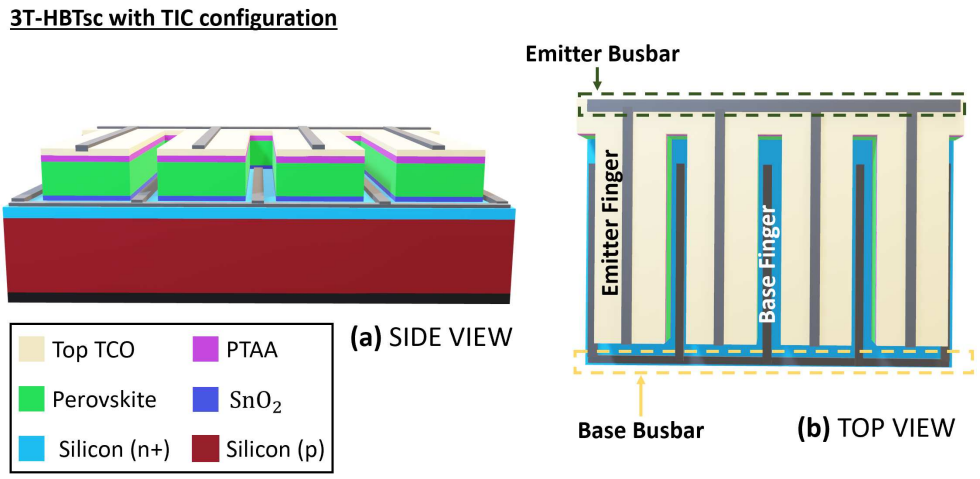

Fig. 6.2 3T-HBTsc with TIC configuration: (a) side view (b) top view.

base and collector terminals. Along the path, charge carriers cross materials with finite conductivity, interfaces and contacts causing power loss that can be modeled as resistive effects. As depicted in Fig. 6.3a, the current flow (black arrows) in the collector region is orthogonal to the R-metal contact that extends on the entire bottom surface; instead, in the emitter and base region, carriers laterally flow across the thin semiconductor layers until they reach the T and Z contacts. The metal grid (Figure 6.3c) introduces several losses mechanisms:

- resistance losses of the grid itself: fingers and busbars (see Figure. 6.3b);
- shading losses due to the area covered by metallic contacts;
- contact resistance between the metallic grid and the semiconductor layers;
- lateral resistance related to the current flow in the thin emitter and base regions.

Geometry and design optimization of the front-surface grid electrodes is needed to minimize the aforementioned energy losses [95], above all for large-area devices. For example, from Figure 6.3b, d_f is the distance between the base or emitter fingers, that is one of the main design parameter. Indeed, for high efficiency solar cell, it is mandatory to find out the best trade off for d_f, increasing or decreasing the number of the figers to minimize at the same time the lateral resistance and shading losses. To estimate power losses in the 3T-HBT solar cell under study, we have adopted a well-known approach based on a lumped description of the current collecting

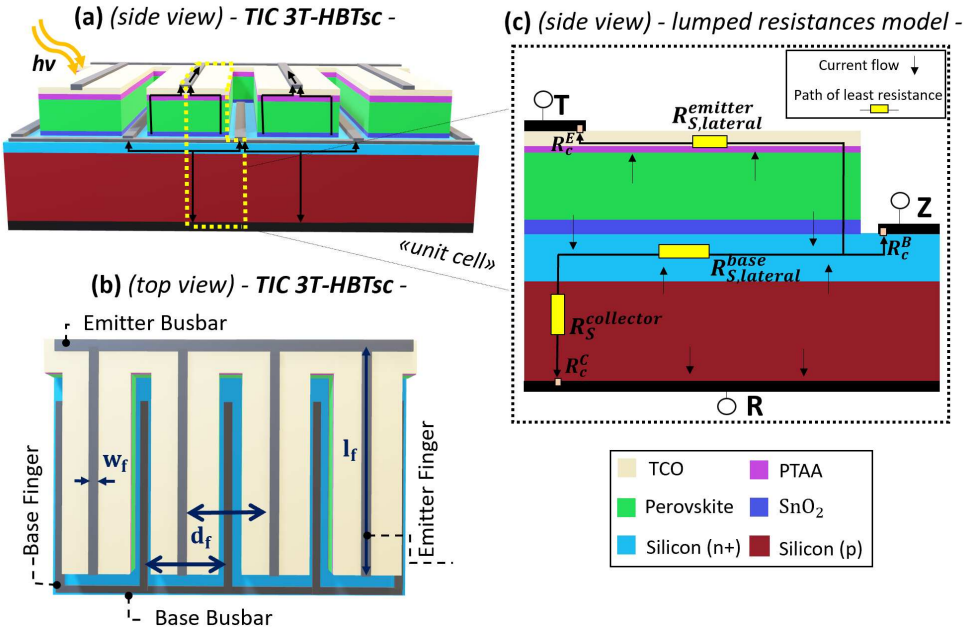

Fig. 6.3 3T-HBTsc with TIC configuration: (a) side view (b) top view. (c) Dashed black inset: unit cell of the 3T-HBT sc, in which yellow rectangles depict the lumped resistances.

grid [96]. We have considered a *unit cell* of the front metallic grid (yellow dashed box in Figure 6.3a) and modeled the distributed losses through equivalent lumped resistances [96]. In the 3T-HBT of Figure 6.3c, we can identify:

- R_c^E, R_c^B, R_c^C: contact resistances at the interface emitter/T-contact, base/Z-contact and collector/R-contact, respectively;
- $R_{S,lateral}^{emitter}$ and $R_{S,lateral}^{base}$ accounting for the contribution of lateral current flow;
- $R_S^{collector}$ accounting for the orthogonal current flow;
- R_{finger} accounting for series resistance of the metal fingers.

At this stage, the analysis does not include the busbars. Expressions for lateral, contact and finger resistances, respectively $R_{S,lateral}$, R_c and R_f, can be written as:

$$R_{\mathrm{S,lateral}} = \frac{1}{12} R_{\mathrm{sh}} d_{\mathrm{f}}^2 \tag{6.1a}$$

$$R_{\mathrm{c}} = \frac{1}{2} d_{\mathrm{f}} \frac{\rho_{\mathrm{c}}}{L_{\mathrm{t}}} \coth\left(\frac{w_{\mathrm{f}}}{2L_{\mathrm{t}}}\right) \tag{6.1b}$$

$$R_{\mathrm{f}} = \frac{1}{3} \frac{\rho_{\mathrm{m}}}{t_{\mathrm{f}} w_{\mathrm{f}}} l_{\mathrm{f}}^2 d_{\mathrm{f}} \tag{6.1c}$$

Derivation of Eq. 6.1a and Eq. 6.1c are reported in Appendix D. For Eq. 6.1b, see [96].

From Figure 6.3c, we can identify three equivalent lumped series resistances R_E, R_B and R_C (in $\Omega\mathrm{cm}^2$) that can be read as

$$R_{\mathrm{E}} = R^{\mathrm{E}}_{\mathrm{S,lateral}} + R^{\mathrm{E}}_{\mathrm{c}} + R^{\mathrm{E}}_{\mathrm{f}} \tag{6.2a}$$

$$R_{\mathrm{B}} = R^{\mathrm{B}}_{\mathrm{S,lateral}} + R^{\mathrm{B}}_{\mathrm{c}} + R^{\mathrm{B}}_{\mathrm{f}} \tag{6.2b}$$

$$R_{\mathrm{C}} = \rho_{p\text{-Si}} t_{\mathrm{collector}} \tag{6.2c}$$

The resulting equivalent circuit model of the 3T-HBT is shown in Fig. 6.4.

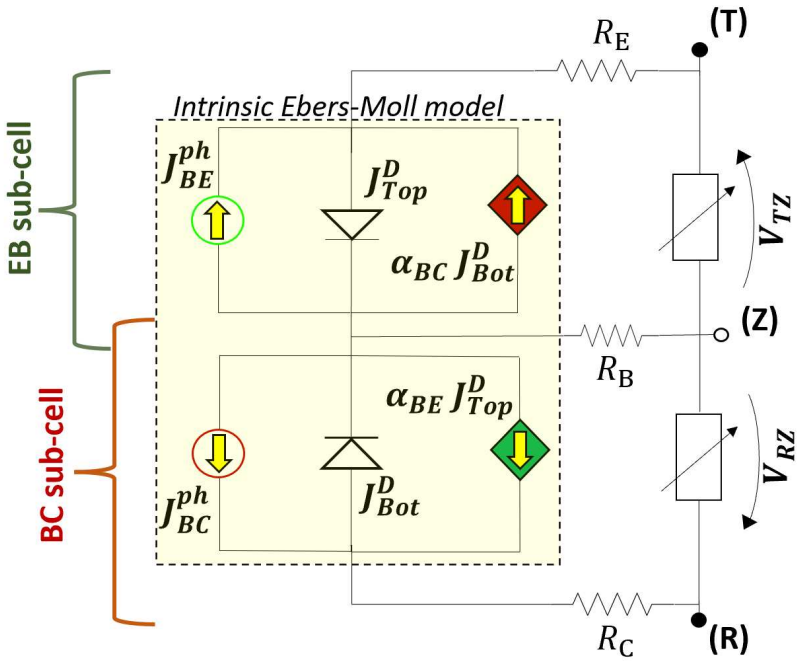

Fig. 6.4 Equivalent circuit of the 3T-HBT tandem.

It consists of the Ebers-Moll circuit of the *intrinsic* device under illumination [43, 16] completed by parasitic series resistances at each terminal. The parameters of the Ebers-Moll model (dashed box in Fig. 6.4) are extracted by fitting the current-voltage characteristics of the intrinsic 3T-HBT obtained by coupled optical-transport simulations.

6.1.1 Focus on the base resistance

From Fig. 6.4, one can observe that the effect of the parasitic resistances R_{E} and R_{C}, on the sub-cell performance, is the same of the series resistance in a SJ solar cell discussed in Chapter 2. Instead, it is interesting to discuss the effect of the base resistance R_{B}, that is shared between the emitter-base and base-collector sub-cells. To this aim, we can neglect, for the time being, in Fig. 6.4 the parasitic resistances R_{E} and R_{C}, obtaining the simplified circuit of Fig. 6.5.

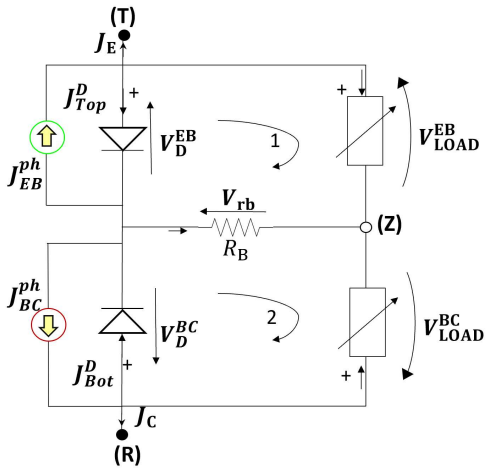

Fig. 6.5 Simplified equivalent circuit model of the 3T-HBT, highlighting the impact of the $\mathrm{R_B}$ resistance.

From the analysis of the circuit in Fig. 6.5, we derive the following system of equations:

$$V^{\mathrm{EB}}_{\mathrm{LOAD}} = V^{\mathrm{EB}}_{\mathrm{D}} + V_{\mathrm{rb}} \tag{6.3a}$$

$$V^{\mathrm{BC}}_{\mathrm{LOAD}} = V^{\mathrm{BC}}_{\mathrm{D}} + V_{\mathrm{rb}} \tag{6.3b}$$

where V_{rb} is the base resistor voltage, V_D the diode voltage and V_{LOAD} the external load voltage. When $R_B = 0$, we obtain the *intrinsic* Ebers-Moll model, with $V_{LOAD} = V_D$. Otherwise, from Eq. 6.3, the voltage generated at the EB/BC external load differs from the EB/BC diode voltage of an amount equal to the voltage drop V_{rb} on the resistor R_B.
From the equivalent circuit model of Fig. 6.5, V_{rb} can be written as

$$V_{rb} = (-J_{PH}^{EB} + J_D^{EB})R_B + (-J_{PH}^{BC} + J_D^{BC})R_B \tag{6.4}$$

By substituting Eq. 6.4 into Eq. 6.3a and Eq. 6.3b, we have:

$$V_{LOAD}^{EB} = V_D^{EB} + (-J_{PH}^{EB} + J_D^{EB})R_B + (-J_{PH}^{BC} + J_D^{BC})R_B \tag{6.5a}$$
$$V_{LOAD}^{BC} = V_D^{BC} + (-J_{PH}^{EB} + J_D^{EB})R_B + (-J_{PH}^{BC} + J_D^{BC})R_B \tag{6.5b}$$

Eq. 6.5 demonstrates that, due to the presence of R_B, the working point of the EB (BC) sub-cell depends on the working point of the BC (EB) sub-cell. In other words, there is a R_B mediated cross-talk between the sub-cells [97].
In this regard, let us consider the EB top sub-cell, and short-circuit the bottom BC sub-cell ($V_{LOAD}^{BC} = 0$). Under this condition, both EB and BC currents, $-J_{PH}^{EB} + J_D^{EB}$ and $-J_{PH}^{BC} + J_D^{BC}$ respectively, flow through the base resistor by producing a voltage drop (V_{rb}, Eq. 6.4) that affects the *J-V* curve of the EB junction, by worsening its maximum power point.
Otherwise, when the BC junction's operating point moves from short-circuit to open-circuit ($J_{PH}^{BC} = J_D^{BC}$), the voltage drop on the resistor R_B decreases to $(-J_{PH}^{EB} + J_D^{EB})R_B$ by improving the EB *J-V* curve. In detail, the base resistance acts decreasing the open circuit voltage of each junction when the other move from the open circuit to the short circuit condition. This effect has been observed experimentally in [98], where the voltage drop caused by R_B in either junction, when the other junction goes from open circuit to short circuit, was reported to be $\approx$20 mV.
Thus, it is important to assess the effect of the base resistance, since it could significantly worsen the efficiency of the 3T-HBT device.

6.2 Simulation approach & results

Fig. 6.6 presents the simulation strategy implemented to study the effect of the grid layout on the photovoltaic performance.

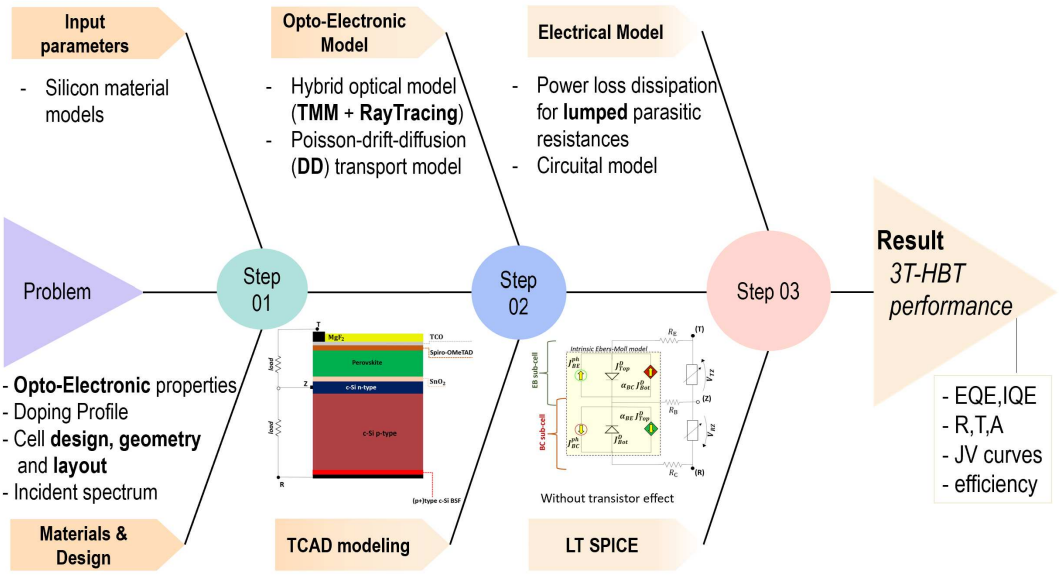

Fig. 6.6 Flow diagram of physics-based and circuit-level simulations.

Firstly, opto-electronic simulations of the PVS 3T-HBT are carried out in TCAD Sentaurus without taking into account lateral transport neither grid shading and resistive loss. Then, parameters of the Ebers-Moll model are extracted by fitting the current–voltage characteristics of the *intrinsic* 3T-HBT. Finally, the effect of the parasitic resistances on the 3T-HBT performance is evaluated through circuit level simulations [99].

6.2.1 Intrinsic device performance

In Fig. 6.7a, the PVK sub-cell consists of: 34 nm TCO layer, 11 nm PTAA hole selective layer, 480 nm of perovskite layer and 25 nm of the SnO_2 electron transport layer. Then, the Si homo-junction bottom sub-cell consists of 150 nm of *n*-Si and 150μm thick *p*-type c-Si. The cell architecture is completed by a 92 nm thick MgF antireflection coating.

Optical-electrical simulations of the PVS 3T-HBT solar cell of Fig. 6.7a were

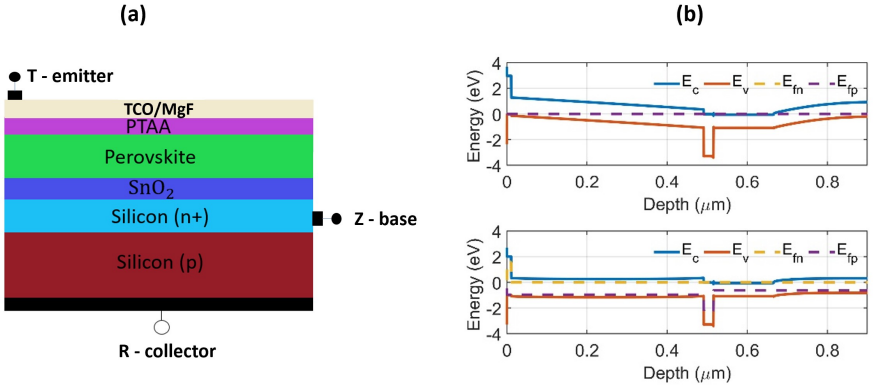

Fig. 6.7 3T-HBT PVS tandem: schematic view (a) Energy band diagram at short-circuit and maximum power point (b).

carried out based on the same simulation methodology followed also in Sec. 5.1. Material parameters for the electrical simulation are reported in Table 5.3. The main differences with respect to the planar HBT of Sec. 5.1, rely on the *p-i-n* architecture of the PVK top sub-cell and on the fact that a homo-junction bottom sub-cell replaces the HIT one. Fig. 6.7b shows the energy band diagram at short-circuit and maximum power point for the 3T-HBT solar cell of Fig. 6.7a. The PVK and Si sub-cells reach a Voc of 1.06 and 0.64, respectively.

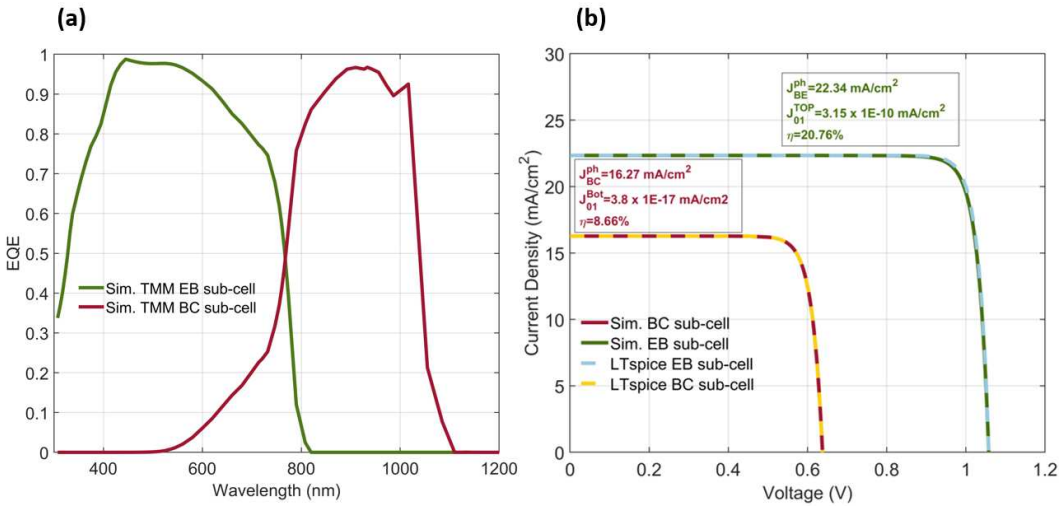

Fig. 6.8 (a) EQE and (b) J–V characteristics obtained from TCAD simulations (solid lines) and Ebers-Moll circuit fit (dashed lines).

Fig. 6.8a shows the EQE of the 3T-HBT PVS tandem under study; it is possible to observe a penalty at long wavelength related to the high surface recombination at the

back side of the BC junction. We have used a (p^+)-Si as BSF. A possible solution to reduce rear surface recombination is by exploiting a PERC architecture (discussed in Chapter 2) by reducing the metal contact area and passivating the surface between the metal contact and Si material. Fig. 6.8b shows the J–V characteristics of the EB and BC sub-cells of the 3T-HBT PVS tandem, and the J–V characteristics reproduced with the *intrinsic* Ebers-Moll model (yellow box in Fig. 6.4). The Ebers-Moll parameters have been obtained by neglecting the current controlled generators of Fig. 6.4 for both junctions, because transport simulations of the *intrinsic* 3T-HBT have shown that the two sub-cells substantially work as independent, *i.e.* no appreciable transistor effect occurs through the SnO_2/n^+-Si base. Fitting parameters are reported as inset in Fig. 6.8b. The *intrinsic* device has a high efficiency of $\sim 29.4\%$.

6.2.2 Circuit-level simulations: results and discussion

To analyze the influence of the TIC grid on the device performance and the scalability to large areas, we have considered typical metal grid parameters [95, 96], as summarized in Table 6.1.

Table 6.1 Grid geometrical and material parameters

Parameter	Label	Value
Finger width (μm)	w_f	40
Finger height (μm)	t_f	15
Contact resistivity (Ag/ITO) (mΩ cm^2)	ρ_c	1.27
Contact resistivity (Ag/Si) (mΩ cm^2)	ρ_c	1
Gridline resistivity (Ω cm)	ρ_m	2.65×10^{-6}
ITO resistivity (Ω cm)	ρ_{ITO}	9.31x 10^{-4}
c-Si(n^+) resistivity (Ω cm)	ρ_{Si}	1.11 x 10^{-3}
SnO_2 resistivity (Ω cm)	ρ_{SnO_2}	5.2 x 10^{-3}
a-Si:H(n) resistivity (Ω cm)	$\rho_{a\text{-}Si:H(n)}$	124 x 10^{-3}

The effective sheet resistance of the emitter (TCO/PTAA/PVK) and base (SnO_2/n-Si) stacks is calculated by a simple parallel connection of the equivalent resistances

of the constituting layers [96], as shown in Eq. 6.6:

$$R_{\text{tot,sh}}^{\text{Emitter}} = \left(\frac{1}{R_{\text{sh}}^{\text{ITO}}} + \frac{1}{R_{\text{sh}}^{\text{HTL}}} + \frac{1}{R_{\text{sh}}^{\text{PVK}}} \right)^{-1} \tag{6.6a}$$

$$R_{\text{tot,sh}}^{\text{Base}} = \left(\frac{1}{R_{\text{sh}}^{\text{SnO}_2}} + \frac{1}{R_{\text{sh}}^{\text{c-Si(n}^+\text{)}}} \right)^{-1} \tag{6.6b}$$

$R_{\text{tot,sh}}^{\text{Emitter}}$ and $R_{\text{tot,sh}}^{\text{Base}}$ result equal to $274\,\Omega/\square$ ($\approx R_{\text{sh}}^{\text{ITO}}$) and $74\,\Omega/\square$ ($\approx R_{\text{sh}}^{\text{c-Si(n}^+\text{)}}$), respectively. $R_{\text{tot,sh}}^{\text{Emitter/Base}}$ is affected by the properties of the material forming the emitter/base region. Fig. 6.9a shows the corresponding emitter (R_{E}) and base (R_{B})

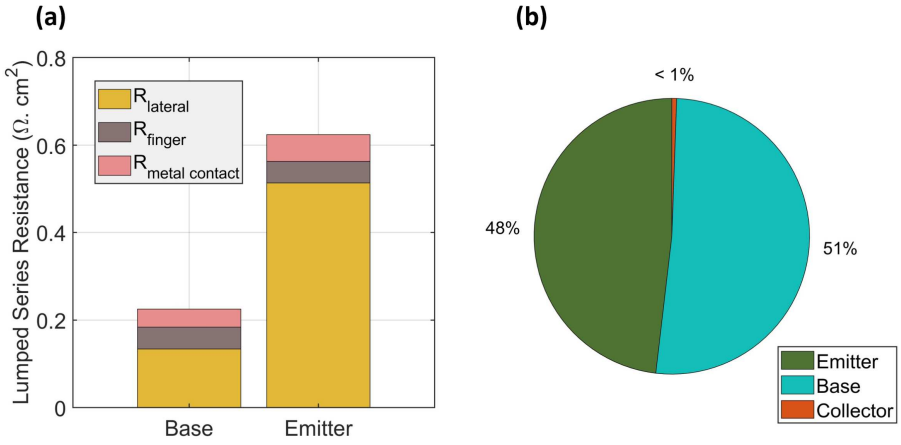

Fig. 6.9 (a) Emitter and base resistance components for a PVS 3T-HBT tandem with 1.5 cm x 1.5 cm area and (b) associated fractional resistive power loss.

resistance, computed according to Eq. 6.2, for a finger length of 1.5 cm and finger distance of 1.5 mm. Here, the dominant resistive path is associated to the lateral transport (R_{lateral}) across the base and emitter, as depicted by the yellow rectangle in Fig. 6.9a. Instead, both finger R_{finger} and contact $R_{\text{metal contact}}$ resistances are marginal. As the cell area and finger length increase, the resistive effects of the emitter/base grid become the dominant cause of efficiency loss. Fig. 6.9b shows the power loss associated to the TIC configuration under study. Although the total base resistance R_{B} is about 1/3 of the emitter one R_{E} (Fig. 6.9a), the fractional power loss ($\propto RJ^2$) associated to base and emitter grids is comparable ($\approx 48\%$ emitter vs $\approx 51\%$ base) because the current through the base, which corresponds to the sum of the top and bottom sub-cell currents, is about 70% higher than that one of the emitter.
As previously discussed in 6.1.1, the presence of the parasitic resistance R_{B} provides

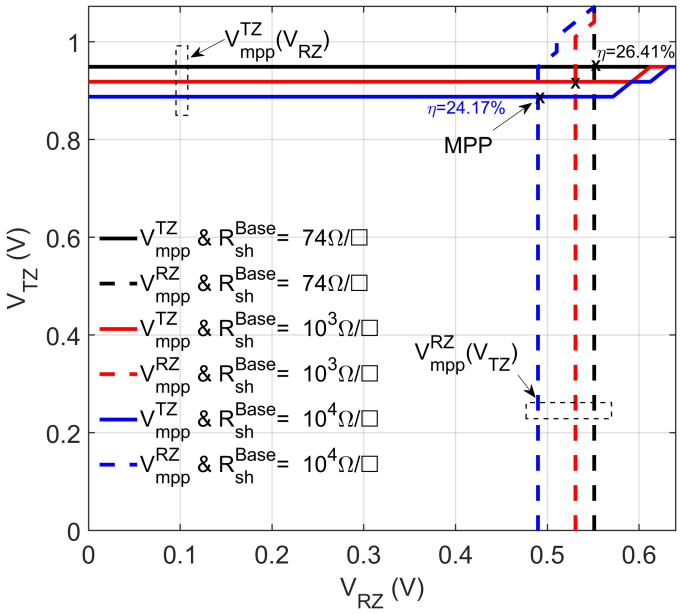

Fig. 6.10 EB and BC mpp voltages (V^{TZ}_{mpp} and V^{RZ}_{mpp}) as a function of V_{RZ} and V_{TZ} voltages.

an interplay between the EB and BC sub-cells, therefore the MPP of each sub-cell depends on the working point of the other. In this regard, Fig. 6.10 analyzes the impact on the MPP voltages of the interaction between the two sub-cells and the corresponding efficiency reduction for a small-area 3T-HBT device, with finger spacing and length of 1.5 mm and 1.5 cm, for several values of R^{Base}_{sh}. For the sake of the following discussion, R^{Base}_{sh} identifies the sheet resistance of that layer where the base metal contact is physically placed. In Eq. 6.6b, we have replaced $R^{c\text{-}Si(n^+)}_{sh}$ with R^{Base}_{sh} ranging in $[1 \div 5\times10^4]$ Ω/□.

In Fig. 6.10, it can be observed for several values of R^{Base}_{sh}, the variation of the EB (BC) maximum power point (MPP) voltage V^{TZ}_{mpp} (V^{RZ}_{mpp}) as a function of the V_{RZ} (V_{TZ}). One can observe that the two sub-cells remain independent up to the MPP, regardless of the value of R_B. The R_B mediated cross-talk is visible only at voltages higher than the MPP one and causes an increase of the open circuit voltage as the bias of the other sub-cell grows towards open circuit. On the other hand, for each sub-cell, Vmpp becomes smaller as R_B increases, because of the series resistance effect on the individual cell.

The introduction of a TIC configuration causes not only resistive effects and an interplay between the two sub-cells, as discussed above, but also shading losses due to the area covered by metallic contacts. These must be also quantified in order to

assess the overall efficiency losses provided by the TIC configuration. In the shaded regions, as shown in Fig. 6.11, the incoming light is blocked and does not contribute to the photo-current, hence these areas can be treated as "dead".

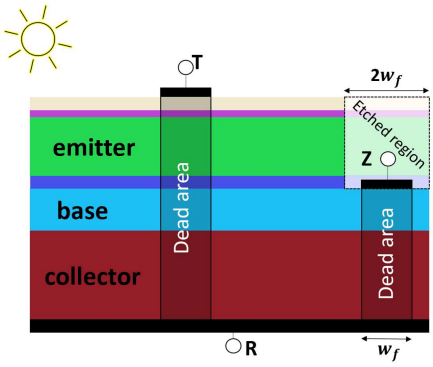

Fig. 6.11 Sketch of optical losses due to the TIC configuration.

The power loss generation associated to them is taken into account by applying a shading loss factor, f_{shadow}, given as [95]

$$f_{\text{shadow}} = \frac{w_{\text{f}}}{d_{\text{f}}} \tag{6.7}$$

where w_{f} is the grid width.
By using the TIC grid, part of the emitter must be etched to contact the base layer and, depending on the metal deposition technique, the *effective* finger width could have a high thickness variation. To date, some works, focused on metallization route to realize large area perovskite/Si tandems, report finger resolution widths of 16 ± 1 μm for ink-jet printing [95] or 23 ± 4 μm for screen printing technique [100].
In this preliminary study, we have assumed an etched region width equal to twice the metal finger width. Hence, to account for shadow losses, we have considered the lost EB current ($J_{\text{BE}}^{\text{ph}}$ in Fig. 6.4) equal to three times f_{shadow}, because of the emitter finger and the emitter etched region (Eq. 6.8). Alongside, we have evaluated the fraction of lost BC current ($J_{\text{BC}}^{\text{ph}}$ in Fig. 6.4) equal to twice f_{shadow}, accounting for the emitter and base finger metallization (Eq. 6.9).

$$J_{\text{BE}}^{\text{ph'}} = J_{\text{BE}}^{\text{ph}}\,(1 - 3w_{\text{f}}/d_{\text{f}}) \tag{6.8}$$

$$J_{\text{BC}}^{\text{ph'}} = J_{\text{BC}}^{\text{ph}}\,(1 - 2w_{\text{f}}/d_{\text{f}}) \tag{6.9}$$

Results reported in Fig. 6.12 show the efficiency loss of the PVS 3T-HBTsc in terms of finger spacing d_f and base sheet resistance R_{sh}^{Base} for small devices ($l_f = 1.5$ cm). The variation of R_{sh}^{Base} on the y-axis of the map corresponds to a change in the conductivity of the base materials. As shown in Fig. 6.12, for R_{sh}^{Base} up to

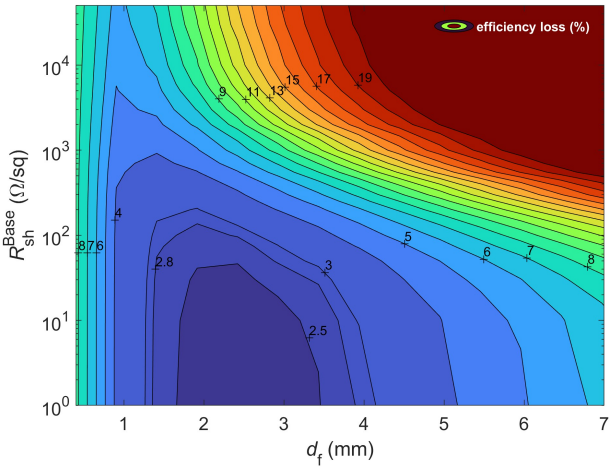

Fig. 6.12 Efficiency loss as a function of the finger distance (d_f) and base sheet resistance (R_{sh}^{Base}).

$100\,\Omega/\square$ (representative of PVS tandems on homojunction c-Si cells as in Fig.6.2) the efficiency loss can be minimized to less than 3% with finger distance in the range $[1.5 \div 2.9]$ mm. For very low finger distance (≈ 0.5 mm), the dominant effect limiting the efficiency is related to the shadowing effect. Based on the previous considerations, the base resistance R_B is strongly dependent on the HBT configuration (*p-n-p* or *n-p-n*) and bottom cell technology. Thus, it is interesting to evaluate the base resistance for a PVS 3T-HBT solar cell made on HTJ silicon cells. In this regard, Fig. 6.13a and Fig. 6.13b show an analysis for *n-p-n* and *p-n-p* perovskite/silicon heterojunction 3T-HBT configurations, respectively. Based on the lumped analytical model, the base resistance R_B accounts for the high sheet resistance of both a-Si:H layers ($\approx 10^5\,\Omega/\square$, Tab. 6.1) and HTL/ETL layers, depending on the used *n-p-n*/*p-n-p* configuration. We can observe that the total base series resistance of the *n-p-n* device (Fig. 6.13a) is higher than the corresponding one of the *p-n-p* configuration (Fig. 6.13b). In fact, in the *n-p-n* configuration, the total series resistance is dominated by the high lateral resistance of the HTL/a-Si:H stack, which is characterized by the high sheet resistance of $\approx 10^5\,\Omega/\square$ of the a-Si:H layer. Instead, in the *p-n-p* configuration, the lateral base resistance is mitigated by the presence of the highly conductive SnO_2

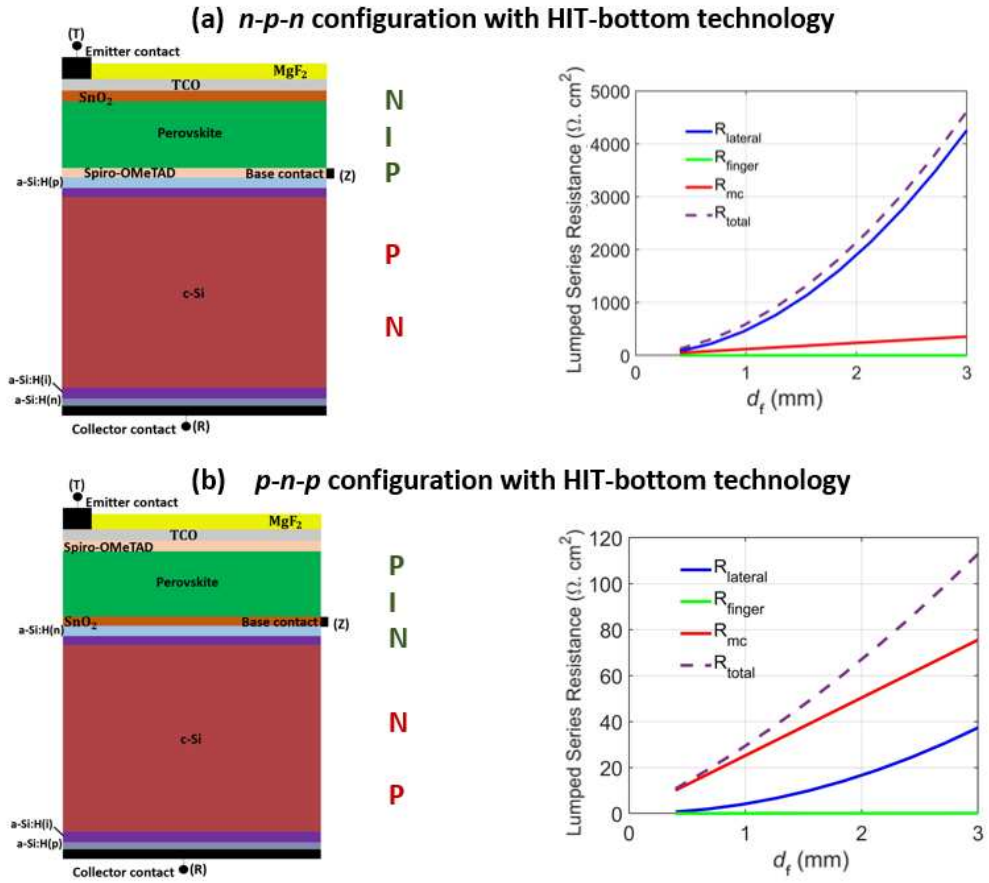

Fig. 6.13 3T-HBT solar cell made on HTJ silicon bottom cell: (a) *n-p-n* configuration (b) *p-n-p* configuration and related base resistance components. The plots show the lumped base series resistance contributions as in function of d_f. R_{mc} (Eq. 6.1b) is the contact resistance at the interface Base/Z-contact, $R_{lateral}$ (Eq. 6.1a) accounts for the contribution of the base lateral current flow, R_{finger} (Eq. 6.1c) for the metal finger resistance and R_{total} is the sum of all contributions.

electron transport layer, with sheet resistance $\approx 10^3\,\Omega/\square$ (Tab. 6.1). In this case, the total series resistance is dominated by the contact resistance of the interface Ag/SnO_2. In this regard, the contact resistivity Ag/SnO_2 as well as Ag/a-Si:H is set to $\approx 1\,\Omega cm^2$ [101–103]. In contrast, in the HBT made on homo-junction silicon bottom cell, the contact resistance is expected to be very low owing to the small contact resistivity of Ag/Si (Table 6.1). Thus, to achieve low efficiency loss (Fig. 6.12) for PVS 3T-HBT tandems on HTJ silicon cells, the high sheet resistance of the a-Si:H layers shall be mitigated by exploiting a highly conductive transport layer for the PVK top cell, such as the SnO_2 layer used in the *p-n-p* HBT under study. On the other hand, we have analyzed in Sec. 5.1 that the choice of a *p-i-n* top sub-cell,

illuminated from the HTL layer, leads to higher optical losses. Thus, it is important to pursue a trade off between optical and resistance losses, even considering other HTL materials.

Finally, we study the impact of the metal grid layout for different values of finger length l_{f} and distance d_{f}. To this aim, we consider two values for the base sheet resistance: $R_{\mathrm{sh}}^{\mathrm{Base}} = 74\ \Omega/\square$ and $R_{\mathrm{sh}}^{\mathrm{Base}} = 10^5\ \Omega/\square$ representative of 3T-HBT tandems made on homo-junction and hetero-junction silicon cells, respectively. In detail, in

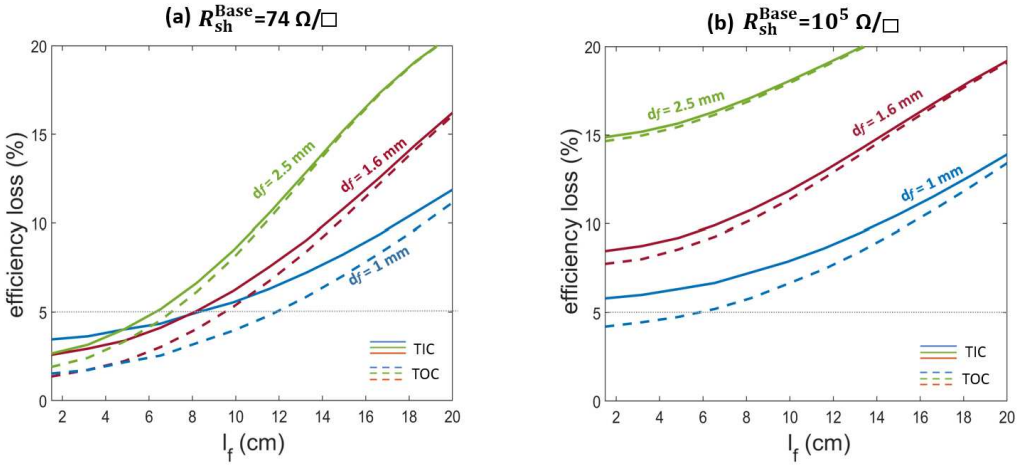

Fig. 6.14 Efficiency loss as a function of finger finger length (l_{f}) for the case studies of PVS 3T/HBT on (a) homojunction Si cell ($R_{\mathrm{sh}}^{Base} = 74\ \Omega/\square$) and (b) HTJ Si cell ($R_{\mathrm{sh}}^{Base} = 10^5\ \Omega/\square$): TIC layout (solid line) and TOC layout (dashed line).

Fig. 6.14a and Fig. 6.14b, we analyze the efficiency penalty for a TIC layout (solid lines) when scaling to larger areas, i.e. increasing both finger length and distance. Clearly, the base resistance R_{sh}^{Base} is, the HBT device worsens its performances as the finger length or distance increases. The impact of l_{f} has a large effect on the efficiency, since the finger resistance scales with the square of l_{f} (Eq. 6.1c). Simulations of Fig. 6.14a show that for architectures based on homojunction silicon bottom cell, with an optimized TIC layout, efficiency loss remain lower than 5% (green dashed line) for finger lengths up to 6 cm. Instead, by exploiting the HTJ Si cell, the efficiency losses, for the design and material parameters under investigation, are greater than 5 % (Fig. 6.14b) due to the high base sheet resistance.

Aiming at improve the device performance, one could investigate an alternative solution to the TIC configuration, that is a layout with emitter/base Top Overlapped Contacts (TOC) inspired to microelectronic metal interconnection technology. In this case, by overlapping emitter and base metal contact, we will have an important

reduction of the optical losses. In this regard, the EB and BC fraction of lost current of Eq. 6.8 and Eq. 6.9 can be rewritten as

$$J_{\mathrm{BE/BC}}^{\mathrm{ph'}} = J_{\mathrm{BE/BC}}^{\mathrm{ph}} (1 - w_{\mathrm{f}}/d_{\mathrm{f}}) \tag{6.10}$$

The TOC configuration improves the HBT performance by reducing the optical losses. Indeed, in Fig. 6.14, we can observe the effect of the TOC grid (dashed lines) with respect to the TIC (solid lines) one. The TOC layout provides lower efficiency losses mainly for small finger distance, when the dominant loss effect is related to the shadowing one. Instead, as the finger distance increases, the efficiency loss of the TOC layout approaches that one of the TIC one, being dominated by resistive effects. For the HBT made on HTJ Si cell, although we exploit a TOC layout, efficiency losses, shown in Fig. 6.14b, remain quite high for $d_{\mathrm{f}} > 1$ mm. On the other hand, by further reducing the finger distance, efficiency loss can be significantly reduced. For example, we calculated that for d_{f}=0.5 mm the penalty decreases to about 3.3% when l_{f}=1.5 cm and remains lower than 5% for l_{f} up to 12 cm.

Overall, the obtained results show the potential of using the HBT architecture to develop high efficiency, large area three-terminal perovskite/silicon tandems that can be integrated with industry standard silicon bottom cells.

In the perspective of scaling up to large areas, further study is needed to refine the model, e.g. by including busbars power loss, and to optimize material and device structure/layout.

Chapter 7

Conclusions

This work has presented a modeling and simulation study of perovskite/silicon 3T-tandems based on the HBT solar cell concept, to investigate their potential and possible bottlenecks compared to conventional 2T series connected tandems.
The detailed balance analysis of both PVS 2T and 3T solar cells shows that the 3T-HBT structure removes the current matching constraint that affects 2T tandems, allowing for a wide range of band gap combinations for the perovskite top sub-cell and the realization of a simpler tandem structure, without the need of using any tunnel junction or recombination layer.
In Chapter 3, the operating principle of the HBT tandem has been outlined with the aid of a generalized formulation of the analytical Hovel model. Compared with other semi-analytical approaches reported in the literature, the model in this thesis allows the formulation of closed-form analytical expressions for the HBT tandem terminal currents, clarifying the impact of different physical parameters on photovoltaic performance. Moreover, it naturally leads to the definition of the equivalent electrical circuit of the HBT solar cell, which is an extension of the Ebers-Moll model of bipolar transistors under illumination.
Based on the analytical model, we could verify that the reduction of the attainable efficiency caused by the interplay between the two sub-cells, mediated by the common base layer, is rather limited and can be made negligible by a proper design. In fact, because of the high/low gap stacking of emitter/base and base/collector junctions, and the requirement of a highly conductive base, the HBT tandem is characterized by a weak transistor action *by design*.
A preliminary PVS 3T-HBT solar cells design is developed, demonstrating the ab-

sence of any significant transistor effect under maximum power point operation. Thus, the total HBTsc efficiency corresponds to the sum of the efficiency of the individual sub-cells operating as independent. Finally, the analysis demonstrates a visible transistor action, showing up an apparent increase of the short circuit current at the bottom sub-cell, when the top sub-cell increases towards its open circuit. This effect has been observed experimentally in HBT tandems based on III-V semiconductors and attributed to photoluminescence coupling between the sub-cells. Our results show that the transistor action could be a concurrent cause of such an effect. In this regard, further theoretical and experimental study is needed to clarify the relative impact of the two mechanisms.

The extension of the Hovel model to the HBT case provides the preliminary knowledge needed to get critical insight from more advanced numerical simulations exploited in the following chapters for the accurate modeling and design of proof-of-concept devices close to the practical realization. In this perspective, coupled electromagnetic and drift-diffusion simulations of both planar and textured PVS 3T-HBT tandems based on homo-junction or HTJ Si bottom sub-cell are carried out by means of the Synopsys TCAD software. Among different aspects, the most relevant improvement of the numerical model, with respect to the analytical one, is the ability to accurately model the external quantum efficiency of the device by resorting to mixed coherent/incoherent propagation methods, depending on the structure under study. In particular, Transfer Matrix Method combined with Monte Carlo Ray Tracing method has been used, as described in Chapter 4.

Chapter 5 presents two proof-of-concept *p-n-p* and *n-p-n* designs of HBT cells, developed within a HIT-Si platform, with flat and textured surfaces. By simulating the *p-n-p* PVS 3T-HBT structure, to investigate its potential with respect to *n-p-n* DJ cell counterpart, we found out that the use of a *n-i-p* top sub-cell architecture rather than a *p-i-n* one, that is by illuminating the cell from the ETL layer, improves the optical response. However, adopting a *n-i-p* architecture for the top sub-cell can worsen the electrical performance of the HBT tandem made on HTJ silicon bottom cell due to lateral transport in the base layer. In this regard, a different HBT architecture based on PERC or BSF Si cell can relax the electrical constraints on the *n-p-n* or *p-n-p* configuration to be adopted. Nevertheless, the penalty in the HBT EQE with respect to the DJ one does not affect the tandem efficiency, because the short circuit current of the DJ tandem is limited by the top cell due to the current matching constraint. As a result, the two devices deliver comparable power.

In the second part of Chapter 5, we have proposed another design of HBT cell developed starting from a fully textured PVS 2T tandem solar cell reported in literature. The cell has an optimized design and a perovskite layer with higher optical absorption.
Simulating a textured solar cell requires a hybrid optical model that combine TMM for thin-layer-stack with Monte Carlo RayTracing to take into account scattering effects at the textured surface. Due to the complexity of the optical model, simulations are firstly verified for a 2T solar cell against the experimental data. Then, the model is used to analyze the performance of the proposed PVS 3T-HBT solar cell with respect to the 2T one. From simulation results, we have obtained that the 3T-HBT textured device, exploiting a *n-i-p* PVK architecture, achieves a high efficiency of 28.2 %, in line with the 2T benchmark.
We also verify that for both planar and textured HBT designs, the MPP of the tandem HBT corresponds to the MPP of the two sub-cells working as if they were isolated from each other, i.e. there is no the transistor effect, confirming the preliminary remarks provided by the analytical model.
Given the excellent performance of the *intrinsic* HBT tandem demonstrated on the basis of the opto-electronic simulations, Chapter 6 deals with the main possible bottleneck of this device, i.e. the fact that the implementation of the third terminal and corresponding metal grid will introduce further optical and electrical loss with respect to the conventional 2T structure. This is particularly relevant in the prospect of analyzing the feasibility of large area HBT tandems. In this regard, we have assessed, through electro-optical simulations of the 3T-HBT device combined with circuit-level simulations, both optical and resistive losses provided by the adoption of a Top Interdigitated Contact (TIC) configuration for the emitter and base current collection. To estimate power losses, we have modeled the distributed losses through an equivalent lumped resistances accounting for contact resistances, lateral and orthogonal current flow and series resistances of the metal fingers. Also, the power loss generation associated to the shaded regions is taken into account by applying a shading loss factor. The study shows that due to the presence of the base resistance, the working point of each junction depends on the working point of the other one, by reducing the efficiency of the HBT device. In particular, simulations show that the base resistance is strongly dependent on the HBT configuration (*n-p-n* or *p-n-p*) and on the bottom cell technology. By adopting a SHJ technology, the high sheet resistance of the a-Si:H layers shall be mitigated by the low sheet resistance

of the ETL layer, hence by exploiting a *p-n-p* configuration. Thus, a *n-p-n* design should be avoided since the total series resistance is dominated by the high lateral resistance of the HTL/a-Si:H stack unless highly conductive HTL materials become available. On the other hand, when resorting to a homo-junction Si bottom cell, the low sheet resistance of the Silicon base layer minimizes the parasitic effect of the TIC layout. With an optimized TIC layout, efficiency losses remain lower than 5 % for finger lengths up to about 6-8 cm depending on the base sheet resistance. These are promising results in view of the feasibility of large area 3T-HBTs and prompt for further layout engineering to pursue a better trade off between optical and electrical losses, *e.g.* by implementing an overlapped layout for the base and emitter metal grids.

Overall, the study reported in this dissertation demonstrate that the HBT architecture exhibits attractive potential to develop high efficiency three-terminal perovskite/silicon tandems that can be integrated with industry standard silicon bottom cells. In this perspective, we need to focus on the practical realization of the HBT device. In this regard, based on my visit at CHOSE, where I worked on the fabrication of *p-i-n* perovskite solar cell, an interesting solution could be to realize a PVK/Si 3T-HBT cell by adopting hybrid deposition process for the PVK layer and optimize material and device structure/layout with accurate opto-electronic model. In this regard, the modeling tool for PVK/Si 3T tandems, developed in this thesis, could be extended to include specific features of the PVK and organic materials, such as transport of mobile ions in the PVK film and transport at the heterointerfaces dominated by hopping phenomena. In addition, from the optical point of view, the optimization of the physics-based model could include the study of more advanced photonic effects such as photon recycling effects, and the development of a more accurate 3D fully coupled opto-electronic simulation tools accounting for the presence of textured surfaces. In conclusion, from the electrical point of view and in the perspective of scaling up to large areas, it could be interesting refining the modelling approach for the optimization of the collecting grid layout and explore novel solutions.

Appendix A

Visit to CHOSE: perovskite deposition, porosity and correlation with model

In this Appendix, I describe preliminary methods and results experienced during a long visit of four month at CHOSE at University of Rome Tor Vergata.
Deposition technique and temperature conditions are crucial for perovskite solar cell performance. There are three main methods for preparing perovskite films [104]: solution processing, vapor deposition and hybrid vapor-solution processing. Solution processing can either be through a one-step method or a two-step sequential method. The one-step method is based on spin-coating of a mixed CH_3NH_3X and PbX_2 solution. Instead, the two-step process, mostly exploited for mesoporous substrate, consists on a first spin-coats PbI_2 and then dipping in a CH_3NH_3X solution. Another interesting technique is the vapour deposition one that produces high-quality uniform planar perovskite solar cells by co-evaporation of CH_3NH_3X and PbX_2 at the same time. Finally, another deposition technique is the two-step hybrid vacuum-solution deposition process [105].
In this regard, during my visit at CHOSE, I have been working on the fabrication of *p-i-n* perovskite solar cell with a hybrid deposition process in which PbI_2 is deposited by vapor deposition, while the CH_3NH_3I is deposited by spin coating technique. Being an initial development, one key point to be studied was to correlate the parameters of the deposition technique to the porosity of PbI_2. In this regard, a study has been initiated to support with optical simulations the experimental activity.

A.1 Development of the hybrid deposition process

Fabrication of *p-i-n* perovskite solar cell, carried out at CHOSE, is based on a hybrid deposition process. In this regard, for high device performance, it is necessary to focus on one of the main aspect of the deposition technique, that is the complete conversion of the PbI_2 into the $CH_3NH_3PbI_3$ (MAPI) perovskite structure [106] by thermal evaporation of PbI_2 followed by spin coating of the precursor CH_3NH_3I (MAI).

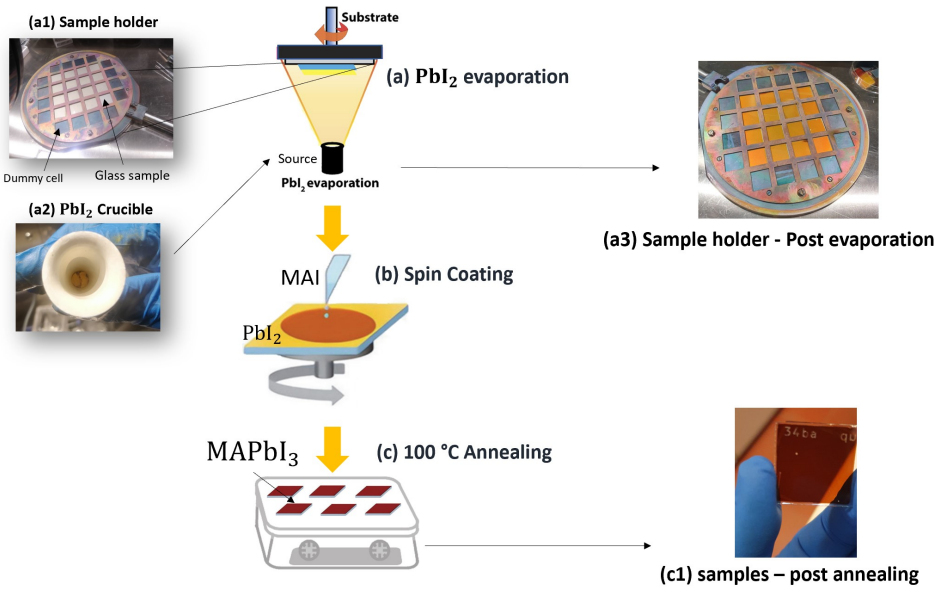

Fig. A.1 Two-step vapor-solution deposition process.

Fig. A.1 shows the schematic of the two-step vapor-solution deposition process of hybrid perovskite thin-film. Before PbI_2 evaporation process, samples are cleaned sequentially with deionized water, acetone and isopropanol (IPA) using an ultrasonic cleaner for 10 min and then dried in N_2 gas flow. Subsequently, the substrates are treated by UV ozone cleaner for 10 min. Then, Glass samples, brought inside the glove box of the evaporator machine, are placed on the sample holder of Fig. A.1a1. Then, the sample holder is placed on the top of the evaporator chamber with the exposed sample area downward (Fig. A.1a). Figure A.1a2 shows the PbI_2 powder in the crucible that evaporates at 280 °C and is deposited on the Glass substrate (2.5 cm x 2.5 cm). During the evaporation, the plate where the sample holder is placed rotates guaranteeing an uniform deposition of the PbI_2. Fig. A.1a3 shows

the post evaporated sample. Since the perovskite is fabricated with hybrid vapor-solution deposition, the second step is the solution process via spin coating. In this regard, 40 mg/mL of CH_3NH_3I (MAI) are dissolved in 2-propanol (IPA). Then, the MAI solution is spin coated with both static (substrate is spun after deposition) and dynamic (solution is deposited during spinning) technique onto the Glass/PbI2 sample at 3000 rpm for 40 s. Subsequently, the film is annealed at 100 °C for 10 min to obtain the perovskite film.
Phase structures of the MAPI samples are then studied by using X-ray diffraction (XRD) measurement, and the results are shown in Fig. A.2. In both Glass/MAPI samples, obtained with dynamic and static spin coating, we can observe two peaks: one at 15.1° that is ascribed to MAPI and, the second one, at 13.7°, that is ascribed to the residual PbI_2. Thus, for both sample, the total conversion of PbI_2 in MAPI is not

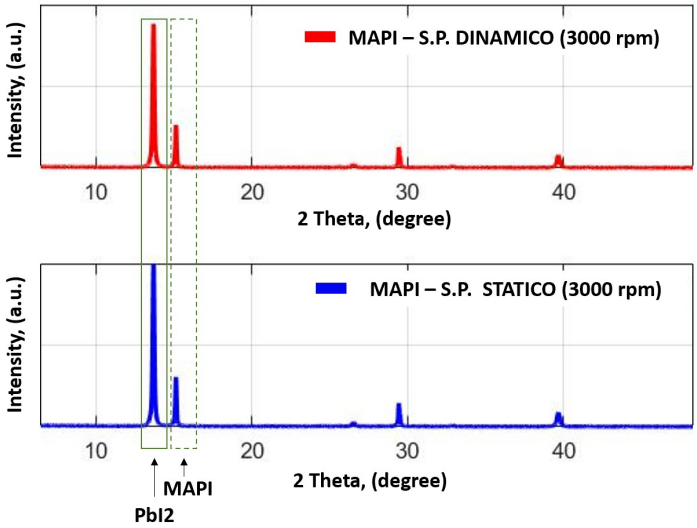

Fig. A.2 XRD patterns of MAPI film. The dashed green box highlights the first diffraction peak of the MAPI at 15.1°, the solid green box the PbI_2 one at 13.7°. In line with [107].

achieved. We further investigate the morphology of the samples through Field Effect Scanning Electron Microscope (FE-SEM). Fig. A.3a shows the FE-SEM images of the evaporated PbI_2 on Glass. Instead, Fig. A.3b shows the SEM image of the MAPI on Glass obtained by static (a) and dynamic (b) spin coating. In Fig. A.3c, we can detect the presence of the residual PbI_2 (yellow solid circle) in line with results shown in Fig. A.2. In this regard, get to know the porosity of the PbI_2 has a key role to attempt complete perovskite conversion. In fact, a porous PbI_2 structure allows

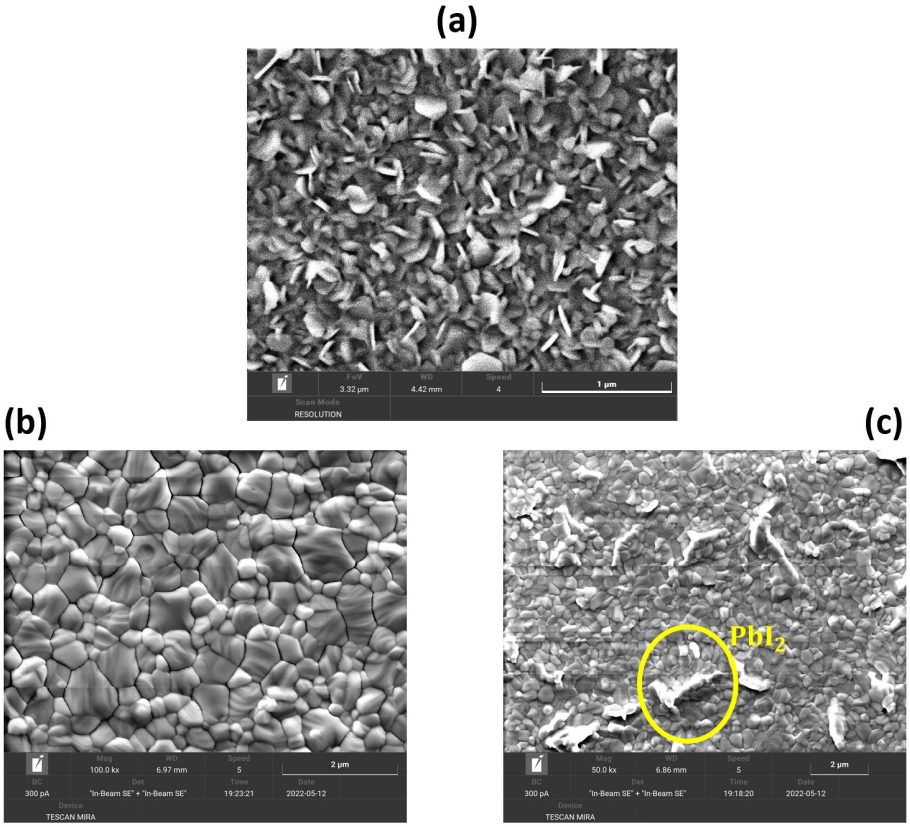

Fig. A.3 Top view, cross-sectional SEM images of (a) PbI_2 on Glass (b) MAPI on Glass for static spin coating (3000 rpm), (c) MAPI on Glass for dinamic spin coating (3000 rpm).

MAI solution to penetrate deep into the layer leading to a high crystal growth [108] by improving the efficiency and stability of the perovskite solar cell [109].

A.2 PbI_2 porosity: characterization and modeling

Optical modeling of the PbI_2 was developed to support an experimental study aimed at characterizing the porosity of the PbI_2 film. Depending on several evaporation factors, for example temperature and evaporation rate, the PbI_2 layer presents a different porosity. As shown in Fig. A.4, we can suppose that the first nanometers near Glass/PbI_2 interface form a compact layer, while the remaining part tends to be highly porous. Although the total thickness is known, the thickness of the compact and porous layers and the porosity are unknown. Thus, the main goal is to obtain the porosity and thickness for both compact and porous layer. Fig. A.4

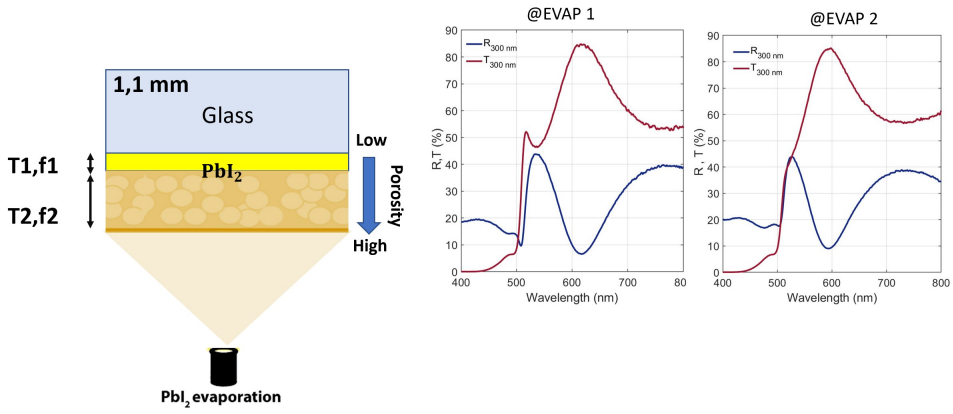

Fig. A.4 Sketch of PbI_2 on Glass.

shows reflectance and transmittance spectra, obtained by the spectrophotometer, for two different evaporation processes of PbI_2. For both samples, the total PbI_2 thickness, measured with the profilometer machine is of about $\sim$300 nm. With this aim, we implement an optical model able to obtain porosity and thickness of the PbI_2 starting from the measured reflectance and transmittance, drawing the total thickness measured by the profilometer. Thus, the variable unknowns are four: thickness (T_1 and T_2) and porosity (f_1 and f_2) of each PbI_2 layer (Fig. A.4). The optical modeling implemented combines the General Scattering Matrix Method (GSMM), to take into account incoherent propagation through the Glass layer, and the effective medium approximation (EMA) based on Bruggeman's model to obtain the refractive index of the porous layer.

A.2.1 General Scattering Matrix Method

Reflectance and transmittance of the sample Glass/PbI_2 is obtained by implementing the general transfer matrix method, which is able to treat some layers of a multilayer sytem as coherent and others as incoherent (internal interference ignored). That is the case of a thin layer (300 nm) deposited on top of a glass substrate (1.1 mm). The thickness of the glass is much larger than the light wavelength, hence light propagation must be treated as incoherent layer in this subdomain. We implement the model reported in [110], which consists of the following steps:

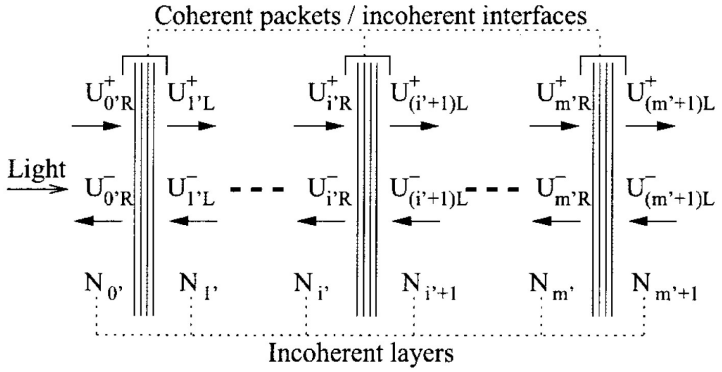

Fig. A.5 Schematic representation of a multilayer with forward and backward-propagating electric field components shown.

- the multi-layer system is divided in a subset of layers that can be treated as coherent and other subset of incoherent layers, as in Fig. A.5.
- for each packet of coherent layers, one can use the classical Scattering matrix formalism (Eq. A.1) to compute the scattering matrix **S** (Eq. A.2) and therefore the associated front-reflectance (r) (Eq. A.10) and front-transmittance (t) (Eq. A.11), and the back-reflectance (r') (Eq. A.12) and back-transmittance coefficients (t') (Eq. A.13) values.
- then, the obtained r, t, r', t' are used to compute an equivalent incoherent interface matrix $\bar{\mathbf{I}}$ Eq. A.16, reducing the mixed coherent-incoherent problem to the incoherent one.
- the final scattering matrix $\bar{\mathbf{S}}$ can be computed based on both propagation matrices $\bar{\mathbf{I}}$ (Eq. A.16) and $\bar{\mathbf{L}}$ (Eq. A.17).

$$\begin{bmatrix} E_{0R}^{+} \\ E_{0R}^{-} \end{bmatrix} = \mathbf{S} \begin{bmatrix} E_{(m+1)L}^{+} \\ E_{(m+1)L}^{-} \end{bmatrix} \tag{A.1}$$

where E_{0R}^{+} (E_{0R}^{-}) is the electric field, just before the first interface, associated with the wave propagating in the positive (negative) direction, $E_{(m+1)L}$ is the electric field just after the last interface, and **S** is the 2x2 scattering matrix,

$$\mathbf{S} = \mathbf{I}_{01}\mathbf{L}_{1}\mathbf{I}_{12}...\mathbf{L}_{\mathrm{m}}\mathbf{I}_{\mathrm{m+1}} \tag{A.2}$$

where $\mathbf{I}_{j(j+1)}$ defines the wave propagation at the interface between the film j and $j+1$ and $\mathbf{L}_j$ describes the wave propagation through the film j. The matrix $\mathbf{I}$ (2 x 2) is defined as

$$\mathbf{I}_{i,j} = \frac{1}{t_{ij}} \begin{bmatrix} 1 & r_{ij} \\ r_{ij} & 1 \end{bmatrix} \tag{A.3}$$

where t_{ij} and r_{ij} are the Fresnel coefficients at the interface ij:

$$r_{ij,p} = \frac{N_j cos\phi_i - N_i cos\phi_j}{N_j cos\phi_i + N_i cos\phi_j} \tag{A.4}$$

$$r_{ij,s} = \frac{N_i cos\phi_i - N_i cos\phi_j}{N_i cos\phi_i + N_j cos\phi_j} \tag{A.5}$$

$$t_{ij,p} = \frac{2N_i cos\phi_i}{N_j cos\phi_i + N_i cos\phi_j} \tag{A.6}$$

$$t_{ij,s} = \frac{2N_i cos\phi_i}{N_i cos\phi_i + N_j cos\phi_j} \tag{A.7}$$

where N is the complex index of refraction of the material (N=n+ik), ϕ is the complex propagation angle (ϕ=0 for light perpendicular to the interface) and the suffixes p and s refer to the wave polarization state parallel (TM waves) and perpendicular (TE waves) to the incident plane, respectively. The matrix $\mathbf{L}$ is defined as:

$$\mathbf{L}_j = \mathbf{L}(\beta_j) = \begin{bmatrix} \exp(-i\beta_j) & 0 \\ 0 & \exp(i\beta_j) \end{bmatrix} \tag{A.8}$$

where β is the phase shift that is due to the wave passing through the film j and is defined by the equation

$$\beta_j = \frac{2\pi d_j N}{\lambda} cos\phi_j \tag{A.9}$$

where λ is the wavelength of the incident light and d is the layer thickness. From the scattering matrix, it is possible to calculate the front-reflectance and front-transmittance coefficients

$$r = \frac{S_{21}}{S_{11}} \tag{A.10}$$

$$t = \frac{1}{S_{11}} \tag{A.11}$$

and the back-reflectance and back-transmittance coefficients

$$r' = -\frac{S_{12}}{S_{11}} \tag{A.12}$$

$$t' = \frac{detS}{S_{11}} \tag{A.13}$$

where $detS$ is the S matrix determinant.
In the case of multilayer incoherent layers, Eq. A.1 can be rewritten in terms of amplitude square of the electric field $U = |E|^2$,

$$\begin{bmatrix} U^+_{0\text{'R}} \\ U^-_{0\text{'R}} \end{bmatrix} = \bar{\mathbf{S}} \begin{bmatrix} U^+_{(\text{m'}1)\text{L}} \\ U^-_{(\text{m'}1)\text{L}} \end{bmatrix} \tag{A.14}$$

$\bar{\mathbf{S}}$ identifies the scattering matrix in the incoherent case. Thus, Eq. A.2 becomes

$$\bar{\mathbf{S}} = \bar{\mathbf{I}}_{0\text{'}1\text{'}}\bar{\mathbf{L}}_{1\text{'}}\bar{\mathbf{I}}_{1\text{'}2\text{'}}...\bar{\mathbf{L}}_{\text{m'}}, \bar{\mathbf{I}}'_{\text{m'(m'+1)}} \tag{A.15}$$

The propagation matrix $\bar{\mathbf{I}}$ in the incoherent case can be defined as:

$$\bar{\mathbf{I}}_{\text{j'(j'+1)}} = \frac{1}{|t|^2} \begin{bmatrix} 1 & -|r'|^2 \\ |r|^2 & |tt'|^2 - |rr'|^2 \end{bmatrix} \tag{A.16}$$

where r and t are the complex reflection and transmission coefficients, respectively, of the interface $j'(j'+1)$ for light moving in a positive direction and r' and t' for light moving in a negative direction. The matrix $\bar{\mathbf{L}}$ in the incoherent case can be defined as:

$$\bar{\mathbf{L}}_{\text{j'}} = \bar{\mathbf{L}}(\beta_{\text{j'}}) = \begin{bmatrix} \left|\exp(-i\beta_{\text{j}})\right|^2 & 0 \\ 0 & \left|\exp(i\beta_{\text{j}})\right|^2 \end{bmatrix} \tag{A.17}$$

Once computed the incoherent scattering matrix $\bar{\mathbf{S}}$ considering both propagation matrices $\bar{\mathbf{I}}$ and $\bar{\mathbf{L}}$ in the incoherent case, it is possible to compute the front-reflectance and front-transmittance coefficients as:

$$\bar{r} = \frac{\bar{S}_{21}}{\bar{S}_{11}} \tag{A.18}$$

$$\bar{t} = \frac{1}{\bar{S}_{11}} \tag{A.19}$$

and the back-reflectance and back-transmittance coefficients as:

$$\bar{r}' = -\frac{\bar{S}_{12}}{\bar{S}_{11}} \tag{A.20}$$

$$\bar{t}' = \frac{det\bar{S}}{\bar{S}_{11}} \tag{A.21}$$

where $det\bar{S}$ is the $\bar{S}$ matrix determinant.

A.2.2 Bruggeman's model for porous PbI_2

The refraction complex index of the porous PbI_2 material is computed through the Landauer–Bruggeman effective-medium approximation [111], that can be applied to random composite media. In this regard, we can consider a random mixture of two types of grains, A and B present in relative volume fraction f and $1-f$, whose dielectric constant are ε_A and ε_B, respectively. We can suppose that each grain is immersed in a homogeneous *effective medium* whose dielectric constant ε_* can be determined by the quadratic equation:

$$f\frac{\varepsilon_A - \varepsilon_*}{\varepsilon_A + 2\varepsilon_*} + (1-f)\frac{\varepsilon_B - \varepsilon_*}{\varepsilon_B + 2\varepsilon_*} = 0 \tag{A.22}$$

In our case study, ε_A is the dielectric constant of the compact PbI_2 and ε_B is the dielectric constant of the air. The dielectric constant of the compact PbI_2 is taken from [112].

A.2.3 Combined optical modeling

Aiming at fitting the reflectance and transmittance of the Glass/PbI_2 sample, we have combined the GSMM with the Bruggeman's model and a fitting routine into Matlab has been implemented to estimate T_1, T_2, f_1, f_2 (Fig. A.4) based on the comparison between measured and simulated reflectance spectra (Fig. A.6). The routine terminates when it founds a simulated reflectance curve $R(T_1, T_2, f_1, f_2)$ (dashed

blue curve in Fig. A.6) with a relative error lower than 5% with respect to that one obtained experimentally (blue solid curve in Fig. A.6) from the spectrophotometer. Fig. A.6 shows the results obtained for two different evaporation processes. We guess that the difference between the experimental and simulated curves relies on the choice of the dielectric constant of the compact PbI_2 that is taken from literature. To improve the fit, it would be necessary to calculate the optical constants of the porous PbI_2 layer through the Bruggeman's model starting from the dielectric constants, computed by ellipsometry measurements, of the compact PbI_2 material evaporated in laboratory.

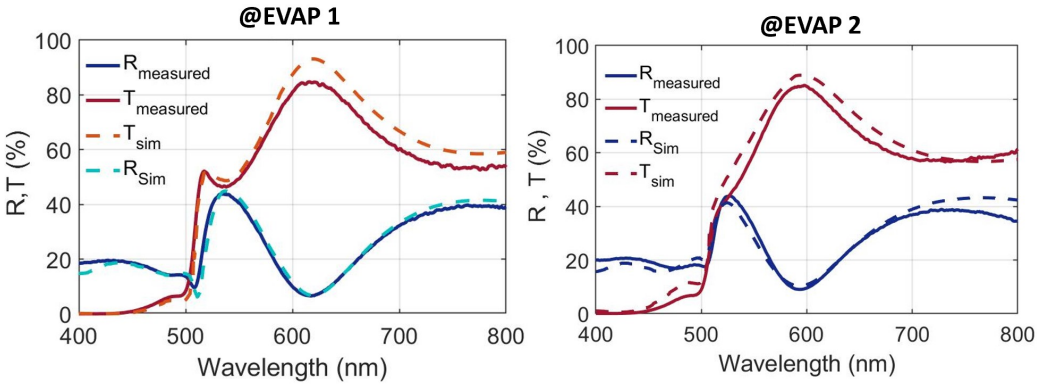

Fig. A.6 Simulated and measured reflectance and transmittance.

Table A.1 shows an example of estimated porosity percentage and thickness for the case under study.

	f1	f2	T1	T2
EVAP 1	86 %	77 %	93 nm	155 nm
EVAP 2	90 %	45 %	61 nm	246 nm

Table A.1 Simulation results.

The model and examples discussed here could be further developed to implement a way of controlling the PbI_2 evaporation process. In this context, further work is necessary in order to obtain a complete conversion of the PbI_2 into the MAPI perovskite structure by studying the porosity of the evaporated PbI_2 and characterizing the correlation between the PbI_2 porosity and morphology of the MAPI thin-film [106, 108, 109].

Appendix B

Shockley-Queisser model of the 3T-HBT Tandem

In this Appendix, we summarize the main steps to obtain the efficiency limit of a 3T-HBT solar cell, as reported in [16]. The model in [16] is an extension of the well-known Shockley-Queisser *detailed balance limit* [21] for a single gap solar cell. The main assumption is that the only two physical processes that occur in the cells are generation and radiative emission of photons (radiative recombination process). The sketch of a 3T-HBT structure under study is shown in Fig. B.1a. The main hypothesis is that the cell, at the ambient temperature T_c=300 K, is illuminated by a black body at the sun temperature T_s=6000 K. In the back side of the collector a back reflector is inserted to avoid luminescent radiation from the rear side.
In Fig. B.1a, the emitter and base are made of a high-gap semiconductor (E_H), and the collector of a low-gap one (E_L). Let's assume that the base of the 3T-HBT is 'long' [16], i.e. photons emitted by the emitter towards the collector are fully absorbed in the base layer and do not reach the collector. Moreover, we assume that carriers generated in the emitter (collector) cannot reach the collector (emitter) due to the high recombination rate in the base layer. Thus, the 3T-HBTsc can be studied as two junctions emitter-base and base-collector, independently connected, as shown in Fig.B.1b. Under these assumptions, the equivalent circuit model of the 3T-HBT solar cell is shown in Fig.B.2, where J_E (J_C) is the total current provided by the emitter-base (base-collector) junction, J^D_{TOP} (J^D_{BOT}) is the emitter-base (base-collector) dark current and J^{ph}_{TOP} (J^{ph}_{BOT}) is the emitter-base (base-collector) photogenerated current. To evaluate the emitter and collector currents provided by 3T-HBTsc working under

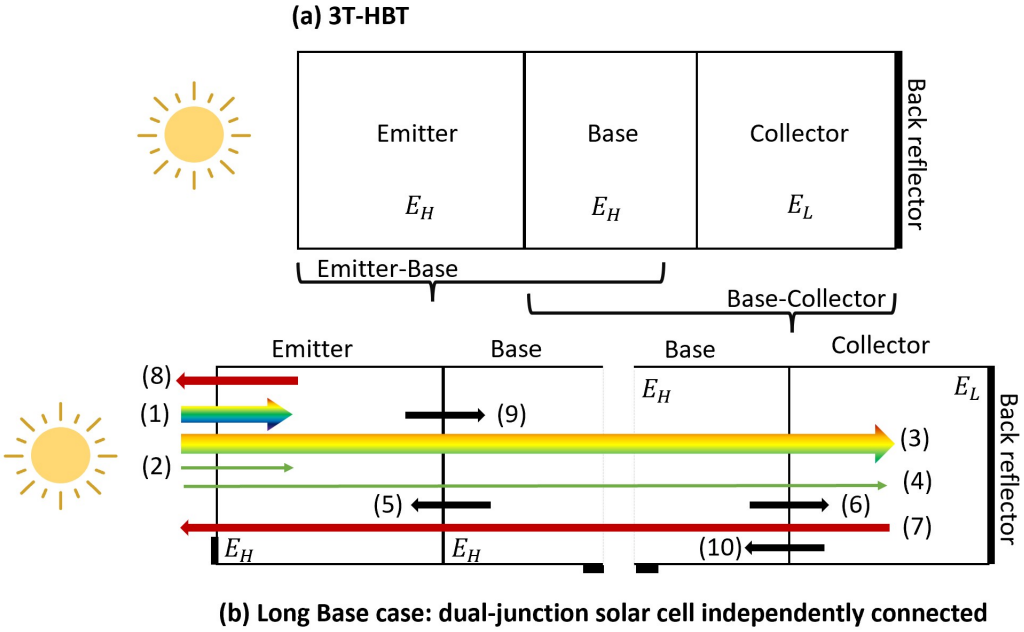

Fig. B.1 (a) Scketch of a 3T-HBT device. (b) Schematic figure of the 3T-HBT under the assumption of Long Base. The figure shows the photon fluxes. (1) $F^{\mathrm{E}}_{\mathrm{abs}}/q$ and (3) F^{C}_{abs}/q are the photons absorbed from the sun in the emitter and collector layer, respectively. (2) $F^{\mathrm{E}}_{\mathrm{abs,amb}}/q$ and (4) $F^{\mathrm{C}}_{\mathrm{abs,amb}}/q$ are related to the photons absorbed from the ambience in the emitter and collector layer. (5) $F^{\mathrm{B}}_{\mathrm{em,E}}/q$ and (6) $F^{\mathrm{B}}_{\mathrm{em,C}}/q$ represent the electroluminescent emission from the base respectively towards the emitter and collector. (7) $F^{\mathrm{E}}_{\mathrm{em,amb}}/q$ and (8) $F^{\mathrm{C}}_{\mathrm{em,amb}}/q$ are photons emitted by the emitter and collector layer to the ambient. (9) $F^{\mathrm{E}}_{\mathrm{em,B}}/q$ (10) $F^{\mathrm{C}}_{\mathrm{em,B}}/q$ represent the electroluminescent emission from the emitter and collector towards the base.

the radiative limit, let's consider the photon fluxes, shown in Fig. B.1b, that are involved in the cell under illumination condition. In this regard, we define the function F [22] as follows:

$$F(E_1,E_2,\mu,T) = \frac{2\pi}{h^3c^2}\int_{E_1}^{E_2}\frac{E^2}{\exp(\frac{E-\mu}{kT})}dE \tag{B.1}$$

where h the Planck's constant, c the speed of light in vacuum, k the Boltzman's constant. The function F corresponds, from a physical point of view, to a photon flux of temperature T, chemical potential μ, and energy between E_1 and E_2. Let's define the photon fluxes of Fig. B.1b for the emitter-base junction:

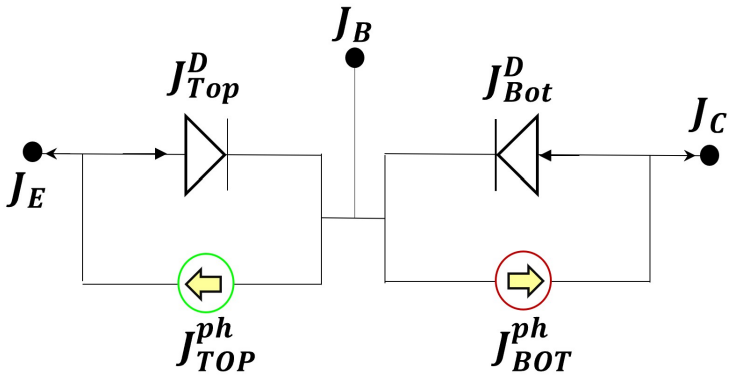

Fig. B.2 Equivalent Circuit model of the 3T-HBT Tandem under the assumption of 'long' base case.

- process (1): $F^{\mathrm{E}}_{\mathrm{abs}} = \frac{X}{X_{\mathrm{MAX}}} qF(E_{\mathrm{H}}, \infty, 0, T_{\mathrm{s}})$ corresponds to the photons from the sun, whose temperature is T_{s}, absorbed by the emitter.
- process (2): $F^{\mathrm{E}}_{\mathrm{abs,amb}} = \left(1 - \frac{X}{X_{\mathrm{MAX}}}\right) qF(E_{\mathrm{H}}, \infty, 0, T_{\mathrm{c}})$ corresponds to the photons from the ambience, whose temperature is T_{c}, absorbed by the emitter.
- process (5): $F^{\mathrm{B}}_{\mathrm{em,E}} = n_{\mathrm{r}}^2 qF(E_{\mathrm{H}}, \infty, qV_{\mathrm{BE}}, T_{\mathrm{c}})$ corresponds to the photons emitted from the front side of the base and absorbed by the emitter.
- process (8): $F^{\mathrm{E}}_{\mathrm{em,amb}} = qF(E_{\mathrm{H}}, \infty, qV_{\mathrm{BE}}, T_{\mathrm{c}})$ corresponds to the photons emitted from the front side of the emitter.
- process (9): $F^{\mathrm{E}}_{\mathrm{em,B}} = n_r^2 qF(E_{\mathrm{H}}, \infty, qV_{\mathrm{BE}}, T_{\mathrm{c}})$ corresponds to the photons emitted from the rear side of the emitter.

where V_{BE} is the emitter-base voltage, n_{r} [16, 22] is the refraction index of the low and high bandgap semiconductor, X is the light concentration factor, and $\frac{1}{X_{\mathrm{MAX}}} = sin^2\theta_{\mathrm{s}}$ where θ_{s} the semiangle of the sun seen from the Earth [22]. The total emitter current can be formulated as:

$$J_{\mathrm{E}} = F^{\mathrm{E}}_{\mathrm{abs}} + F^{\mathrm{E}}_{\mathrm{abs,amb}} - F^{\mathrm{E}}_{\mathrm{em,amb}} - F^{\mathrm{E}}_{\mathrm{em,B}} + F^{\mathrm{B}}_{\mathrm{em,E}} \tag{B.2}$$

Since $F^{\mathrm{B}}_{\mathrm{em,E}} = F^{\mathrm{E}}_{\mathrm{em,B}}$, Eq. B.2 can be rewritten as

$$J_{\mathrm{E}} = \underbrace{F^{\mathrm{E}}_{\mathrm{abs}} + F^{\mathrm{E}}_{\mathrm{abs,amb}}}_{J^{\mathrm{ph}}_{\mathrm{TOP}}} - \underbrace{F^{\mathrm{E}}_{\mathrm{em,amb}}}_{J^{\mathrm{D}}_{\mathrm{TOP}}} \tag{B.3}$$

where $J^{\mathrm{ph}}_{\mathrm{TOP}}$ and $J^{\mathrm{D}}_{\mathrm{TOP}}$ are the terms in Fig. B.2.

Then, by considering the base-collector junction, we obtain that:

- process (3): $F^{\mathrm{C}}_{\mathrm{abs}} = \frac{X}{X_{\mathrm{MAX}}} qF(E_{\mathrm{L}}, E_{\mathrm{H}}, 0, T_{\mathrm{s}})$ corresponds to the photons from the sun, whose temperature is T_{s}, absorbed by the collector. The collector layer, characterized by a low-gap, absorbs the remaining part of the solar spectrum that has not been absorbed by the high-gap emitter-base junction.
- process (4): $F^{\mathrm{C}}_{\mathrm{abs,amb}} = \left(1 - \frac{X}{X_{\mathrm{MAX}}}\right) qF(E_{\mathrm{L}}, E_{\mathrm{H}}, 0, T_{\mathrm{c}})$ corresponds to the photons from the ambience, whose temperature is T_c, absorbed by the collector.
- process (6): $F^{\mathrm{B}}_{\mathrm{em,C}} = n_{\mathrm{r}}^2 qF(E_{\mathrm{H}}, \infty, qV_{\mathrm{BC}}, T_{\mathrm{c}})$ corresponds to the photons emitted from the rear side of the base and absorbed by the collector.
- process (7): $F^{\mathrm{C}}_{\mathrm{em,amb}} = qF(E_{\mathrm{L}}, E_{\mathrm{H}}, qV_{\mathrm{BC}}, T_{\mathrm{c}})$ corresponds to the photons emitted from the front side of the collector towards the base. They escape into the air since their energy is lower than the gap of the base.
- process (10): $F^{\mathrm{C}}_{\mathrm{em,B}} = n_{\mathrm{r}}^2 qF(E_{\mathrm{H}}, \infty, qV_{\mathrm{BC}}, T_{\mathrm{c}})$ corresponds to the photons emitted from the front side of the collector and absorbed by the base. This quantity is linked to the process (7): collector layer emits photons ($E > E_{\mathrm{L}}$), some of them escape from the front side of the 3T-HBT if $E < E_{\mathrm{H}}$, others are absorbed into the base layer if $E > E_{\mathrm{H}}$.

where V_{BC} is the collector-base voltage. The total collector current can be read as :

$$J_{\mathrm{E}} = F^{\mathrm{C}}_{abs} + F^{\mathrm{C}}_{\mathrm{abs,amb}} - F^{\mathrm{C}}_{\mathrm{em,amb}} - F^{\mathrm{C}}_{\mathrm{em,B}} + F^{\mathrm{B}}_{\mathrm{em,C}} \tag{B.4}$$

Since $F^{\mathrm{B}}_{\mathrm{em,C}} = F^{\mathrm{C}}_{\mathrm{em,B}}$, Eq. B.4 can be rewritten as

$$J_{\mathrm{C}} = \underbrace{F^{\mathrm{C}}_{\mathrm{abs}} + F^{\mathrm{C}}_{\mathrm{abs,amb}}}_{J^{\mathrm{ph}}_{\mathrm{BOT}}} - \underbrace{F^{\mathrm{C}}_{\mathrm{em,amb}}}_{J^{\mathrm{D}}_{\mathrm{BOT}}} \tag{B.5}$$

where J^{ph}_{BOT} and J^{D}_{BOT} are the terms in Fig. B.2. Thus, the total radiative efficiency of the 3T-HBT is the sum of the efficiency achieved by each sub-cell.
For completeness, the assumption of 'short' base case, discussed also in [16], leads to the fact that generation and recombination of carriers in the base region become negligible. Thus, emission of photons from the emitter and collector, respectively from the rear and front side, leads to an absorption of photons no more in the base, but in the collector and emitter respectively. Mathematically, process (5) and process (6) should be rewritten as follows:

- process (5): $F^{B}_{em,E} = n_r^2 qF(E_H, \infty, qV_{BC}, T_c)$. It is associated to the number of photons emitted from the front side of the collector and absorbed by the emitter.
- process (6): $F^{B}_{em,C} = n_r^2 qF(E_H, \infty, qV_{BE}, T_c)$. It is associated to the number of photons emitted from the rear side of the emitter and absorbed by the collector.

where we have replaced the term V_{BE} (V_{BC}) with $V_{BC}(V_{BE})$ in $F^{B}_{em,E}$ ($F^{B}_{em,C}$). In this case, the two junctions are not independent and the injection of carriers from the emitter towards the collector and viceversa must be taken into account. Please refer to Sec.3.2.
The total power of the 3T-HBT can be computed as:

$$P_{3T\text{-}HBT} = J_E V_{BE} + J_C V_{BC} \tag{B.6}$$

In Chapter 3, Fig. 3.2 and Fig. 3.3 are obtained through the presented model under the long base assumption. The same model can be applied to the 2T-tandem whose total output power can be written as:

$$P_{2T} = J_{tandem} V_{tandem} \tag{B.7}$$

where $J_{tandem} = [0 \div \min(J_E, J_C)]$ and the voltage can be expressed as:

$$V_{tandem}(J) = V_c \ln\left(\frac{J^{ph}_{TOP} - J_{tandem}}{J^{D}_{s,TOP}} + 1\right) + V_c \ln\left(\frac{J^{ph}_{BOT} - J_{tandem}}{J^{D}_{s,BOT}} + 1\right) \tag{B.8}$$

where $V_c = k_B T_c / q$.

Appendix C

Hovel model: extended current density equations for the 3T-HBT solar cell

In Figure C.1, the x axis has the origin at the leftmost side of the emitter region (n-type, length w_{E}), the inner base region (p-type, length w_{B}) is between $x = w_{\mathrm{E}}$ and $x = w_{\mathrm{E}} + w_{\mathrm{B}}$, and finally the collector region (n-type, length w_{C}) is defined between $x = w_{\mathrm{E}} + w_{\mathrm{B}}$ and $x = w_{\mathrm{E}} + w_{\mathrm{B}} + w_{\mathrm{C}}$. Light is impinging from the emitter region.

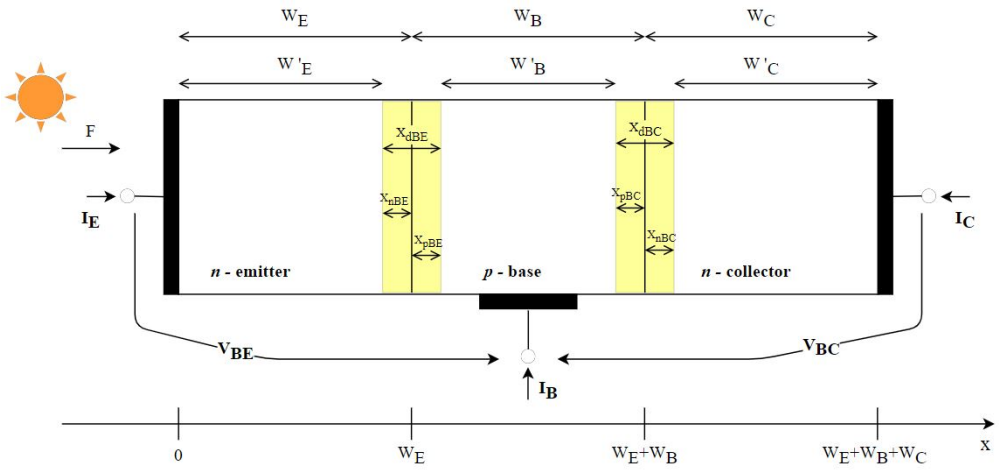

Fig. C.1 3T-HBT structure as considered in the model derivation. Yellow rectangles between the emitter-base and base-collector regions highlight the depleted regions.

Emitter current density

Starting equation for the n-type emitter region:

$$\frac{d^2(p_{\mathrm{n}}-p_{\mathrm{n0}})}{dx^2}-\left(\frac{p_{\mathrm{n}}-p_{\mathrm{n0}}}{D_{\mathrm{pE}}\tau_{\mathrm{p}}}\right)+\left(\frac{\alpha_{\mathrm{E}}F(1-R_{\mathrm{E}})\mathrm{e}^{(-\alpha_{\mathrm{E}}x)}}{D_{\mathrm{pE}}}\right)=0 \tag{C.1}$$

where F is the photon flux.
Emitter boundary equations:

$$\frac{d(p_{\mathrm{n}}-p_{\mathrm{n0}})}{dx}=\frac{S_{\mathrm{pE}}}{D_{\mathrm{pE}}}(p_{\mathrm{n}}-p_{\mathrm{n0}});\quad \text{for } x=0 \tag{C.2}$$

$$p_{\mathrm{n}}=p_{\mathrm{n0}}e^{(qV_{\mathrm{BE}}/kT)};\quad \text{for } x=w'_{\mathrm{E}} \tag{C.3}$$

Eq. C.1 can be solved considering the two boundary conditions Eq. C.2 and Eq. C.3. We obtain that the hole component of the emitter current density at the base-emitter junction, $J_{\mathrm{pE}}(x=w'_{\mathrm{E}})$, can be written as

$$\begin{aligned}
J_{\mathrm{pE}} &= -qD_{\mathrm{pE}}\frac{ni^2}{N_{\mathrm{D}}}\frac{1}{L_{\mathrm{pE}}}\left[\frac{\sinh\left(\frac{w'_{\mathrm{E}}}{L_{\mathrm{pE}}}\right)+\frac{S_{\mathrm{pE}}L_{\mathrm{pE}}}{D_{\mathrm{pE}}}\cosh\left(\frac{w'_{\mathrm{E}}}{L_{\mathrm{pE}}}\right)}{\cosh\left(\frac{w'_{\mathrm{E}}}{L_{\mathrm{pE}}}\right)+\frac{S_{\mathrm{pE}}L_{\mathrm{pE}}}{D_{\mathrm{pE}}}\sinh\left(\frac{w'_{\mathrm{E}}}{L_{\mathrm{pE}}}\right)}\right]\left(\mathrm{e}^{\left(\frac{qV_{\mathrm{BE}}}{KT}\right)}-1\right)\\
&+qL_{\mathrm{pE}}\frac{\alpha_{\mathrm{E}}F(1-R_{\mathrm{E}})}{\alpha_{\mathrm{E}}^2L_{\mathrm{pE}}^2-1}\left[\frac{\left(\alpha_{\mathrm{E}}L_{\mathrm{pE}}+\frac{S_{\mathrm{pE}}L_{\mathrm{pE}}}{D_{\mathrm{pE}}}\right)-\mathrm{e}^{-\alpha_{\mathrm{E}}w'_{\mathrm{E}}}\left(\sinh\left(\frac{w'_{\mathrm{E}}}{L_{\mathrm{pE}}}\right)+\frac{S_{\mathrm{pE}}L_{\mathrm{pE}}}{D_{\mathrm{pE}}}\cosh\left(\frac{w'_{\mathrm{E}}}{L_{\mathrm{pE}}}\right)\right)}{\cosh\left(\frac{w'_{\mathrm{E}}}{L_{\mathrm{pE}}}\right)+\frac{S_{\mathrm{p}}L_{\mathrm{pE}}}{D_{\mathrm{pE}}}sinh\left(\frac{w'_{\mathrm{E}}}{L_{\mathrm{pE}}}\right)}\right]\\
&-qL_{\mathrm{pE}}\frac{\alpha_{\mathrm{E}}F(1-R_{\mathrm{E}})}{\alpha_{\mathrm{E}}^2L_{\mathrm{pE}}^2-1}\left(\alpha_{\mathrm{E}}\,\mathrm{e}^{-\alpha_{\mathrm{E}}w'_{\mathrm{E}}}\right)
\end{aligned} \tag{C.4}$$

Base current density

Starting equation for the p-type base region:

$$\frac{d^2(n_{\mathrm{p}}-n_{\mathrm{p0}})}{dx^2}-\left(\frac{n_{\mathrm{p}}-n_{\mathrm{p0}}}{D_{\mathrm{nB}}\tau_{\mathrm{n}}}\right)+\left(\frac{\alpha_{\mathrm{B}}F(1-R_{\mathrm{E}})\mathrm{e}^{(-\alpha_{\mathrm{E}}W_{\mathrm{E}})}(1-R_{\mathrm{B}})\mathrm{e}^{(-\alpha_{\mathrm{B}}(x-W_{\mathrm{E}}))}}{D_{\mathrm{nB}}}\right)=0 \tag{C.5}$$

Base boundary conditions:

$$n_{\mathrm{p}}-n_{\mathrm{p0}}=n_{\mathrm{p}}^{'}=n_{\mathrm{p0}}\left(\mathrm{e}^{\left(\frac{qV_{\mathrm{BE}}}{KT}\right)}-1\right);\quad \text{for } x=W_{\mathrm{E}}+x_{\mathrm{pBE}} \tag{C.6}$$

$$n_{\mathrm{p}}-n_{\mathrm{p0}}=n_{\mathrm{p}}^{''}=n_{\mathrm{p0}}\left(\mathrm{e}^{\left(\frac{qV_{\mathrm{BC}}}{KT}\right)}-1\right);\quad \text{for } x=W_{\mathrm{E}}+x_{\mathrm{pBE}}+w_{\mathrm{B}}^{\prime} \tag{C.7}$$

Eq. C.5 can be solved considering the two boundary conditions Eq. C.6 and Eq. C.7. We obtain that the electron component of the base current density at the base-emitter junction, $J_{\mathrm{nB}}(x=W_{\mathrm{E}}+x_{\mathrm{pBE}})$, can be written as

$$J_{\mathrm{nB}}(W_{\mathrm{E}}+x_{\mathrm{pBE}})=q\frac{D_{\mathrm{n}}}{L_{\mathrm{nB}}}\left[\frac{n_{\mathrm{p0}}\left(\mathrm{e}^{\left(\frac{qV_{\mathrm{BC}}}{KT}\right)}-1\right)-\cosh\left(\frac{w_{\mathrm{B}}^{\prime}}{L_{\mathrm{nB}}}\right)n_{\mathrm{p0}}\left(\mathrm{e}^{\left(\frac{qV_{\mathrm{BE}}}{KT}\right)}-1\right)}{\sinh\left(\frac{w_{\mathrm{B}}^{\prime}}{L_{\mathrm{nB}}}\right)}\right]+$$

$$+qL_{\mathrm{nB}}\frac{\mathrm{e}^{-\alpha_{\mathrm{E}}W_{\mathrm{E}}}\alpha_{\mathrm{B}}F(1-R_{\mathrm{E}})(1-R_{\mathrm{B}})}{\alpha_{\mathrm{B}}^2L_{\mathrm{nB}}^2-1}\left[\frac{\mathrm{e}^{-\alpha_{\mathrm{B}}\left(x_{\mathrm{pBE}}+w_{\mathrm{B}}^{\prime}\right)}-\cosh\left(\frac{w_{\mathrm{B}}^{\prime}}{L_{\mathrm{nB}}}\right)\mathrm{e}^{-\alpha_{\mathrm{B}}x_{\mathrm{pBE}}}}{\sinh\left(\frac{w_{\mathrm{B}}^{\prime}}{L_{\mathrm{nB}}}\right)}+L_{\mathrm{nB}}\alpha_{\mathrm{B}}\mathrm{e}^{-\alpha_{\mathrm{B}}\left(x_{\mathrm{pBE}}\right)}\right] \tag{C.8}$$

Then, the electron component of the base current density at the base-collector junction, $J_{\mathrm{nB}}(x = W_{\mathrm{E}} + x_{\mathrm{pBE}} + w'_{\mathrm{B}})$, can be written as

$$J_{\mathrm{nB}}(W_{\mathrm{E}} + x_{\mathrm{pBE}} + w'_{\mathrm{B}}) = q\frac{D_{\mathrm{n}}}{L_{\mathrm{nB}}}\left[\frac{-n_{\mathrm{p0}}\left(\mathrm{e}^{\left(\frac{qV_{\mathrm{BE}}}{KT}\right)} - 1\right) + n_{\mathrm{p0}}\cosh\left(\frac{w'_{\mathrm{B}}}{L_{\mathrm{nB}}}\right)\left(\mathrm{e}^{\left(\frac{qV_{\mathrm{BC}}}{KT}\right)} - 1\right)}{\sinh\left(\frac{w'_{\mathrm{B}}}{L_{\mathrm{nB}}}\right)}\right] +$$

$$\frac{qL_{\mathrm{nB}}\mathrm{e}^{-\alpha_{\mathrm{E}}W_{\mathrm{E}}}\alpha_{\mathrm{B}}F(1-R_{\mathrm{E}})(1-R_{\mathrm{B}})}{\alpha_{\mathrm{B}}^2L_{\mathrm{nB}}^2 - 1}\left[\frac{\cosh\left(\frac{w'_{\mathrm{B}}}{L_{\mathrm{nB}}}\right)\mathrm{e}^{-\alpha_{\mathrm{B}}(x_{\mathrm{pBE}}+w'_{\mathrm{B}})} - \mathrm{e}^{-\alpha_{\mathrm{B}}\left(x_{\mathrm{pBE}}\right)}}{\sinh\left(\frac{w'_{\mathrm{B}}}{L_{\mathrm{nB}}}\right)} + L_{\mathrm{nB}}\alpha_{\mathrm{B}}\mathrm{e}^{-\alpha_{\mathrm{B}}\left(x_{\mathrm{pBE}}+w'_{\mathrm{B}}\right)}\right] \tag{C.9}$$

Collector current density

Starting equation for the n-type collector region:

$$\frac{d^2(p_{\mathrm{n}} - p_{\mathrm{n0}})}{dx^2} - \left(\frac{p_{\mathrm{n}} - p_{\mathrm{n0}}}{D_{\mathrm{pC}}\tau_{\mathrm{p}}}\right) + G_{\mathrm{c}} = 0 \tag{C.10}$$

where G_{c} reads as

$$G_{\mathrm{c}} = \frac{\alpha_{\mathrm{C}}F(1-R_{\mathrm{E}})(1-R_{\mathrm{B}})(1-R_{\mathrm{C}})e^{-\alpha_{\mathrm{E}}(W_{\mathrm{E}})}e^{-\alpha_{\mathrm{B}}(W_{\mathrm{B}})}e^{-\alpha_{\mathrm{C}}(x-W_{\mathrm{E}}-W_{\mathrm{B}})}}{D_{\mathrm{pC}}} \tag{C.11}$$

Collector boundary conditions:

$$p_{\mathrm{n}} = p_{\mathrm{n0}}\mathrm{e}^{\left(\frac{qV_{\mathrm{BC}}}{kT}\right)}; \quad \text{for } x = W_{\mathrm{E}} + W_{\mathrm{B}} + x_{\mathrm{nBC}} \tag{C.12}$$

$$\frac{d(p_{\mathrm{n}} - p_{\mathrm{n0}})}{dx} = -\frac{S_{\mathrm{pC}}}{D_{\mathrm{pC}}}(p_{\mathrm{n}} - p_{\mathrm{n0}}); \quad \text{for } x = H \tag{C.13}$$

Eq. C.10 can be solved considering the two boundary conditions Eq. C.12 and Eq. C.13. We obtain that the hole component of the collector current density at the base-collector junction, $J_{\mathrm{pC}}(x = W_{\mathrm{E}} + W_{\mathrm{B}} + x_{\mathrm{nBC}})$, reads as

$$J_{\mathrm{pC}}(W_{\mathrm{E}} + W_{\mathrm{B}} + x_{\mathrm{nBC}}) = \left[\frac{\sinh\left(\frac{H'}{L_{\mathrm{pC}}}\right) + \frac{S_{\mathrm{p}} L_{\mathrm{pC}}}{D_{\mathrm{pC}}} \cosh\left(\frac{H'}{L_{\mathrm{pC}}}\right)}{\cosh\left(\frac{H'}{L_{\mathrm{pC}}}\right) + \frac{S_{\mathrm{p}} L_{\mathrm{pC}}}{D_{\mathrm{pC}}} \sinh\left(\frac{H'}{L_{\mathrm{pC}}}\right)} \right] \left(\mathrm{e}^{\left(\frac{qV_{\mathrm{BC}}}{KT}\right)} - 1 \right) \times$$

$$qD_{\mathrm{pC}} \frac{ni^2}{N_{\mathrm{D}}} \frac{1}{L_{\mathrm{pC}}} - \frac{qL_{\mathrm{pC}} \alpha_{\mathrm{C}} (1 - R_{\mathrm{E}})(1 - R_{\mathrm{B}})(1 - R_{\mathrm{C}}) F \mathrm{e}^{-\alpha_{\mathrm{E}}(W_{\mathrm{E}})} \mathrm{e}^{-\alpha_{\mathrm{B}}(W_{\mathrm{B}})} \mathrm{e}^{-\alpha_{\mathrm{C}}(x_{\mathrm{nBC}})}}{\alpha^2 L_{\mathrm{pC}}^2 - 1} \tag{C.14}$$

$$\left[\alpha_{\mathrm{C}} L_{\mathrm{pC}} - \frac{\frac{S_{\mathrm{p}} L_{\mathrm{pC}}}{D_{\mathrm{pC}}} \left[\cosh \frac{H'}{L_{\mathrm{pC}}} - \mathrm{e}^{-\alpha_{\mathrm{C}} H'} \right] + \sinh \frac{H'}{L_{\mathrm{pC}}} + \alpha_{\mathrm{C}} L_{\mathrm{pC}} e^{-\alpha_{\mathrm{C}} H'}}{\cosh\left(\frac{H'}{L_{\mathrm{pC}}}\right) + \frac{S_{\mathrm{p}} L_{\mathrm{pC}}}{D_{\mathrm{pC}}} \sinh\left(\frac{H'}{L_{\mathrm{pC}}}\right)} \right]$$

where $H' = H - (W_{\mathrm{E}} + W_{\mathrm{B}} + x_{\mathrm{nBC}})$.

Photocurrent in the depleted regions

The photocurrent density in the emitter-base and base-collector depleted regions is obtained considering a unitary collection efficiency. Thus, the electron and hole pairs generated into the depleted regions and, collected at the emitter and collector terminals, are equal to the number of photons absorbed.
$J_{\mathrm{EB}}^{\mathrm{dr}}$ is the photocurrent generated in the emitter-base depleted region. It reads as

$$J_{\mathrm{EB}}^{\mathrm{dr}} = F(1 - R_{\mathrm{E}}) \left\{ \mathrm{e}^{-\alpha_{\mathrm{E}} w'_{\mathrm{E}}} \left[1 - \mathrm{e}^{-\alpha_{\mathrm{E}} x_{\mathrm{nBE}}} \right] + (1 - R_{\mathrm{B}}) \mathrm{e}^{-\alpha_{\mathrm{E}} w_{\mathrm{E}}} \left[1 - \mathrm{e}^{-\alpha_{\mathrm{B}} x_{\mathrm{pBE}}} \right] \right\} \tag{C.15}$$

and $J_{\mathrm{BC}}^{\mathrm{dr}}$ is the photocurrent generated in the base-collector depleted region:

$$J_{\mathrm{BC}}^{\mathrm{dr}} = F(1-R_{\mathrm{E}})(1-R_{\mathrm{B}})\,\mathrm{e}^{-\alpha_{\mathrm{E}} w_{\mathrm{E}}} \left\{ \mathrm{e}^{-\alpha_{\mathrm{B}}(w'_{\mathrm{B}} + x_{\mathrm{pBE}})} \right.$$
$$\left. \times \left[1 - \mathrm{e}^{\alpha_{\mathrm{B}} x_{\mathrm{pBC}}}\right] + (1-R_{\mathrm{C}})\,\mathrm{e}^{-\alpha_{\mathrm{B}} w_{\mathrm{B}}} \left[1 - \mathrm{e}^{-\alpha_{\mathrm{C}} x_{\mathrm{nBC}}}\right] \right\} \qquad \text{(C.16)}$$

Appendix D

Power loss analysis

The idea to simulate the distributed losses in a solar cell by using an equivalent lumped series resistance in conjunction with a simple diode model was explored in 1960 for the optimization of grid electrode pattern [113]. Here, the resistive losses from lateral current in the base as well as in the emitter of the 3T-HBT sc (Fig.D.1) and resistive losses from the fingers are discussed. Figure D.1a shows the flat *p-n-p*

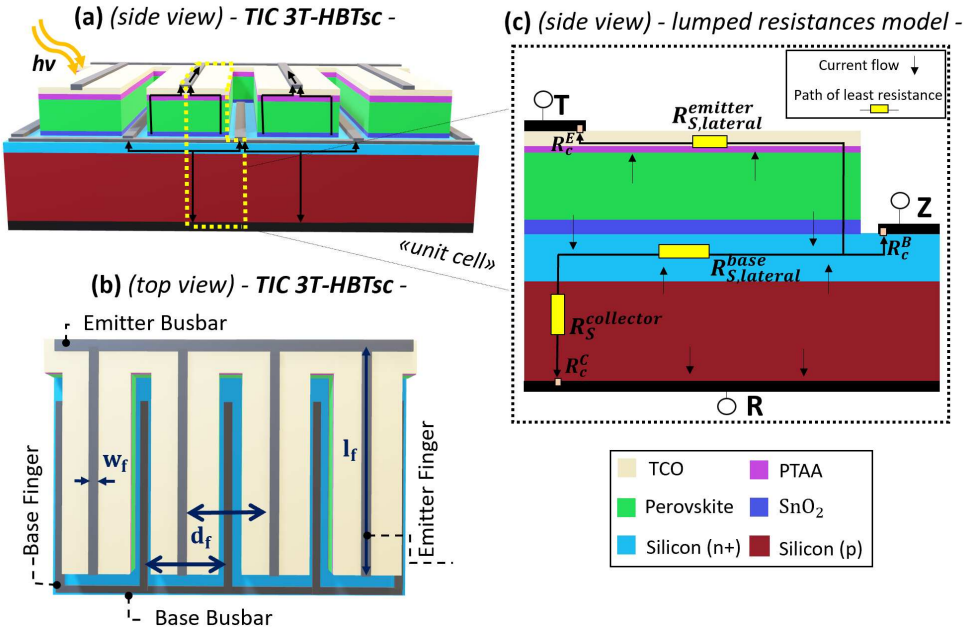

Fig. D.1 3T-HBTsc with TIC configuration: (a) side view (b) top view. (c) Dashed black inset: unit cell of the 3T-HBT sc, in which yellow rectangles depict the lumped resistances.

PVS 3T-HBT proposed in Chapter 6 made on n^+/p Si homo-junction bottom sub

cell. From the top: the TCO/PTAA/PVK layer stack constitutes the p-emitter layer; the ETL/n-Si layers form the n-base layer on top of p-type c-Si collector. In Figure D.1b, d_{f}, w_{f} and l_{f} are the finger distance, width and length, respectively.
Here, to estimate power losses in the 3T-HBT solar cell under study, we have adopted a well-known approach based on a lumped description of the current collecting grid [96]. Thus, we have considered a *unit cell* of the front metallic grid (yellow dashed box in Figure 6.3a) and modeled the distributed losses through equivalent lumped resistances [96]. In Figure D.1c, $R_{\mathrm{c}}^{\mathrm{E}}$, $R_{\mathrm{c}}^{\mathrm{B}}$, $R_{\mathrm{c}}^{\mathrm{C}}$ are the contact resistances at the interface emitter/T-contact, base/Z-contact and collector/R-contact, respectively; $R_{\mathrm{S,lateral}}^{\mathrm{emitter}}$ and $R_{\mathrm{S,lateral}}^{\mathrm{base}}$ account for the contribution of lateral current flow; $R_{\mathrm{S}}^{\mathrm{collector}}$ for the orthogonal current flow; R_{finger} accounts for the series resistance of the metal fingers. As discussed in Chapter 6, we obtain that the emitter, base and collector series resistances, respectively R_{E}, R_{B} and R_{C} ($\Omega\mathrm{cm}^2$), read as

$$R_{\mathrm{E}} = R_{\mathrm{S,lateral}}^{\mathrm{E}} + R_{\mathrm{c}}^{\mathrm{E}} + R_{\mathrm{f}}^{\mathrm{E}} \tag{D.1a}$$

$$R_{\mathrm{B}} = R_{\mathrm{S,lateral}}^{\mathrm{B}} + R_{\mathrm{c}}^{\mathrm{B}} + R_{\mathrm{f}}^{\mathrm{B}} \tag{D.1b}$$

$$R_{\mathrm{C}} = \rho_{p\text{-Si}} t_{\mathrm{collector}} \tag{D.1c}$$

The general expression for the series resistance ($\Omega\mathrm{cm}^2$) reads as

$$R_{*} = \frac{P_{\mathrm{loss,uc}}}{I_{\mathrm{uc}}^2} \times A_{\mathrm{uc}} \tag{D.2}$$

where $P_{\mathrm{loss,uc}}$ is the power loss and I_{uc} is the current photo-generated in the unit-cell (uc) of interest, of area A_{uc}. In order to obtain the lateral and finger resistances, the methodology in [96] will be followed, by computing:

- the expression for power loss due to resistive paths
- the generated current density
- the area of each unit cell

D.1 Resistive losses from lateral transport

The same analytical method used to compute the lateral resistance in the base layer can be adopted to compute that one in the emitter. Thus, let's consider the base layer, that is n(+)-Silicon in Fig. D.1c where the metal contact is placed. We highlight that when we consider the unit cell, we are keeping half of the base layer, as showed in Fig.D.2a.

Let's assume that:

- the base layer is uniformly illuminated
- a constant current enters the layer in the z-direction $I_{z=0} = I_T$, I_T being a constant current value
- power dissipation associated to current flow in the z-direction can be neglected.

Thus, Fig. D.2.a can be redrawn as Fig. D.2.b where we have considered the grid electrodes as equipotentials [113].

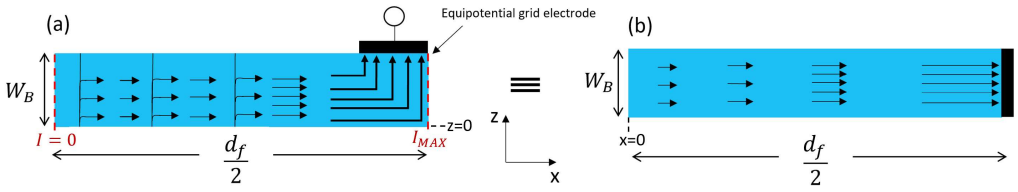

Fig. D.2 Schematic diagram of the actual current flow (a) Schematic diagram of the assumed current (flow) (b) [113]

The sheet resistance R_{sh} ($\Omega/\square$) of the n(+)-Silicon base layer reads as

$$R_{sh} = \frac{1}{q\mu N_D W_B} \tag{D.3}$$

where μ is the electron mobility, N_D the layer doping, W_B base thickness and q the electron charge.
Let's assume that in the base layer the current $I(x)$ increases linearly across the x-axis (Fig. D.2) [113, 114].

Thus, the current in Fig. D.2b can be expressed as:

$$I(x) = I_{\mathrm{T}} \frac{x}{a} \tag{D.4}$$

where $a = d_{\mathrm{f}}$, that is the width of the base layer (Fig.D.1b).
Since the current $I(x)$ is not homogeneous in the x-direction, the power loss due to resistive effects in the base across the *unit cell* is calculated using an integral expression:

$$P_{\mathrm{loss}}(base) = 2 \int_0^{d_{\mathrm{f}}/2} I(x)^2 \, dR \tag{D.5}$$

In the power loss expression, the factor 2 takes into account the current coming from both sides of the finger.
The resistance of a cross section perpendicular to the finger can be expressed as

$$dR = \frac{R_{\mathrm{sh}}}{l_{\mathrm{f}}} dx \tag{D.6}$$

where l_{f} is the finger length (Fig.D.1b).
The power dissipated in the base across a unit cell can be read as

$$P = 2 \int_0^{d_{\mathrm{f}}/2} I(x)^2 \frac{R_{\mathrm{sh}}}{l_{\mathrm{f}}} \, dx = 2 \frac{I_{\mathrm{T}}^2 R_{\mathrm{sh}}}{a^2 l_{\mathrm{f}}} \int_0^{d_{\mathrm{f}}/2} x^2 \, dx \tag{D.7}$$

and after integration:

$$P = \frac{1}{12} R_{\mathrm{sh}} \frac{I_{\mathrm{T}}^2 d_{\mathrm{f}}}{l_{\mathrm{f}}} \tag{D.8}$$

From Eq. D.2 the series resistance can be expressed as

$$R_{\mathrm{lateral}} = \frac{P}{I_{\mathrm{T}}^2} \times A_{\mathrm{uc}} \tag{D.9}$$

thus, we obtain that the final expression of the lateral base resistance:

$$R_{\mathrm{lateral}} = \frac{R_{\mathrm{sh}}}{12} d_{\mathrm{f}}^2 \tag{D.10}$$

Eq. D.10 is also valid for the emitter lateral resistance. As explained in Chapter 6, to obtain the lateral base and emitter resistances of the 3T-HBT solar cell, it is necessary to consider the total sheet resistance R_{sh} of the thin layers constituting the base and emitter regions. For the sake of completeness, the effective sheet resistance

of the emitter (TCO/PTAA/PVK) and base (SnO_2/n-Si) layers can be expressed as:

$$R_{\text{tot,sh}}^{\text{Emitter}} = \left(\frac{1}{R_{\text{sh}}^{\text{ITO}}} + \frac{1}{R_{\text{sh}}^{\text{HTL}}} + \frac{1}{R_{\text{sh}}^{\text{PVK}}} \right)^{-1} \tag{D.11a}$$

$$R_{\text{tot,sh}}^{\text{Base}} = \left(\frac{1}{R_{\text{sh}}^{\text{SnO}_2}} + \frac{1}{R_{\text{sh}}^{\text{c-Si(n}^+\text{)}}} \right)^{-1} \tag{D.11b}$$

D.2 Finger resistance

The methodology to compute the finger resistance is roughly the same of that one in Sec. D.1. Let's consider Fig. D.3, that is the top view of the unit cell of Fig. D.1. Let's consider the y-direction. The current flow in the y-direction increases linearly

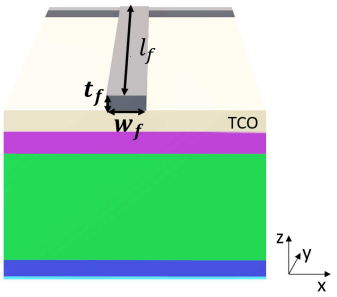

Fig. D.3 Focus on the emitter layer: top view of the 3T-HBT unit cell.

(same assumptions of Sec. D.1):

$$I(y) = I_{\text{T}} \frac{y}{l_{\text{f}}} \tag{D.12}$$

where l_{f} is the finger length. Since the current $I(y)$ is not homogeneous in the y-direction, the power loss due to resistive effects is calculated by using the integral expression:

$$P_{\text{loss}}(finger) = \int_0^{l_{\text{f}}} I(y)^2 \, dR \tag{D.13}$$

where

$$dR = \frac{\rho_{\text{m}}}{t_{\text{f}} w_{\text{f}}} dy \tag{D.14}$$

ρ_{m} being the metal resistivity, and t_{f} and w_{f} the thickness and width of the finger. Considering Eq. D.14 and Eq. D.12, Eq. D.13 can be rewritten as

$$P_{\mathrm{loss}}(finger) = \int_0^{l_{\mathrm{f}}} I_{\mathrm{T}}^2 \frac{\rho_{\mathrm{m}}}{t_{\mathrm{f}} w_{\mathrm{f}} l_{\mathrm{f}}^2} y^2 \, dy = \frac{I_{\mathrm{T}}^2 \rho_{\mathrm{m}}}{t_{\mathrm{f}} w_{\mathrm{f}}} \frac{l_{\mathrm{f}}}{3} \tag{D.15}$$

Considering Eq. D.15 and Eq. D.2, the final expression of the finger resistance R_{f} reads as

$$R_{\mathrm{f}} = \frac{\rho_{\mathrm{m}} l_{\mathrm{f}}^2 d_{\mathrm{f}}}{3 t_{\mathrm{f}} w_{\mathrm{f}}} \tag{D.16}$$

D.3 Resistive losses due to the contact

The expression for the contact resistance R_{c} [96] can be written as:

$$R_{\mathrm{c}} = d_{\mathrm{f}} \frac{\rho_{\mathrm{c}} w_{\mathrm{f}}}{2 L_{\mathrm{t}}} \coth\left(\frac{w_{\mathrm{f}}}{2 L_{\mathrm{t}}}\right) \tag{D.17}$$

where L_{t} is the transfer length of that contact, $L_{\mathrm{t}} = \sqrt{\frac{\rho_{\mathrm{c}}}{R_{sh}}}$.

References

[1] SP Global. What is energy transition. https://www.spglobal.com/en/research-insights/articles/what-is-energy-transition, 2020.

[2] IEA. World energy outlook 2022. https://www.iea.org/reports/world-energy-outlook-2022, 2022.

[3] Maria Mercedes Vanegas Cantarero. Of renewable energy, energy democracy, and sustainable development: A roadmap to accelerate the energy transition in developing countries. *Energy Research Social Science*, 70:101716, 2020.

[4] Grazia Giacovelli. Social capital and energy transition: A conceptual review. *Sustainability*, 14(15):9253, 2022.

[5] Joy Clancy and Marielle Feenstra. Women, gender equality and the energy transition in the eu, 05 2019.

[6] European Institute for Gender Equality EIGE. Gender and energy. 10.2839/94295, 2016.

[7] United States Energy Employment Report 2022 Canary Media. U.S Department of Energy. Electricity workforce is heavily male even more so for renewables, 2022.

[8] Bindu Shrestha, Sudarshan R Tiwari, Sushil B Bajracharya, Martina M Keitsch, and Hom B Rijal. Review on the importance of gender perspective in household energy-saving behavior and energy transition for sustainability. *Energies*, 14(22):7571, 2021.

[9] IRENA. Renewable energy: A gender perspective, 01 2019.

[10] United Nations Entity for Gender Equality and the Empowerment of Women (UN Women). Call to action gender equality in the renewable energy industry, 2020.

[11] IEA. Net zero by 2050. https://www.iea.org/reports/net-zero-by-2050, 2021.

[12] UNECE. Carbon neutrality in the unece region: Integrated life-cycle assessment of electricity sources. https://unece.org/sed/documents/2021/10/reports/life-cycle-assessment-electricity-generation-options, 2021.

[13] IEA. Co2 emissions in 2022. https://www.iea.org/reports/co2-emissions-in-2022, 2022.

[14] Abdulaziz SR Bati, Yu Lin Zhong, Paul L Burn, Mohammad Khaja Nazeeruddin, Paul E Shaw, and Munkhbayar Batmunkh. Next-generation applications for integrated perovskite solar cells. *Communications Materials*, 4(1):2, 2023.

[15] Fabrizio Gota, Malte Langenhorst, Raphael Schmager, Jonathan Lehr, and Ulrich W Paetzold. Energy yield advantages of three-terminal perovskite-silicon tandem photovoltaics. *Joule*, 4(11):2387–2403, 2020.

[16] A Martí and A Luque. Three-terminal heterojunction bipolar transistor solar cell for high-efficiency photovoltaic conversion. *Nature communications*, 6(1):1–6, 2015.

[17] Allen Chodos. April 25, 1954: Bell labs demonstrates the first practical silicon solar cell. *APS News-This month in Physics history*, 2009.

[18] Harold J Hovel. *Semiconductors and semimetals. Volume 11. Solar cells*. Academic Press, Inc., New York, 1975.

[19] Simon M. Sze and Kwok K. Ng. *Physics of Semiconductor Devices*. John Wiley & Sons, Ltd, 2006.

[20] Maksym Plakhotnyuk. Nanostructured heterojunction crystalline silicon solar cells with transition metal oxide carrier selective contacts. 2018.

[21] William Shockley and Hans J Queisser. Detailed balance limit of efficiency of p-n junction solar cells. *Journal of applied physics*, 32(3):510–519, 1961.

[22] Antonio Martí. Limiting efficiency of heterojunction solar cells. *IEEE Journal of Photovoltaics*, 9(6):1590–1595, 2019.

[23] Zachary C. Holman, Antoine Descoeudres, Loris Barraud, Fernando Zicarelli Fernandez, Johannes P. Seif, Stefaan De Wolf, and Christophe Ballif. Current losses at the front of silicon heterojunction solar cells. *IEEE Journal of Photovoltaics*, 2(1):7–15, 2012.

[24] Matthew P. Lumb, Christopher G. Bailey, Jessica G. J. Adams, Glen Hillier, Francis Tuminello, Victor C. Elarde, and Robert J. Walters. Extending the 1-d hovel model for coherent and incoherent back reflections in homojunction solar cells. *IEEE Journal of Quantum Electronics*, 49(5):462–470, 2013.

[25] Christophe Ballif, Franz-Josef Haug, Mathieu Boccard, Pierre J Verlinden, and Giso Hahn. Status and perspectives of crystalline silicon photovoltaics in research and industry. *Nature Reviews Materials*, 7(8):597–616, 2022.

[26] Martin Green, Ewan Dunlop, Jochen Hohl-Ebinger, Masahiro Yoshita, Nikos Kopidakis, and Xiaojing Hao. 3 solar cell efficiency tables (version 57). *Progress in Photovoltaics: Research and Applications*, 29(1):3–15, 2021.

[27] Brittany L Smith, Michael Woodhouse, Kelsey AW Horowitz, Timothy J Silverman, Jarett Zuboy, and Robert M Margolis. Photovoltaic (pv) module technologies: 2020 benchmark costs and technology evolution framework results. Technical report, National Renewable Energy Lab.(NREL), Golden, CO (United States), 2021.

[28] NREL. Best research-cell efficiencies: Emerging photovoltaics. https://www.nrel.gov/pv/assets/pdfs/cell-pv-eff-emergingpv.pdf, 2022.

[29] Christoph Messmer, Baljeet S. Goraya, Sebastian Nold, Patricia S.C. Schulze, Volker Sittinger, Jonas Schön, Jan Christoph Goldschmidt, Martin Bivour, Stefan W. Glunz, and Martin Hermle. The race for the best silicon bottom cell: Efficiency and cost evaluation of perovskite–silicon tandem solar cells. *Progress in Photovoltaics: Research and Applications*, 29(7):744–759, 2021.

[30] Markus Fischer. Itrpv 9th edition 2018 report release and key findings. In *PV CellTech conference*, volume 14, 2018.

[31] Lei Meng, Jingbi You, and Yang Yang. Addressing the stability issue of perovskite solar cells for commercial applications. *Nature communications*, 9(1):5265, 2018.

[32] Shuxia Tao, Ines Schmidt, Geert Brocks, Junke Jiang, Ionut Tranca, Klaus Meerholz, and Selina Olthof. Absolute energy level positions in tin- and lead-based halide perovskites. *Nat. Commun.*, 10(1):2560–2560, 2019.

[33] Jin Young Kim, Jin-Wook Lee, Hyun Suk Jung, Hyunjung Shin, and Nam-Gyu Park. High-efficiency perovskite solar cells. *Chemical Reviews*, 120(15):7867–7918, 2020.

[34] Christopher Eames, Jarvist M Frost, Piers RF Barnes, Brian C O'regan, Aron Walsh, and M Saiful Islam. Ionic transport in hybrid lead iodide perovskite solar cells. *Nature communications*, 6(1):7497, 2015.

[35] Moritz H. Futscher and Bruno Ehrler. Efficiency limit of perovskite/si tandem solar cells. *ACS Energy Letters*, 1(4):863–868, 2016.

[36] Tomas Leijtens, Kevin A Bush, Rohit Prasanna, and Michael D McGehee. Opportunities and challenges for tandem solar cells using metal halide perovskite semiconductors. *Nature Energy*, 3(10):828–838, 2018.

[37] William E. McMahon, John F. Geisz, Jeronimo Buencuerpo, and Emily L. Warren. A framework for comparing the energy production of photovoltaic modules using 2-, 3-, and 4-terminal tandem cells. *Sustainable Energy Fuels*, 7:461–470, 2023.

[38] Christoph Messmer, Baljeet S. Goraya, Sebastian Nold, Patricia S.C. Schulze, Volker Sittinger, Jonas Schön, Jan Christoph Goldschmidt, Martin Bivour, Stefan W. Glunz, and Martin Hermle. The race for the best silicon bottom cell: Efficiency and cost evaluation of perovskite–silicon tandem solar cells. *Progress in Photovoltaics: Research and Applications*, n/a(n/a), 2020.

[39] Ik Jae Park, Jae Hyun Park, Su Geun Ji, Min-Ah Park, Ju Hee Jang, and Jin Young Kim. A three-terminal monolithic perovskite/si tandem solar cell characterization platform. *Joule*, 3(3):807–818, 2019.

[40] S Sakai and M Umeno. Theoretical analysis of new wavelength-division solar cells. *Journal of Applied Physics*, 51(9):5018–5024, 1980.

[41] Emily L Warren, Michael G Deceglie, Michael Rienäcker, Robby Peibst, Adele C Tamboli, and Paul Stradins. Maximizing tandem solar cell power extraction using a three-terminal design. *Sustainable Energy & Fuels*, 2(6):1141–1147, 2018.

[42] Ik Jae Park, Jae Hyun Park, Su Geun Ji, Min-Ah Park, Ju Hee Jang, and Jin Young Kim. A three-terminal monolithic perovskite/si tandem solar cell characterization platform. *Joule*, 3(3):807–818, 2019.

[43] Gemma Giliberti, Francesco Di Giacomo, and Federica Cappelluti. Three terminal perovskite/silicon solar cell with bipolar transistor architecture. *Energies*, 15(21), 2022.

[44] Henning Schulte-Huxel, Daniel J Friedman, and Adele C Tamboli. String-level modeling of two, three, and four terminal si-based tandem modules. *IEEE Journal of Photovoltaics*, 8(5):1370–1375, 2018.

[45] Miha Filipič, Philipp Löper, Bjoern Niesen, Stefaan De Wolf, Janez Krč, Christophe Ballif, and Marko Topič. Ch3nh3pbi3 perovskite / silicon tandem solar cells: characterization based optical simulations. *Opt. Express*, 23(7):A263–A278, Apr 2015.

[46] Rudi Santbergen, Hisashi Uzu, Kenji Yamamoto, and Miro Zeman. Optimization of three-terminal perovskite/silicon tandem solar cells. *IEEE Journal of Photovoltaics*, 9(2):446–451, 2019.

[47] Syed Akhil, S. Akash, Altaf Pasha, Bhakti Kulkarni, Mohammed Jalalah, Mabkhoot A. Alsaiari, Farid A. Harraz, and R. Geetha Balakrishna. Review on perovskite silicon tandem solar cells: Status and prospects 2t, 3t and 4t for real world conditions. *Materials & Design*, 211:110138, 2021.

[48] Philipp Tockhorn, Philipp Wagner, Lukas Kegelmann, Johann-Christoph Stang, Mathias Mews, Steve Albrecht, and Lars Korte. Three-terminal perovskite/silicon tandem solar cells with top and interdigitated rear contacts. *ACS Applied Energy Materials*, 3(2):1381–1392, 2020.

[49] Rune Strandberg. Spectral and temperature sensitivity of area de-coupled tandem modules. In *2015 IEEE 42nd Photovoltaic Specialist Conference (PVSC)*, pages 1–6. IEEE, 2015.

[50] Hiroyuki Kanda, Valentin Dan Mihailetchi, Marie-Estelle Gueunier-Farret, Jean-Paul Kleider, Zakaria Djebbour, Jose Alvarez, Baranek Philippe, Olindo

Isabella, Malte R. Vogt, Rudi Santbergen, Philip Schulz, Fiala Peter, Mohammad K. Nazeeruddin, and James P. Connolly. Three-terminal perovskite/integrated back contact silicon tandem solar cells under low light intensity conditions. *Interdisciplinary Materials*, 1(1):148–156, 2022.

[51] Three-terminal perovskite/silicon tandem solar cells with top and interdigitated rear contacts. 3(2):1381–1392, 2020.

[52] Gemma Giliberti, Fabrizio Bonani, Antonio Martí, and Federica Cappelluti. Modeling of three-terminal heterojunction bipolar transistor solar cells. In *2020 International Conference on Numerical Simulation of Optoelectronic Devices (NUSOD)*, pages 43–44, 2020.

[53] Gemma Giliberti, Antonio Martí, and Federica Cappelluti. Perovskite-si solar cell: a three-terminal heterojunction bipolar transistor architecture. In *2020 47th IEEE Photovoltaic Specialists Conference (PVSC)*, pages 2696–2699, 2020.

[54] Babak Olyaeefar, Sohrab Ahmadi-Kandjani, and Asghar Asgari. Bulk and interface recombination in planar lead halide perovskite solar cells: A drift-diffusion study. *Physica E: Low-dimensional Systems and Nanostructures*, 94:118–122, 2017.

[55] Eike Khnen, Marko Jot, Anna Belen Morales-Vilches, Philipp Tockhorn, Amran Al-Ashouri, Bart Macco, Lukas Kegelmann, Lars Korte, Bernd Rech, Rutger Schlatmann, Bernd Stannowski, and Steve Albrecht. Highly efficient monolithic perovskite silicon tandem solar cells: analyzing the influence of current mismatch on device performance. *Sustainable Energy & Fuels*, 3(8):1995–2005, 2019.

[56] Yecheng Zhou and Angus Gray-Weale. A numerical model for charge transport and energy conversion of perovskite solar cells. *Phys. Chem. Chem. Phys.*, 18:4476–4486, 2016.

[57] Hassan Imran, Imranzeb Durrani, Muhammad Kamran, Tarek Mohammed Abdolkader, Muhammad Faryad, and Nauman Zafar Butt. High-performance bifacial perovskite/silicon double-tandem solar cell. *IEEE journal of photovoltaics*, 8(5):1222–1229, 2018.

[58] G. Masetti, M. Severi, and S. Solmi. Modeling of carrier mobility against carrier concentration in arsenic-, phosphorus-, and boron-doped silicon. *IEEE Transactions on Electron Devices*, 30(7):764–769, 1983.

[59] Yecheng Zhou and Angus Gray-Weale. A numerical model for charge transport and energy conversion of perovskite solar cells. *Physical Chemistry Chemical Physics*, 18(6):4476–4486, 2016.

[60] Elisa Antolín, Marius H. Zehender, Simon A. Svatek, Myles A. Steiner, Mario Martínez, Iván García, Pablo García-Linares, Emily L. Warren, Adele C.

Tamboli, and Antonio Martí. Progress in three-terminal heterojunction bipolar transistor solar cells. *Prog Photovolt Res Appl.*, 30(8):843–850, 2022.

[61] Sentaurus Device, Synopsys Inc., 2017.

[62] D Alonso-Alvarez, T Wilson, P Pearce, M Fuhrer, D Farrell, and N Ekins-Daukes. Solcore: a multi-scale, python-based library for modelling solar cells and semiconductor materials. *Journal of Computational Electronics*, 17:1099–1123, 2018.

[63] Synopsys, Sentaurus Device User Guide. Version i-2017, Mountain View, CA, sentaurus technology template: Eqe and i–v curve calculation of a textured silicon solar cell using the raytracer, 2017.

[64] Erin M. Tonita, Christopher E. Valdivia, Michael Martinez-Szewczyk, Mandy R. Lewis, Mariana I. Bertoni, and Karin Hinzer. Effect of air mass on carrier losses in bifacial silicon heterojunction solar cells. *Solar Energy Materials and Solar Cells*, 230:111293, 2021.

[65] Mario Ochoa Gómez. *TCAD Modelling, simulation and characterization of III-V multijunction solar cells*. PhD thesis, Universidad Politécnica de Madrid, 2018.

[66] Synopsys, Sentaurus Device User Guide. Version i-2017, Mountain View, CA, 2017.

[67] Sophocles J Orfanidis. Electromagnetic waves and antennas.

[68] Gemma Giliberti and Federica Cappelluti. Physical simulation of perovskite/silicon three-terminal tandems based on bipolar transistor structure. In Alexandre Freundlich, Stéphane Collin, and Karin Hinzer, editors, *Physics, Simulation, and Photonic Engineering of Photovoltaic Devices XI*, volume 11996, page 1199602. International Society for Optics and Photonics, SPIE, 2022.

[69] Felix Lang, Eike Koohnen, Jonathan Warby, Ke Xu, Max Grischek, Philipp Wagner, Dieter Neher, Lars Korte, Steve Albrecht, and Martin Stolterfoht. Revealing fundamental efficiency limits of monolithic perovskite/silicon tandem photovoltaics through subcell characterization. *ACS Energy Letters*, 6(11):3982–3991, 2021.

[70] Urs Aeberhard, Roger Hausermann, Andreas Schiller, Balthasar Blulle, and Beat Ruhstaller. Analysis and optimization of perovskite-silicon tandem solar cells by full opto-electronic simulation. In *2020 International Conference on Numerical Simulation of Optoelectronic Devices (NUSOD)*, pages 37–38. IEEE, 2020.

[71] Ya Wang, Meidouxue Han, Rongbo Wang, Juntao Zhao, Jiawei Zhang, Huizhi Ren, Guofu Hou, Yi Ding, Ying Zhao, and Xiaodan Zhang. Buried interface passivation strategies for high performance perovskite solar cells. *Journal of Materials Chemistry A*, 2023.

[72] Synopsys, Sentaurus Device User Guide. Version i-2017, Mountain View, CA, simulation of a gaas/gainp dual-junction solar cell, 2017.

[73] Florent Sahli, Jérémie Werner, Brett A Kamino, Matthias Bräuninger, Raphaël Monnard, Bertrand Paviet-Salomon, Loris Barraud, Laura Ding, Juan J Diaz Leon, Davide Sacchetto, Gianluca Cattaneo, Matthieu Despeisse, Mathieu Boccard, Sylvain Nicolay, Quentin Jeangros, Bjoern Niesen, and Christophe Ballif. Fully textured monolithic perovskite/silicon tandem solar cells with 25.2% power conversion efficiency. *Nature materials*, 17(9):820–826, 2018.

[74] Emily L. Warren, William E. McMahon, Michael Rienäcker, Kaitlyn T. VanSant, Riley C. Whitehead, Robby Peibst, and Adele C. Tamboli. A taxonomy for three-terminal tandem solar cells. *ACS Energy Letters*, 5(4):1233–1242, 2020.

[75] Babak Olyaeefar, Sohrab Ahmadi-Kandjani, and Asghar Asgari. Bulk and interface recombination in planar lead halide perovskite solar cells: A drift-diffusion study. *Physica E: Low-dimensional Systems and Nanostructures*, 94:118–122, 2017.

[76] Marko Jošt, Lukas Kegelmann, Lars Korte, and Steve Albrecht. Monolithic perovskite tandem solar cells: A review of the present status and advanced characterization methods toward 30% efficiency. *Advanced energy materials*, 10(26):1904102–n/a, 2020.

[77] Yichuan Chen, Qi Meng, Linrui Zhang, Changbao Han, Hongli Gao, Yongzhe Zhang, and Hui Yan. Sno2-based electron transporting layer materials for perovskite solar cells: A review of recent progress. *Journal of energy chemistry*, 35:144–167, 2019.

[78] Florine M Rombach, Saif A Haque, and Thomas J Macdonald. Lessons learned from spiro-ometad and ptaa in perovskite solar cells. *Energy & Environmental Science*, 2021.

[79] Hanul Min, Do Yoon Lee, Junu Kim, Gwisu Kim, Kyoung Su Lee, Jongbeom Kim, Min Jae Paik, Young Ki Kim, Kwang S. Kim, Min Gyu Kim, Tae Joo Shin, and Sang Il Seok. Perovskite solar cells with atomically coherent interlayers on sno2 electrodes. *Nature*, 598(7881):444–450, 2021.

[80] Guozheng Du, Li Yang, Cuiping Zhang, Xiaoli Zhang, Nicholas Rolston, Zhide Luo, and Jinbao Zhang. Evaporated undoped spiro-ometad enables stable perovskite solar cells exceeding 20% efficiency. *Advanced Energy Materials*, page 2103966, 2022.

[81] Matthew Kam, Qianpeng Zhang, Daquan Zhang, and Zhiyong Fan. Room-temperature sputtered sno2 as robust electron transport layer for air-stable and efficient perovskite solar cells on rigid and flexible substrates. *Sci. Rep.*, 9(1):1–10, 2019.

[82] Seungkyu Kim, Yong Ju Yun, Taemin Kim, Chanyong Lee, Yohan Ko, and Yongseok Jun. Hydrolysis-regulated chemical bath deposition of tin-oxide-based electron transport layers for efficient perovskite solar cells with a reduced potential loss. *Chem. Mater.*, 33(21):8194–8204, 2021.

[83] AJ Liu and S Nagel. Nature. *Nonlinear dynamics: Jamming is not just cool any more*, 396:21–22, 1998.

[84] Alexander J Bett, Kristina M Winkler, Martin Bivour, Ludmila Cojocaru, Ozde Kabakli, Patricia SC Schulze, Gerald Siefer, Leonard Tutsch, Martin Hermle, Stefan W Glunz, et al. Semi-transparent perovskite solar cells with ito directly sputtered on spiro-ometad for tandem applications. *ACS applied materials & interfaces*, 11(49):45796–45804, 2019.

[85] Kenjiro Miyano, Neeti Tripathi, Masatoshi Yanagida, and Yasuhiro Shirai. Lead halide perovskite photovoltaic as a model p–i–n diode. *Accounts of chemical research*, 49(2):303–310, 2016.

[86] Aaesha Alnuaimi, Ibraheem Almansouri, and Ammar Nayfeh. Effect of mobility and band structure of hole transport layer in planar heterojunction perovskite solar cells using 2d tcad simulation. *Journal of computational electronics*, 15(3):1110–1118, 2016.

[87] Thomas Kirchartz, Florian Staub, and Uwe Rau. Impact of photon recycling on the open-circuit voltage of metal halide perovskite solar cells. *ACS Energy Letters*, 1(4):731–739, 2016.

[88] S. Altazin, L. Stepanova, J. Werner, B. Niesen, C. Ballif, and B. Ruhstaller. Design of perovskite/crystalline-silicon monolithic tandem solar cells. *Opt. Express*, 26(10):A579–A590, May 2018.

[89] Juan-Pablo Correa-Baena, Miguel Anaya, Gabriel Lozano, Wolfgang Tress, Konrad Domanski, Michael Saliba, Taisuke Matsui, Tor Jesper Jacobsson, Mauricio E. Calvo, Antonio Abate, Michael Grätzel, Hernán Míguez, and Anders Hagfeldt. Unbroken perovskite: Interplay of morphology, electro-optical properties, and ionic movement. *Advanced Materials*, 28(25):5031–5037, 2016.

[90] Klaus Jäger, Johannes Sutter, Martin Hammerschmidt, Philipp-Immanuel Schneider, and Christiane Becker. Prospects of light management in perovskite/silicon tandem solar cells. *Nanophotonics*, 10(8):1991–2000, 2020.

[91] Thomas Stübinger. Optische modellierung und charakterisierung von organischen donor-akzeptor solarzellen. 2005.

[92] Timofey Golubev, Dianyi Liu, Richard Lunt, and Phillip Duxbury. Understanding the impact of c60 at the interface of perovskite solar cells via drift-diffusion modeling. *AIP Advances*, 9(3):035026, 2019.

[93] Rolf Häcker and Andreas Hangleiter. Intrinsic upper limits of the carrier lifetime in silicon. *Journal of Applied Physics*, 75(11):7570–7572, 1994.

[94] Jeremie Werner, Gizem Nogay, Florent Sahli, Terry Chien-Jen Yang, Matthias Brauninger, Gabriel Christmann, Arnaud Walter, Brett A Kamino, Peter Fiala, Philipp Looper, et al. Complex refractive indices of cesium–formamidinium-based mixed-halide perovskites with optical band gaps from 1.5 to 1.8 ev. *ACS Energy Letters*, 3(3):742–747, 2018.

[95] Atteq ur Rehman, Emmanuel P Van Kerschaver, Erkan Aydin, Waseem Raja, Thomas G Allen, and Stefaan De Wolf. Electrode metallization for scaled perovskite/silicon tandem solar cells: Challenges and opportunities. *Progress in Photovoltaics: Research and Applications*, 2021.

[96] Léo Basset. *Contact electrodes for heterojunction silicon solar cells: Evaluations and optimizations of the electron contact*. Phd thesis, Université de Lille, November 2020.

[97] Marius H. Zehender, Iván García, Simon A. Svatek, Myles A. Steiner, Pablo García-Linares, Emily Warren, Adele Tamboli, Antonio Martí, and Elisa Antolín. Demonstrating the gainp/gaas three-terminal heterojunction bipolar transistor solar cell. In *2019 IEEE 46th Photovoltaic Specialists Conference (PVSC)*, pages 0035–0040, 2019.

[98] Marius H Zehender, Iván García, Simon A Svatek, Myles A Steiner, Pablo García-Linares, Emily Warren, Adele Tamboli, Antonio Martí, and Elisa Antolín. Demonstrating the gainp/gaas three-terminal heterojunction bipolar transistor solar cell. In *2019 IEEE 46th Photovoltaic Specialists Conference (PVSC)*, pages 0035–0040. IEEE, 2019.

[99] Linear Technology, ltspice xvii.

[100] Timo Wenzel, Andreas Lorenz, Elmar Lohmuller, Simon Auerbach, Kenji Masuri, Yin Cheung Lau, Sebastian Tepner, and Florian Clement. Progress with screen printed metallization of silicon solar cells-towards 20 mum line width and 20 mg silver laydown for perc front side contacts. *Solar Energy Materials and Solar Cells*, 244:111804, 2022.

[101] Kiichi Kamimura Kiichi Kamimura, ZhanHe Wang ZhanHe Wang, and Yoshiharu Onuma Yoshiharu Onuma. Contact resistance of sno2 films determined by the transmission line model method. *Japanese journal of applied physics*, 37(6R):3284, 1998.

[102] Jerzy Kanicki. Contact resistance to undoped and phosphorus-doped hydrogenated amorphous silicon films. *Applied physics letters*, 53(20):1943–1945, 1988.

[103] M Shahidul Haque, HA Naseem, WD Brown, and SS Ang. Hydrogenated amorphous silicon/aluminum interaction at low temperatures. *MRS Online Proceedings Library (OPL)*, 258:1037, 1992.

[104] Priyanka Roy, Aritra Ghosh, Fraser Barclay, Ayush Khare, and Erdem Cuce. Perovskite solar cells: A review of the recent advances. *Coatings*, 12(8):1089, 2022.

[105] Stefano Pisoni, Romain Carron, Thierry Moser, Thomas Feurer, Fan Fu, Shiro Nishiwaki, Ayodhya N Tiwari, and Stephan Buecheler. Tailored lead iodide growth for efficient flexible perovskite solar cells and thin-film tandem devices. *NPG Asia Materials*, 10(11):1076–1085, 2018.

[106] Sung Hun Lee, Seungyeon Hong, Seongho An, Tae-Yoel Jeon, and Hyo Jung Kim. Strategy for the complete conversion of thermally grown pbi 2 layers in inverted perovskite solar cells. *Electronic Materials Letters*, 16:588–594, 2020.

[107] Yani Chen, Bobo Li, Wei Huang, Deqing Gao, and Ziqi Liang. Efficient and reproducible ch 3 nh 3 pbi 3- x (scn) x perovskite based planar solar cells. *Chemical communications*, 51(60):11997–11999, 2015.

[108] Mohamad Firdaus Mohamad Noh, Nurul Affiqah Arzaee, Inzamam Nawas Nawas Mumthas, Amin Aadenan, Hussain Alessa, Mohammed N Alghamdi, Hazim Moria, Nurul Aida Mohamed, Mohd Asri Mat Teridi, et al. Facile tuning of pbi2 porosity via additive engineering for humid air processable perovskite solar cells. *Electrochimica Acta*, 402:139530, 2022.

[109] Rui Li, Huanyu Zhang, Mei Zhang, and Min Guo. Effect of pbi2 solution on air-preparation of perovskite solar cells for enhanced performance. *Applied Surface Science*, 458:172–182, 2018.

[110] Emanuele Centurioni. Generalized matrix method for calculation of internal light energy flux in mixed coherent and incoherent multilayers. *Applied Optics*, 44(35):7532–7539, 2005.

[111] David Stroud. The effective medium approximations: Some recent developments. *Superlattices and microstructures*, 23(3-4):567–573, 1998.

[112] Rajeev Ahuja, Hans Arwin, A Ferreira da Silva, Clas Persson, JM Osorio-Guillén, J Souza de Almeida, C Moyses Araujo, E Veje, N Veissid, CY An, et al. Electronic and optical properties of lead iodide. *Journal of applied physics*, 92(12):7219–7224, 2002.

[113] N Convers Wyeth. Sheet resistance component of series resistance in a solar cell as a function of grid geometry. *Solid-State Electronics*, 20(7):629–634, 1977.

[114] Alexander W. Haas, John Robert Wilcox, Jeffery Lynn Gray, and Richard J. Schwartz. A distributed emitter model for solar cells: Extracting an equivalent lumped series resistance. *2010 35th IEEE Photovoltaic Specialists Conference*, pages 002044–002049, 2010.